University of Copenhagen

Niels Bohr Institute, Faculty of Science

Thesis submitted for the degree of MSc in Physics

STM predictions for the loop-current pseudogap theory of the cuprates

William H. P. Nielsen

January 2012

Academic supervisor:
Brian M. Andersen

Resumé

I dette speciale undersøges de eksperimentelle konsekvenser af den af C. M. Varma fremsatte teori om intra-orbitale strømme som forklaringsmodel for pseudogabfasen i kupraterne. Nærmere bestemt undersøges en middelfeltsteoretisk tre-båndsmodel med intra-orbitale strømme. Denne model vises at være selvkonsistent for visse parameterværdier samt at give eksakt strømbevarelse igennem hver orbital. Modellen udvides herefter til også at inkludere en sameksisterende ordensparameter for superledning. Denne udregnes ikke selvkonsistent.

Modellens forudsigelser for modulationerne i den lokale tilstandstæthed omkring en enkelt urenhed er specialets egentlige resultat. Spredningen på urenheden beregnes ved hjælp af en eksakt greensfunktionsformalisme. Det findes at tilstædeværelsen af en ikke-forsvindende værdi for orbitalstrømmenes middelfeltsparameter giver anledning til en brudt C4-symmetri i nærheden af urenheden. Dette resultat er kvalitativt uændret af tilstedeværelsen af superledning i modellen, men superledning findes at forstærke effekten. Resultatet forklares kvalitativt i termer af strømmenes middelfeltsparameters indvirkning på de energikonturer elastisk spredning foregår imellem. Det konkluderes således som eksperimentel forudsigelse, at en STM-måling i nærheden af en enkelt urenhed principielt set bør kunne bekræfte dette C4-brud.

Preface

Physics is an experimental science. Regardless of the beauty or horridness of a theory, it can only measure its worth against the test of experiment. As a theoretical physicist, it is ones most honoured duty to deduce concrete experimental predictions from abstract theoretical ideas. In its own humble way, this thesis is an attempt to heed to this duty.

The field of high-temperature superconductivity is ripe with experimental data and theoretical explanations, but is yet to converge in favour of one unifying idea explaining everything. It is not altogether unlikely that the "real" explanation has not even been put forward yet. But in order to ever confirm any idea in that direction, we must of course carefully analyse the present theories and systematically judge them in the laboratory. The work presented here is a small step in that direction. We single out one particular theory and one particular experiment, and then attempt to answer the question "if the theory is correct, what will the experiment see?" Regardless of the outcome of the experiment, it should leave us wiser than we were before, and thus in principle one (small) step closer to understanding the physics of high-temperature superconductivity.

Although this might only be a small step for science, it is of course a giant leap for the author, who would therefore like to give credit where credit is due.

The author is grateful towards his advisor, Brian Andersen, for proposing the project and for guidance throughout the entire process, and towards Rasmus Christensen, Shantanu Mukherjee, Astrid Rømer and especially Bill Atkinson for valuable discussions and input ideas. Also friends and family deserve thanks for their support and patience during this past year. Above all, I am of course indebted dla kwiatuszka mojego, Agnieszka Frąszczak.

William H. P. Nielsen
Copenhagen, December 2011

Contents

Chapter 1

Introduction

It was never an easy task to understand superconductivity. From the famous initial discovery of a *near-enough zero* resistivity in 1911 (see [1]) it took 46 years, many failed attempts and even required the birth of an entirely new physical theory - quantum mechanics - before the world received a satisfying microscopic theory of superconductivity (The famous BCS paper: [2]). Satisfying should in this context be understood as of course providing an actual physical mechanism - that electrons pair two and two, become bosons this way and condensate - but also that the theory describing this is simple. To quote the authors of [2], "Advantages of the theory are [...] The theory is simple enough so that it should be possible to make calculations of thermal, transport, and electromagnetic properties of the superconducting state".

In 1986, a new sort of superconductivity was discovered (ref. [3]), and once again the phenomenon proved itself difficult to understand. Even today, more than a hundred thousand of papers[1] later, there is still no consensus regarding the proper microscopic theory for high-temperature superconductivity. The quest for this theory has been called the quest for the holy grail of contemporary condensed matter theory (ref. [5]). Stakes are high, and it is possible that a new scientific break-through is needed in order to fully understand the intricacies of high temperature superconductivity. But of course, one can not lean back and wait for such a break-through to fall from the sky. Instead, we must carefully try to understand the already proposed explanations and ideas, and make them meet the ultimate test of experiment. In order to do so, we attempt to keep our focus straight and things as simple as possible.

1.1 A minimal introduction to the materials

Before we straighten our focus entirely, we take a brief look back in time, and around the present day scene of the high-T_C field. It is by no means our goal to give an exhaustive account of the many interesting ideas and results that high temperature superconductivity has spawned throughout the years, but it would on the other hand be unfair not to mention any of them, especially since our knowledge of the cuprates is by no means small, albeit incomplete. We skip through this rich story very rapidly, but see e.g. [6] for a more thorough review.

The entire field of high-temperature superconductivity began with the discovery of (possible) superconductivity in $Ba_xLa_{5-x}Cu_5O_{5(3-y)}$ (ref. [3]). Within less than a year, a number of other superconducting compounds had been discovered, all of which shared the same basic crystalline structure: copper and oxygen in planes with different fillings in between. This structure is illustrated in Figure 1.1. These compounds received the name cuprates and quickly became a major field of research in their own right.

[1] The number was already beyond 120 000 in 2004 according to the preface of [4].

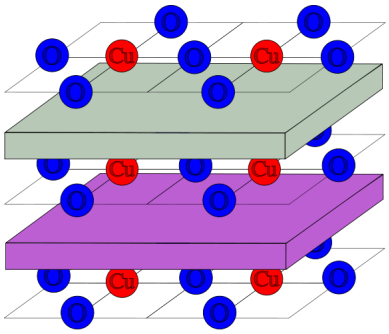

Figure 1.1: The basic structure of a cuprate; copper-oxygen layers and "stuff". The "stuff" dopes the CuO_2 layers by adding electrons or holes to them, thereby altering the electronic properties of the compound. Typical cuprates in modern experiments are Bi-Sr-Ca-Cu-O and Y-Ba-Cu-O.

As further experiments were performed, it turned out that the cuprates had more in common than just being superconducting at high temperatures. A whole temperature-doping phase diagram is shared between the cuprates, with very different models yielding good results deep within each phase. For instance, close to zero doping the system is a very strong insulator (a Mott insulator), whereas it upon increased doping becomes the opposite, namely superconducting. The problem of understanding the mechanism of high-temperature superconductivity thus evolved into the problem of understanding the cuprate phase diagram.

We depict the phase diagram in Figure 1.2a, leaving out some of its regions that are not of importance to our story[2]. It is worth noting that although the overall picture is somewhat unclear, certain facts are well established. Of main importance to us is the consensus that the superconducting phase is well described by a $d_{x^2-y^2}$-wave gap function (also indicated in Figure 1.2a). We shall employ this fact in the next chapter when we build our model.

1.1.1 The great mystery: the pseudogap

Whereas the superconducting phase and the Mott insulating phase are, as the names suggest, proper phases with well-defined phase transition temperatures, the pseudogap region of the phase diagram is more reluctant to be classified. The name pseudogap stems from the fact that a certain energy range near the Fermi energy contains very few (but some; hence the *pseudo* in pseudogap) occupied states; there is a gap in the density of states (see Figure 1.2b). As a proper gap is a characteristic of BSC-type superconductivity, the pseudogap is an interesting feature of the cuprates. If it is the pseudogap that evolves into the superconducting gap, an understanding of the pseudogap must reveal important information of the microscopic origin of high-temperature superconductivity. Even if this is not the case, the position of the pseudogap in the middle of the phase diagram makes it an very relevant place to attack, in order to gain insight into the strange physics of the cuprates.

1.2 The circulating current theory

Many theories and conjectures have been put forward to explain the pseudogap region of the phase diagram. They can roughly be classified as constituting two schools (this view is adopted from ref. [9], where the reader may find references to support this line of thought), where the former believes the pseudogap to be caused by pre-formed Cooper pairs and thus

[2]These are the regions to the right of the superconducting dome. See e.g. [7].

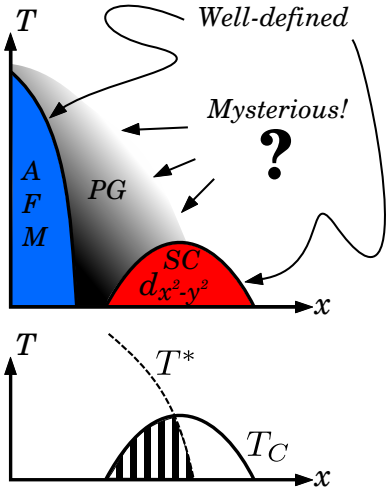

(a) Top: Our slightly suggestive qualitative drawing of the cuprate phase diagram. x denotes (hole) doping. Bottom: The loop current perception. T_c denotes the well-defined superconducting transition temperature. T^* is the pseudogap temperature.

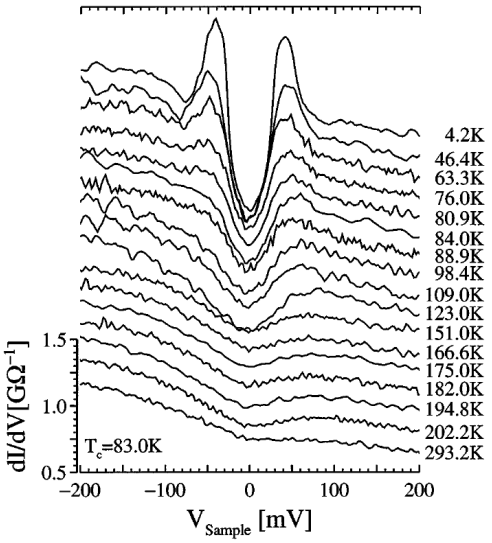

(b) A (pseudo) gap in the density of states persisting high above the superconducting transition temperature in $Bi_2Sr_2CaCu_2O_{8+\delta}$. T^* is not readily extracted from this figure. Adapted from reference [8].

Figure 1.2: The experimental evidence of a pseudogap is clear, but there is still no consensus on the theoretical explanation.

do not consider the pseudogap *phase* to exist, the latter believes the explanation to hinge on another, i.e., not-superconducting order parameter, thus requiring a phase transition connected with the pseudogap. This other order may then compete against the superconductivity (and loose its ground in the superconducting dome) or partly co-exist with the superconductivity. The theory we shall be concerned with belongs to the second school, and has been put forward by C. M. Varma. In a series of papers (mainly [10], [11] and especially [12]), Varma has related the pseudogap behaviour of the cuprates to a broken time-reversal symmetry state, which is believed to co-exist with superconductivity in the left part of the superconducting dome, depicted as the striped region of the lower part of Figure 1.2a. He furthermore suggests that the time-reversal violation is realized through small circulating current patterns within each Cu-O-O unit cell. In reference [12], the theory in mean-field boils down to two possible current patterns, shown in Figure 1.3.

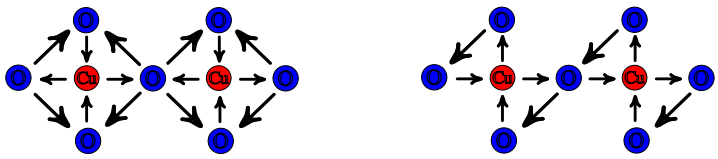

Figure 1.3: The two possible current patterns. Both are translation invariant and time-reversal breaking, but they break different other spatial symmetries (this will be discussed at great length in chapters 3 and 5.)

From what we have said so far, it is of course by no means clear why circulating currents

should explain the phase diagram of the cuprates[3]. Nor is it the scope of this thesis to discuss or derive results in that direction. We shall simply assume the theory and attempt to produce an experimental prediction from this assumption. Let us, however, try to motivate our assumption by touching upon a few experimental results in favour of the theory. Subsequently we shall - to be fair - also mention a few results against the circulating current idea.

1.2.1 Experimental indications in favour of the currents

We now mention four important experiments motivating our interest in Varma's theory. It is far beyond the scope of this introductory chapter to provide detailed accounts of the experiments, but a short review of their scopes and conclusions is appropriate. The purpose is not so much to argue pro or contra the validity and cause of the different results, as to give the reader an overview of the status in the community; a justification for considering this particular theory.

An experiment that really got the ball rolling for the circulating current theory was the polarized elastic neutron scattering experiment by Fauqué et al. of 2006 (ref. [9]). The main idea of the experiment was to shine a spin-polarized neutron beam at a cuprate sample, and then count the rate of spin-flipped outgoing neutrons whereby a magnetic signal would be revealed. Due to the translation invariance of the current patterns, this extra magnetic signal is superimposed on the nuclear Bragg peaks, making the experiment a rather delicate one. In fact, the signal searched for is of order 10^{-4} of the background. But the group succeeded, and the experiment, which was performed on $YBa_2Cu_3O_{6+x}$, showed a magnetic signal in agreement with the doping and temperature ranges of the pseudogap phase and also in agreement with the translational invariance of the proposed current patterns. It is hence verified that the pseudogap phase exhibits intra-unit cell magnetic order.

For another cuprate, namely $Bi_2Sr_2CaCu_2O_{8+\delta}$, a similar experiment performed in 2002 by Kaminski et al. (ref. [13]) also showed a breaking of time-reversal symmetry tied closely together with the pesudogap phase (see Figure 1.4). This time it was left-, and right-circularly polarized photons that in an ARPES setup gave rise to a dichroism which revealed the symmetry breaking. The authors furthermore observe that this time-reversal breaking persists into the superconducting regime, indicating a co-existence of whatever causes the time-reversal symmetry to be broken and the superconducting Cooper pairs. We urge to note that this experiment is somewhat controversial (see the next subsection).

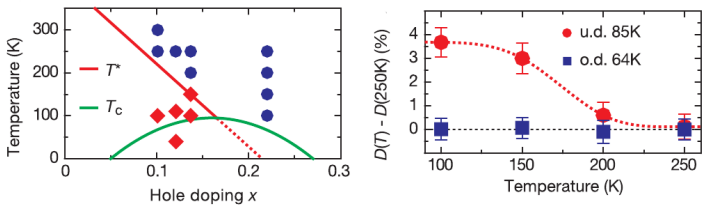

Figure 1.4: Results adapted from [13]. Right: the difference in dichroism between (almost) room temperature and respectively an under-doped sample at 85K and an over-doped sample at 64K. Left: the extrapolated phase diagram from all the data. Absence of dichroism at the blue points and presence at the red points.

That circulating currents are a good candidate as time-reversal breakers are indicated by a recent experiment by Scagnoli et al. (ref. [14]). In this experiment, resonant x-ray diffraction was used to observe circulating orbital currents completely similar to those proposed by Varma (see Figure 1.5). The experiment was *not* performed on a cuprate, but on a CuO plaquette.

[3]As a matter of fact, the mean-field theory does not even produce the pseudogap. This is discussed at the end of chapter 3.

It is thus not a final verification of the orbital current theory for the cuprate pseudogap, but nonetheless a strong hint of the relevance of orbital currents for copper oxide physics.

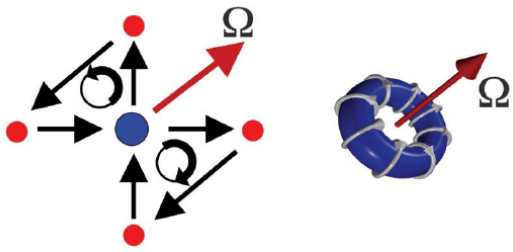

Figure 1.5: The authors of ref. [14] own visualization of their result. The blue ring to the right illustrates that the resulting toroidal magnetic moment Ω points out of the plane. Note that copper is blue and oxygen is red in this picture.

Besides breaking time-reversal symmetry and maintaining translation invariance, we also immediately see from Figure 1.3 that the orbital current patterns of Varma's theory are not invariant under a π rotation (what we shall also call a C4 operation). This C4-invariance breaking has actually been detected in $Bi_2Sr_2CaCu_2O_{8+\delta}$ by STM measurements in 2010 by Lawler et al. (ref [15]), where it was ascribed to a nematic ordering. This result is of interest to us, as it agrees qualitatively with what we find (in chapter 4) upon calculating the local density of states for a mean-field theory with orbital currents. A main difference, however, is that the authors of [15] find an ordered C4-breaking, whereas the C4 symmetry in our results is completely respected in the absence of impurities. In any case, it is an indication that intra-unit cell effects play an important role in the description of the cuprates.

1.2.2 Results against the currents

It was never an easy task to understand the pseudogap. Obviously, the true picture is a bit more complicated than what we have presented so far. The literature does not only provide us with strong indications of the validity of Varma's loop current idea, relevant objections are also present. In this thesis we shall only assume the theory rather than derive it, and we therefore make no claims that it is actually true; we simply derive a consequence of it being true. Our work might then end up providing a prediction in contrast with experimental data and thus be a step in the falsifying direction. As the following two examples show, an ultimate falsification of the loop-current theory would not be a complete shock to the (entire) community.

A search for weak magnetic fields emanating from orbital currents using nuclear-quadropole-resonance came out negatively. The experiment, performed in 2011 by Strässler et al. and documented in ref. [16], examined the cuprate $YBa_2Cu_4O_8$ at 90 K, which is within the pseudogap phase of that material. More specifically, the investigation probed the local field at the Ba site, where the magnetic fields from the orbital currents should enhance each other and the presence of these orbital currents thus readily be detected. The resulting data showed practically no deviation from the reference measurements at 300 K, and it is thus concluded that no magnetic order is associated with the pseudogap region.

In a second ARPES experiment of 2004 (ref. [17]) the experiment of Kaminski et al (ref. [13]) described in the previous subsection was repeated for $(Pb,Bi)_2Sr_2CaCu_2O_{8+\delta}$. In this case the observed dichroism was insensitive to the change in doping and temperature reported earlier. The authors conclude that the time-reversal breaking in the pseudogap state is not generic for the cuprates.

The indications in favour of the theory are strong, but so is the justly sceptical opposition.

The present day situation is somewhat contradictory, which is of course a strong motivation for conducting further experiments and theoretical studies.

1.3 This thesis

The ultimate goal of our work is to present a compelling evidence that the loop-current theory of the pseudogap phase implies some very distinct predictions for a certain experiment; to find a smoking gun, so to speak. If there really *are* circulating currents within each unit cell, then a mean-field theory capturing this feature should be able to produce some non-trivial behaviour for certain physical properties of the cuprates.

1.3.1 The experiment we seek to predict

As already mentioned, we want to perform a theoretical calculation predicting the outcome of an STM experiment. Let us briefly explain how this experiment is performed in real life and what the implications hereof might be for us upon attempting to model the experiment.

The underlying principle of a scanning tunnelling microscope is quite simple; one moves an atom-thin needle about in the very near proximity of a sample, puts a bias voltage across the system and measures how electrons (or holes) tunnel from the needle to the sample (or vice versa). This tunnelling current, I, as a function of the bias voltage, V, can then be used to find the differential tunnelling conductance, $\mathrm{d}I/\mathrm{d}V$, which is proportional to the local density of states at the needle tip position (see e.g. ref. [18]). Once we calculate this quantity, we thus have an experimentally testable prediction. The differential tunnelling conductance is experimentally found at a certain bias voltage, which can of course be varied. This will in our calculations correspond to the density of states at a certain energy.

State of the art apparatus offers Angström-scale resolution (see e.g. [19], [20] or [21]), and is thus in principle easily able to see the individual atoms of the sample. In reality, the effects of the tunnelling through other layers of the sample might mix the signal from each atom (this is discussed in [4, chapter 3]), but it is surely not naïve to make predictions about the local density of states on the nearest and next-nearest atomic neighbours of an atomic sized impurity; the experiment *can* measure effects on this length scale. The precision that we are going to work with will be one that has (generally) different DOS values for different atoms, but only one value per atom, or, as we shall mostly denote them, orbital. This should be within the limits accessible to present day experiments.

1.3.2 The model that we employ

Since the STM experiments take place at very low temperatures, the region of the phase diagram they probe is inside the superconducting dome (as seen in Figure 1.2a). As it has been mentioned in the previous section, the fingerprints of the currents are not believed to be absent from the left part of the superconducting dome (see [12]). We therefore seek to combine the bare mean-field theory of the loop currents with a theory containing d-wave superconductivity. At the same time, we seek the simplest possible model capturing these features.

As the minimal number of points needed to form a closed loop is three, we need to include three orbitals per unit cell in order to have closed circulating intra-orbital current loops. We thus choose a unit cell consisting of two oxygen orbitals and one copper orbital (see Figures 3.1 and 4.1). Our model will only deal with the two-dimensional copper-oxygen plane, since, as it should be clear by now, the copper-oxygen planes are believed to contain the main physics of the cuprates. The starting point for our model is then the three-band Emery model (see ref. [22]) treated in mean-field. Unto this model we then superimpose superconductivity, providing us with the minimal model capturing the essence of the experimental situation we seek predict.

As we are not interested in phase transitions, but rather the ground-state properties of our systems, we set the temperature to zero throughout this work.

1.3.3 The structure of the thesis

The structure of this thesis will then be as follows. In the next chapter, we introduce the formalism and notation we shall make use of in order to describe the copper oxides, with and without superconductivity present. In chapter 3 we show how to get the circulating currents into our model, and show that a self-consistent mean-field parameter for the currents can be found. We furthermore deduce the explicit current patterns consistent with current conservation, and find that no clear predictions can be made from this homogeneous mean-field model alone. In chapter 4 we therefore introduce a single impurity, and consider the local density of states modulations arising from this. Non-trivial current dependencies are found in modulations. Chapter 5 discusses these modulations, and relate their symmetries to the symmetries of the current patterns, and also provides an explanation for how this can be understood in terms of changes in the dispersion. Chapter 6 is a brief conclusion.

Chapter 2

Background

In this chapter we introduce the formal building blocks of our theory and establish the notation. Many quantities mentioned in the previous introductory chapter are now properly defined and explained. Parts of this chapter consists of textbook material that is covered in depth in e.g. ref. [23]. Here, we shall only go into detail with the tools specifically required for our purposes. The main purpose is thus to set the technical stage for later chapters regarding the model employed, as well as to give a full account of our calculational schemes and their (dis)advantages.

2.1 Quantum mechanics of solids (very briefly)

The theoretical framework we work within is the language of second quantization. In this respect and thus for the rest of this section, we largely follow the terminology and notation of ref. [23].

2.1.1 Hamiltonian

At the heart of second-quantized quantum theory resides the Hamiltonian. In this work we only treat fermions, and our Hamiltonian $\mathcal{H}$ is always of the form

$$\mathcal{H} = \sum_{\nu,\nu',\mu,\mu'} A_{\nu\nu'\mu\mu'} c_\nu c_{\nu'} c_\mu^\dagger c_{\mu'}^\dagger + B_{\mu\nu} c_\mu^\dagger c_\nu + C_{\nu\nu'} c_\nu c_{\nu'} + D_{\mu\mu'} c_\mu^\dagger c_{\mu'}^\dagger, \tag{2.1}$$

where ν, ν', μ, μ' are arbitrary quantum numbers, the A, B, C, D are complex numbers and the c-operators are fermionic operators obeying

$$\{c_\nu, c_{\nu'}^\dagger\} = \delta_{\nu,\nu'}. \tag{2.2}$$

Furthermore, we shall always decouple the Hamiltonian, so that it only contains terms with two operators, i.e.,

$$\mathcal{H} = \sum_{\mu,\nu} h_{\mu\nu} c_\mu^\dagger c_\nu + \Delta_{\mu\nu} c_\mu^\dagger c_\nu^\dagger + \Delta_{\nu\mu}^* c_\nu c_\mu, c_{\nu'} c_{\mu'}^\dagger \left\langle c_\nu c_\mu^\dagger \right\rangle + c_\nu c_\mu^\dagger \left\langle c_{\nu'} c_{\mu'}^\dagger \right\rangle c_\nu c_{\mu'}^\dagger \left\langle c_{\nu'} c_\mu^\dagger \right\rangle + c_{\nu'} c_\mu^\dagger \left\langle c_\nu c_{\mu'}^\dagger \right\rangle \tag{2.3}$$

where h and Δ now have to be hermitian matrices in ν and μ. This sort of decoupling is known as a mean-field decoupling (we shall discuss it further in the next chapter), and is based on the assumption that there exists certain operator expectation values, around which only small

fluctuations occur, and that one therefore can approximate an operator pair by its expectation value (hence the name *mean*-field theory). In formulas, one sets

$$\sum_{\nu,\nu',\mu,\mu'} A_{\nu\nu'\mu\mu'} c_\nu c_{\nu'} c^\dagger_\mu c^\dagger_{\mu'} \approx \sum_{\nu,\nu',\mu,\mu'} A_{\nu\nu'\mu\mu'} (c_\nu c^\dagger_{\mu'} \left\langle c_{\nu'} c^\dagger_\mu \right\rangle + c_{\nu'} c^\dagger_\mu \left\langle c_\nu c^\dagger_{\mu'} \right\rangle) \tag{2.4}$$

$$- \sum_{\nu,\nu',\mu,\mu'} A_{\nu\nu'\mu\mu'} \left\langle c_{\nu'} c^\dagger_\mu \right\rangle \left\langle c_\nu c^\dagger_{\mu'} \right\rangle . \tag{2.5}$$

As the alert reader will notice, there are two other ways (or: exchange channels in which [24, Chapter 6]) we might as well have decoupled the four-operator term, so that in total there are three choices;

$$c_\nu c_{\nu'} c^\dagger_\mu c^\dagger_{\mu'} \to \left\{ c_\nu c_{\nu'} \left\langle c^\dagger_\mu c^\dagger_{\mu'} \right\rangle + c^\dagger_\mu c^\dagger_{\mu'} \left\langle c_\nu c_{\nu'} \right\rangle \quad , \right. \tag{2.6}$$

each leading to a different decoupling and thus a different resulting Hamiltonian. This choice, as well as the basic mean-field assumption, must of course be motivated by some physical understanding of the system in question.

One of the benefits of mean-field theory is the possibility of re-writing the Hamiltonian as an inner product, and thus recover a Hamiltonian *matrix*. If we let $\mu_1, \mu_2, \ldots$ denote all the values μ can take and define a vector of operators ψ through its hermitian adjoint as

$$\psi^\dagger = (c^\dagger_{\mu_1}, c^\dagger_{\mu_2}, \ldots, c_{\nu_1}, c_{\nu_2}, \ldots), \tag{2.7}$$

we can write the Hamiltonian as

$$\mathcal{H} = \psi^\dagger H \psi, \tag{2.8}$$

where $\mathcal{H}_{\text{matrix}}$ is a hermitian matrix. For the rest of the thesis, we shall use H to denote the matrix and $\mathcal{H}$ to denote the operator, possibly with some subscript specifying the system in question.

Of course, many choices of ψ are possible, and finding the right operator basis can be of substantial practical importance in solving a problem.

2.1.2 The Hilbert space

The Hamiltonian needs a space to act on. As is common practice in condensed matter theory, we take this to be the Fock space of all many-particle states (see also [24, Chapter 2]). We exploit some features of the Fock space in later chapters, in particular the orthogonality of states with different particle numbers in chapter 3. For now, we mention it for completeness, and to say a few things about how we keep track of quantum numbers.

Let us write the full Fock space $\mathcal{F}$ as

$$\mathcal{F} = \bigoplus_{n=1} \mathcal{F}_n, \tag{2.9}$$

where $\mathcal{F}_N = \text{span}\{|n_{\nu_1}, n_{\nu_2}, \ldots\rangle \mid \sum_j n_{\nu_j} = N\}$, and the state $|n_{\nu_1}, n_{\nu_2}, \ldots\rangle$ has n_{ν_1} particles in the single-particle state $|\nu_1\rangle$, n_{ν_2} particles in the single-particle state $|\nu_2\rangle$ and so forth. It is then relevant for us to ask how we should label a single-particle state $|\nu\rangle$.

In most solid state systems, and certainly in the systems we shall consider, there are three important quantum numbers, namely spin, σ, position, $\mathbf{r}$, and momentum, $\mathbf{k}$. Essentially, this is all there is to the story. An electron or hole has a spin and is somewhere in the lattice, which, by virtue of being a lattice, puts some constraints on the eletron/hole momentum. When dealing with multi-orbital systems, however, we also introduce an *orbital* quantum number ℓ, where, in our case, $\ell \in \{d, p_x, p_y\}$. The letters refer to the types of orbitals; on copper a d-orbital resides and on each oxygen a p-orbital is found. See also Figure 3.1.

Now, in equations (2.2) and (2.3) we said nothing about whether ν and μ refer to spin, position or what not. Generally, it will be understood that the operators are fermionic in all their quantum numbers, i.e.,

$$\{c_\nu, c^\dagger_{\nu'}\} \equiv \{c_{\sigma \mathbf{r} \ell}, c^\dagger_{\sigma' \mathbf{r}' \ell'}\} = \delta_{\sigma,\sigma'} \delta_{\mathbf{r},\mathbf{r}'} \delta_{\ell,\ell'}, \tag{2.10}$$

and that we, upon writing ν and μ, refer to *sets* of anticommuting quantum numbers.

Not all fermionic quantum numbers are anticommuting. What we mean by this is Heisenberg's uncertainty relation; not all quantum numbers can be specified simultaneously. Referring back to the single-particle state $|\nu\rangle$ above, we see that if $\nu = (\mathbf{r}, \sigma, \ell)$ then $|\nu\rangle = |\mathbf{r}\rangle \otimes |\sigma\rangle \otimes |\ell\rangle$. These are all anticommuting quantum numbers. The only ones we shall encounter that are not are $\mathbf{r}$ and $\mathbf{k}$.

2.1.3 Fourier Transform

Assume - as will often be the case - that our Hamiltonian is translation invariant. In that case a Fourier transformation into $\mathbf{k}$-space is a sound thing to perform, as two spatial indices are then replaced by a single momentum one. In many cases - for instance when dealing with a tight-binding Hamiltonian - the Hamiltonian can most conveniently be written in real space, and is then given as

$$\mathcal{H} = \sum_{\mathbf{r},\mathbf{r}',\nu,\nu'} h_{\mathbf{r}\mathbf{r}'\nu\nu'} c^\dagger_{\mathbf{r},\nu} c_{\mathbf{r}',\nu'}, \tag{2.11}$$

with ν and ν' labelling some other quantum numbers than position, and $\mathbf{r}$ and $\mathbf{r}'$ being understood to label lattice sites. The Fourier transform is then straightforwardly

$$c_{\mathbf{r},\nu} = \frac{1}{\sqrt{N}} \sum_{\mathbf{k}} \mathrm{e}^{i\mathbf{k}\cdot\mathbf{r}} c_{\mathbf{k},\nu}, \quad \text{and} \quad c^\dagger_{\mathbf{r},\nu} = \frac{1}{\sqrt{N}} \sum_{\mathbf{k}} \mathrm{e}^{-i\mathbf{k}\cdot\mathbf{r}} c^\dagger_{\mathbf{k},\nu}, \tag{2.12}$$

with N being the system size.

Now, what if the quantum number labelled by ν actually contained some spatial information? This would be the case if, say, every second lattice site could only be occupied by a spin up electron. For the three band model properly introduced in the next chapter, this is indeed the case, as the orbitals are spacially seperated, but still considered to reside at *one lattice site*[1]. The answer is that the Fourier transform should reflect this fact, such that in general

$$c_{\mathbf{r},\nu} = \frac{1}{\sqrt{N}} \sum_{\mathbf{k}} \mathrm{e}^{i\mathbf{k}\cdot(\mathbf{r}+\mathbf{v}(\nu))} c_{\mathbf{k},\nu}, \quad \text{and} \quad c^\dagger_{\mathbf{r},\nu} = \frac{1}{\sqrt{N}} \sum_{\mathbf{k}} \mathrm{e}^{-i\mathbf{k}\cdot(\mathbf{r}+\mathbf{v}(\nu))} c^\dagger_{\mathbf{k},\nu}, \tag{2.13}$$

where the specific system determines $\mathbf{v}(\nu)$. For the three-orbital model $\mathbf{v}(\ell)$ can be plus/minus one half lattice point distance.

2.1.4 Green's functions

An object that will be immensely important to us is the Green's function. It is no exaggeration to say that this thesis is really about calculating the Green's function for different Hamiltonians. What is a Green's function? Physically, we can think of it as a correlation function between two states at two different times, roughly telling us something about the probability for the system to go from the from the former state to the latter.

Now, for our purposes, we are never going to deal with anything time-dependent. Everything is in equilibrium, and the system is thus time-translation invariant. Just as spatial translational invariance makes it obvious to work in $\mathbf{k}$-space, time-translational invariance

[1] That is to say, three orbitals pr. lattice site.

makes the frequency domain a nice place to work. Furthermore, the STM measurements we want to predict are static measurements scanning the energy. We therefore only really care for Green's functions as functions of (real) frequency.

We define the Green's function for our system as[2]

$$G(\omega) := (1(\omega + i\eta) - H)^{-1}, \tag{2.14}$$

where η is a small regulator. We say *the* Green's function, although this is really the *retarded* Green's function we defined in equation 2.14. When nothing else is specified, we mean to refer to the retarded function.

For a general N site system, H is a rather large matrix, and somewhat unwieldy to invert. But, of course, if the Hamiltonian is (block) diagonal in one index, for instance in $\mathbf{k}$, such that

$$\mathcal{H} = \sum_{\mathbf{k}} \psi^\dagger(\mathbf{k}) H(\mathbf{k}) \psi(\mathbf{k}), \tag{2.15}$$

with $H(\mathbf{k})$ and $\psi(\mathbf{k})$ still possibily carrying more indices, then

$$H = \bigoplus_{\mathbf{k}} H(\mathbf{k}), \tag{2.16}$$

and hence

$$G(\omega) = (1(\omega + i\eta) - \bigoplus_{\mathbf{k}} H(\mathbf{k}))^{-1}. \tag{2.17}$$

We therefore define the Green's function of momentum (and in doing so, by Fourier transformation also of position) as

$$G(\mathbf{k}, \omega) = (1(\omega + i\eta) - H(\mathbf{k}))^{-1}. \tag{2.18}$$

Obviously,

$$G(\omega) = \bigoplus_{\mathbf{k}} G(\mathbf{k}, \omega), \tag{2.19}$$

and the matrix-inversion process is now very manageable, but has to be repeated for each block diagonal index, in this case $\mathbf{k}$.

In general, we define the Green's function for any two (sets of) quantum numbers μ and ν as

$$G_{\mu\nu}(\omega) = \left[(1(\omega + i\eta) - H)^{-1}\right]_{\mu\nu}. \tag{2.20}$$

2.1.5 Spectral function and density of states

The main reason that we care so much for Green's functions is the information they contain about the spectral density of the system. Given a (retarded) Green's function, we define the spectral function A as

$$A(\nu, \omega) = -2\mathrm{Im}[G_{\nu\nu}(\omega)]. \tag{2.21}$$

The spectral function is a measure of how much spectral weight the system has in the given quantum numbers, or, in more plain English, how many states with the specific quantum numbers there are at a given energy. This is also the reason why we only define it diagonally. The spectral function relates directly to the density of states, ρ, via the following formula:

$$\rho(\omega) = \frac{1}{\mathcal{N}\pi} \mathrm{Tr}[A(\nu, \omega)], \tag{2.22}$$

[2]The "1" is always understood to be the identity operator on the relevant space.

where the trace is understood to be over *all* quantum numbers and $\mathcal{N}$ is a corresponding normalization factor. In case we do not perform the full trace, the resulting quantity will be the "untraced quantum number"-resolved density of states. In practice, we shall encounter only not tracing over position, thus yielding the spacially resolved or local density of states, LDOS, and not tracing over the orbital quantum numbers. The fully **k**-traced DOS is sometimes referred to as the bulk density of states.

2.2 Example 1: The three band model

Just to get a feel for what is actually going on, we now describe how we find the density of states on each orbital for the three orbital model. A derivation of the specific form of the Hamiltonian will be given in the next chapter. For a homogeneous system, **k**-space is the place, so let's assume that we are already there. Furthermore, we take the Hamiltonian to be spin diagonal and degenerate. The operator basis we use is then[3]

$$\psi^\dagger(\sigma,\mathbf{k}) = (d^\dagger_{\sigma\mathbf{k}}, p^\dagger_{x,\sigma\mathbf{k}}, p^\dagger_{y,\sigma\mathbf{k}}), \tag{2.23}$$

and thus

$$\mathcal{H} = \sum_{\mathbf{k}} \left[\psi^\dagger(\sigma,\mathbf{k}) H_{3\times3}(\mathbf{k})\psi(\sigma,\mathbf{k}) \oplus \psi^\dagger(\bar\sigma,\mathbf{k}) H_{3\times3}(\mathbf{k})\psi(\bar\sigma,\mathbf{k})\right] \tag{2.24}$$

where $\bar\sigma$ is the opposite spin of σ. In order to get the bulk density of states, we first find the Green's function for each **k** in FBZ (the first Brillouin zone). This quantity is given by

$$G(\mathbf{k}) = (1(\omega+i\eta) - [H_{3\times3}(\mathbf{k}) \oplus H_{3\times3}(\mathbf{k})])^{-1} \tag{2.25}$$

$$= (1(\omega+i\eta) - H_{3\times3}(\mathbf{k}))^{-1} \oplus (1(\omega+i\eta) - H_{3\times3}(\mathbf{k}))^{-1}. \tag{2.26}$$

The orbitally-resolved spectral function is then

$$\begin{aligned}\rho_\ell(\omega) &= -\frac{1}{\pi N}\left(\mathrm{Tr}_{\mathbf{k},\sigma}[\mathrm{Im}G]\right)_{\ell,\ell} \\ &= -\frac{1}{\pi N}\left(\mathrm{Tr}_{\mathbf{k},\sigma}[\mathrm{Im}\bigoplus_{\mathbf{k}} G(\mathbf{k},\omega)]\right)_{\ell,\ell} \\ &= -\frac{2}{\pi N}\sum_{\mathbf{k}} \mathrm{Im}(1(\omega+i\eta) - H_{3\times3}(\mathbf{k}))^{-1}_{\ell,\ell}.\end{aligned} \tag{2.27}$$

The virtue of equation (2.27) is its easy numerical evaluation. For a given 3×3 Hamiltonian matrix, we can find the bulk density of states by simply inverting this matrix for each point in the first Brillouin zone and then summing the results and taking the imaginary part. The length of this calculation scales linearly with the system size, and we can therefore easily obtain a rather high resolution/system size.

One more thing deserves mentioning in this example. In the homogeneous case, the bulk density of states must be equal to the spatially resolved density of states for any lattice point. To see that this is indeed the case, we need to introduce the particular Fourier transform convention we use for the three-orbital model. We take

$$d^\dagger_{\mathbf{k}} = \frac{1}{\sqrt{N}}\sum_{\mathbf{r}} d^\dagger_{\mathbf{r}} e^{i\mathbf{k}\cdot\mathbf{r}},\ p^\dagger_{x,\mathbf{k}} = \frac{1}{\sqrt{N}}\sum_{\mathbf{r}} p^\dagger_{x,\mathbf{r}} e^{i\mathbf{k}\cdot(\mathbf{r}+x/2)},\ p^\dagger_{y,\mathbf{k}} = \frac{1}{\sqrt{N}}\sum_{\mathbf{r}} p^\dagger_{y,\mathbf{r}} e^{i\mathbf{k}\cdot(\mathbf{r}+y/2)}. \tag{2.28}$$

[3]Since there are only three orbital quantum numbers, it is customary to write e.g. $d^\dagger_{\sigma,\mathbf{k}}$ instead of $c^\dagger_{\sigma,\mathbf{k},d}$. We shall keep using this notation in the following chapters.

The density of states in the unit cell at $\mathbf{r}'$ is then found as

$$\rho_\ell(\mathbf{r}',\omega) = -\frac{1}{\pi}(\mathrm{Tr}_\sigma \,\mathrm{Im}G(\mathbf{r}',\mathbf{r}',\omega))_{\ell,\ell} = -\frac{1}{\pi}(\mathrm{Tr}_\sigma \,\mathrm{Im}G(\mathbf{r}'-\mathbf{r}',\omega))_{\ell,\ell}. \tag{2.29}$$

The spatial Green's function is given in terms of a Fourier transform as

$$G(\mathbf{r}'-\mathbf{r}',\omega) = \frac{1}{N}\sum_{\mathbf{k}} G(\mathbf{k},\omega).*(F_{3\times3}(\mathbf{k}) \oplus F_{3\times3}(\mathbf{k}))\mathrm{e}^{i\mathbf{k}\cdot(\mathbf{r}'-\mathbf{r}')}, \tag{2.30}$$

where $.*$ denotes elementwise matrix multiplication and

$$F_{3\times3}(\mathbf{k}) = \begin{bmatrix} 1 & \mathrm{e}^{-ik_x/2} & \mathrm{e}^{-ik_y/2} \\ \mathrm{e}^{ik_x/2} & 1 & \mathrm{e}^{i(k_x-k_y)/2} \\ \mathrm{e}^{ik_y/2} & \mathrm{e}^{i(k_y-k_x)/2} & 1 \end{bmatrix}. \tag{2.31}$$

Long story short, we observe that the Fourier transformation for the diagonal elements amounts to performing a $\mathbf{k}$-summation, and it therefore holds that

$$\rho_\ell(\mathbf{r}',\omega) = -\frac{2}{\pi N}\sum_{\mathbf{k}} \mathrm{Im}(1(\omega+i\eta) - H_{3\times3}(\mathbf{k}))^{-1}_{\ell,\ell} = \rho_\ell(\omega), \tag{2.32}$$

just as we expect in the homogeneous case.

2.3 Example 2: A BCS Superconductor

The other important example we should cover is the case of a homogeneous BCS type superconductor treated in mean-field. We shall not derive this model from the underlying electron-phonon interaction (for this derivation, consult [23, Chapter 18] or [25, Chapter 3]), but instead start with the mean-field model and use it to shed some light on how we calculate Green's functions. For simplicity, and in order to highlight what is special about superconducting Green's functions, we assume a one-band model.

The basic idea in the mean-field approach to such a system is the assumption of non-vanishing Cooper-pair expectation values, i.e., that $\langle c^\dagger_\nu c^\dagger_\mu\rangle \neq 0$ and $\langle c_\nu c_\mu\rangle \neq 0$ for some ν and μ. We take $\nu = (\uparrow,\mathbf{k})$ and $\mu = (\downarrow,-\mathbf{k})$ as is standard for singlet BCS pairing. The operator basis we work with - known as the Nambu formalism basis (after ref. [26]) - is then given by

$$\psi^\dagger(\mathbf{k}) = (c^\dagger_{\uparrow\mathbf{k}}, c_{\downarrow-\mathbf{k}}), \tag{2.33}$$

and

$$\mathcal{H} = \sum_{\mathbf{k}} \psi^\dagger(\mathbf{k}) \begin{bmatrix} \xi(\mathbf{k}) & \Delta(\mathbf{k}) \\ \Delta^*(\mathbf{k}) & -\xi(\mathbf{k}) \end{bmatrix} \psi(\mathbf{k}), \tag{2.34}$$

where $\xi(\mathbf{k})$ is the normal state dispersion and $\Delta(\mathbf{k})$ is the so-called gap function. The name of $\Delta(\mathbf{k})$ arises from the fact that the eigenvalues of this system are now given by

$$E_{\mathbf{k}} = \pm\sqrt{\xi(\mathbf{k})^2 + |\Delta(\mathbf{k})|^2}, \tag{2.35}$$

and no exitations with energy less than $|\Delta(\mathbf{k})|$ therefore are possible. The $\mathbf{k}$-components of the Green's function are found in accordance with equation (2.18);

$$\begin{aligned} G(\mathbf{k},\omega) &= \begin{bmatrix} \omega+i\eta-\xi(\mathbf{k}) & -\Delta(\mathbf{k}) \\ -\Delta^*(\mathbf{k}) & \omega+i\eta+\xi(\mathbf{k}) \end{bmatrix}^{-1} \\ &= \frac{1}{(\omega+i\eta)^2 - E^2_{\mathbf{k}}} \begin{bmatrix} (\omega+i\eta)+\xi(\mathbf{k}) & \Delta(\mathbf{k}) \\ \Delta^*(\mathbf{k}) & (\omega+i\eta)-\xi(\mathbf{k}) \end{bmatrix}. \end{aligned} \tag{2.36}$$

Now, before computing the density of states, a bit of caution must be taken. Due to the ordering of operators in our definition of the Nambu spinors, it is not obvious which correlation functions the entries of the matrix in (2.36) correspond to. To see this, it is perhaps easiest to write the Green's function, $\mathcal{G}$, in the imaginary time formalism ([23, Chapters 11 and 18]). Then

$$\mathcal{G}(\mathbf{k},\tau) = -\left\langle T_\tau \psi(\mathbf{k},\tau)\psi^\dagger(\mathbf{k},0)\right\rangle = \begin{bmatrix} -\left\langle T_\tau c_{\uparrow\mathbf{k}}(\tau)c^\dagger_{\uparrow\mathbf{k}}(0)\right\rangle & -\left\langle T_\tau c_{\uparrow\mathbf{k}}(\tau)c_{\uparrow-\mathbf{k}}(0)\right\rangle \\ -\left\langle T_\tau c^\dagger_{\uparrow-\mathbf{k}}(\tau)c^\dagger_{\uparrow\mathbf{k}}(0)\right\rangle & -\left\langle T_\tau c^\dagger_{\downarrow-\mathbf{k}}(\tau)c_{\downarrow-\mathbf{k}}(0)\right\rangle \end{bmatrix}, \quad (2.37)$$

and we see that $\mathcal{G}_{11}(\mathbf{k},\tau) = \mathcal{G}_{\uparrow\uparrow}(\mathbf{k},\tau)$, whereas $\mathcal{G}_{22}(\mathbf{k},\tau) = \mathcal{G}^*_{\downarrow\downarrow}(-\mathbf{k},\tau)$, if we understand $\mathcal{G}_{\sigma\sigma'}(\mathbf{k},\tau)$ to be the physical correlation function between the spins σ and σ'. When we want to calculate the density of states and thus want to trace over all quantum numbers, we have to take into consideration that taking the trace of our Nambu Green's function does *not* correspond to taking the desired spin trace.

Usually, to get physical results, one wants to calculate the density of states not as a function of imaginary time, but of real frequency (energy). Upon Fourier transformation, we get that[4]

$$\mathcal{G}_{22}(\mathbf{k}, i\omega_n) = \mathcal{G}^*_{\downarrow\downarrow}(-\mathbf{k}, -i\omega_n), \quad (2.38)$$

which we then analytically continue to yield that (understanding that $-\omega$ means $-\omega - i\eta$)

$$G_{22}(\mathbf{k},\omega) = G^*_{\downarrow\downarrow}(-\mathbf{k},-\omega). \quad (2.39)$$

The prescription to calculate the density of states for a BCS superconductor is then very similar to the prescription given in equation (2.27). If we understand $H(\mathbf{k})$ to be the 2×2 matrix of equation (2.34), we then have ρ given by

$$\rho(\omega) = -\frac{1}{\pi N}\sum_{\mathbf{k}} \mathrm{Im}(1(\omega+i\eta - H(\mathbf{k}))^{-1}_{11} + \mathrm{Im}[(-1(\omega+i\eta) - H(-\mathbf{k}))^{-1}_{22}]^* \quad (2.40)$$

$$= -\frac{1}{\pi N}\sum_{\mathbf{k}} \mathrm{Im}(1(\omega+i\eta - H(\mathbf{k}))^{-1}_{11} - \mathrm{Im}(-1(\omega+i\eta) - H(-\mathbf{k}))^{-1}_{22}, \quad (2.41)$$

which is slightly more cumbersome to evaluate than equation (2.27), but still rather straightforward to compute.

In our simple one-band model where we have an analytical expression for $G(\mathbf{k},\omega)$ (equation (2.36)), we can of course just go ahead and find a closed-form expression for ρ.

What we have in our Nambu matrix is

$$\begin{aligned} G^*_{\downarrow\downarrow}(-\mathbf{k},-(\omega+i\eta)) &= \frac{(\omega+i\eta)-\xi(\mathbf{k})}{\omega^2-\eta^2+2i\omega\eta - E^2(\mathbf{k})} \\ &= \frac{(\omega+i\eta-\xi(\mathbf{k}))(\omega^2-\eta^2-2i\eta\omega-E^2(\mathbf{k})}{(\omega^2-\eta^2-E^2(\mathbf{k}))^2+4\eta^2\omega^2}. \end{aligned}$$

What we would like to have is[5]

$$\begin{aligned} G_{\downarrow\downarrow}(-\mathbf{k},\omega+i\eta) &= \left(\frac{-\omega-i\eta-\xi(\mathbf{k})}{(\omega+i\eta)^2-E^2(\mathbf{k})}\right)^* \\ &= \left(\frac{(-\omega-i\eta-\xi(\mathbf{k}))(\omega^2-\eta^2-2i\eta\omega-E^2(\mathbf{k}))}{(\omega^2-\eta^2-E^2(\mathbf{k}))^2+4\eta^2\omega^2)}\right)^* \\ &= \frac{(-\omega+i\eta-\xi(\mathbf{k}))(\omega^2-\eta^2+2i\eta\omega-E^2(\mathbf{k}))}{(\omega^2-\eta^2-E^2(\mathbf{k}))^2+4\eta^2\omega^2}. \end{aligned}$$

[4] Using the following fact from Fourier analysis: $\mathcal{F}[f^*](p) = (\mathcal{F}[f](-p))^*$. See e.g. [27].

[5] Getting $G^*_{\downarrow\downarrow}(-\mathbf{k})$ instead of $G^*_{\downarrow\downarrow}(\mathbf{k})$ is okay, since $\sum_{\mathbf{k}} G^*_{\downarrow\downarrow}(-\mathbf{k}) = \sum_{\mathbf{k}} G^*_{\downarrow\downarrow}(\mathbf{k})$.

By comparison, this is equal to what is standing in the Nambu matrix, *with only the sign of ω changed*. The complex conjugation takes care of the sign of η for us.

The corresponding density of states can now explicitly be found as

$$\begin{aligned} d(\omega) &= \mathrm{Tr}_{\mathbf{k},\sigma}(A(\mathbf{k},\omega)) \\ &= -\frac{1}{\pi N}\sum_{\mathbf{k}} 2\mathrm{Im}(G_{\uparrow\uparrow}(\mathbf{k},\omega+i\eta)+G_{\downarrow\downarrow}(\mathbf{k},\omega+i\eta)) \\ &= -\frac{1}{\pi N}\sum_{\mathbf{k}} 2\mathrm{Im}(G_{11}(\mathbf{k},\omega+i\eta)+G_{22}(-\mathbf{k},-\omega+i\eta) \\ &= -\frac{1}{\pi N}\sum_{\mathbf{k}} 2\mathrm{Im}\left(\frac{\omega+i\eta+\xi(\mathbf{k})}{(\omega+i\eta)^2-E_{\mathbf{k}}^2}+\frac{-\omega+i\eta-\xi(\mathbf{k})}{(\omega-i\eta)^2-E_{\mathbf{k}}^2}\right) \\ &= \frac{1}{\pi N}\sum_{\mathbf{k}} \frac{4\eta(\omega^2+\eta^2+E_{\mathbf{k}}^2+\omega\xi(\mathbf{k}))}{(\omega^2-\eta^2-E_{\mathbf{k}}^2)^2+4\omega^2\eta^2}. \end{aligned} \tag{2.42}$$

We mention this mainly for completeness, as it is not our goal to study the one-band BCS superconductor, although it is a fascinating system. The interested reader may consult references [23], [24] and [25]. We shall, however, use the BCS theory as a means of getting superconductivity into our three-band model, where it will play an important role.

2.4 Our model: Three-band superconductor

Finally, we consider the combination of the three-band model and the BCS model. It is this model we really expect to yield interesting results once the orbital currents start flowing (they will do so in Chapter 3). For now we find the density of states-prescription, i.e., the analogue of equations (2.27) and equation (2.41) for a three-band superconductor.

For a homogeneous system, the Hamiltonian will be 6×6 block diagonal in $\mathbf{k}$-space, as there are three orbitals and no spin degeneracy. We choose the operator basis given by

$$\psi^\dagger(\mathbf{k}) = (d^\dagger_{\uparrow\mathbf{k}}, p^\dagger_{x,\uparrow\mathbf{k}}, p^\dagger_{y,\uparrow\mathbf{k}}, d_{\downarrow-\mathbf{k}}, p_{x,\downarrow-\mathbf{k}}, p_{y,\downarrow-\mathbf{k}}). \tag{2.43}$$

If we then let $\mathcal{H} = \sum_{\mathbf{k}} \psi^\dagger(\mathbf{k})H(\mathbf{k})\psi(\mathbf{k})$, $H_{3b}(\mathbf{k})$ be the three band Hamiltonian matrix of equation (2.24), and define two matrices U and D by

$$U := \begin{bmatrix} 1 & 0 \\ 0 & 0 \end{bmatrix}, \qquad D := \begin{bmatrix} 0 & 0 \\ 0 & 1 \end{bmatrix}, \quad \text{and let} \quad \sigma_x = \begin{bmatrix} 0 & 1 \\ 1 & 0 \end{bmatrix}, \tag{2.44}$$

we find that

$$\mathcal{H} = \sum_{\mathbf{k}} \psi^\dagger(\mathbf{k}) \underbrace{[U\otimes H_{3b}(\mathbf{k}) - D\otimes H^*_{3b}(-\mathbf{k}) + \sigma_x\otimes\Delta(\mathbf{k})]}_{H(\mathbf{k})} \psi(\mathbf{k}), \tag{2.45}$$

where $\Delta(\mathbf{k})$ is a 3×3 matrix (which we have already taken to be real), that encodes how superconductivity behaves in our system. How should we choose $\Delta(\mathbf{k})$? Now, we have already mentioned in a previous chapter that we want to study $d_{x^2-y^2}$-superconductivity, since this experimentally have been verified to be relevant for the cuprates (see e.g. ref. [6] and the references herein). We hence already know what the $\mathbf{k}$-dependence of Δ should be. A more pressing question is which orbitals we expect to contribute to the Cooper-pair condensation. In a realistic model, we should diagonalize the bare Hamiltonian (of equation (2.24)), find the fermi energy and the corresponding band, the orbital contributions to this band, and then put the superconductivity on these orbitals with the appropriate weights. However, since we are

interested in studying the phenomenological behaviour of a cuprate with orbital currents and superconductivity, rather than deriving this coexistence from some underlying model (which would in any case have to be chosen somewhat arbitrarily), we shall instead simply put in the superconductivity by hand on the copper. In formulas, our choice amounts to having

$$\Delta(\mathbf{k}) = \begin{bmatrix} \Delta_0(\cos(k_x) - \cos(k_y)) & 0 & 0 \\ 0 & 0 & 0 \\ 0 & 0 & 0 \end{bmatrix}. \tag{2.46}$$

The final and most complicated formula for the density of states on a given orbital is then, in terms of the $H(\mathbf{k})$ of equation (2.45),

$$\rho_\ell(\omega) = -\frac{1}{\pi N} \sum_{\mathbf{k}} \mathrm{Im}(1(\omega + i\eta - H(\mathbf{k}))^{-1}_{aa} - \mathrm{Im}(-1(\omega + i\eta) - H(-\mathbf{k}))^{-1}_{bb}, \tag{2.47}$$

where ℓ, a, and b are connected via the following table:

ℓ	a	b
d	1	4
p_x	2	5
p_y	3	6

2.5 Summary

This is how far we can go without numerical aid. For all three concrete models, the final quantity of interest, equations (2.27), (2.41), and (2.47) involves a $\mathbf{k}$-sum that we are not able to perform analytically[6], and we must therefore enter the world of numerical computations in order to find an actual value for the density of states.

This concludes our chapter on formalism and methods. The notation, main calculational goals, and how to achieve these have now been clarified. In the next chapter we introduce the mean-field current theory and discuss how to choose the appropriate 3×3 matrix for equation (2.45). In the chapter after that we introduce an impurity, put our faith in numerics and produce some results that we believe to be a loop current signature.

[6]For the one-band BCS superconductor, we might be able to find some approximations and make progress, but for the three-band cases this is not feasible for our purposes.

Chapter 3

The Circulating Currents

With the formal developments in place, we now turn to a study of the circulating current phase. The main goal of this chapter is to show that a mean-field decoupling as performed in [12] and [28] actually leads to a pattern of circulating intra-unit cell currents, and that the expectation values of these currents are consistent with current conservation through each orbital. We shall take this latter requirement as a proof of the physical interpretation of the mean-field parameter of the currents as being actual currents, or, in other words, that we understand the presence of currents in our model. There are some differences in our approach as compared to the to quoted works. Following [28] but as opposed to [12], we do not rewrite the Hamiltonian in terms of flux through each unit cell, but instead keep the direct formulation in terms of the immediate parameter. To keep the parameter space as small as possible, we deviate from the procedure in [28], in that we retain one current parameter for all the intra-unit cell currents, instead of having one parameter for the copper-oxygen currents and another one for the oxygen-oxygen currents.

After having obtained our desired Hamiltonian(s), and established possible self-consistency and definite current conservation, we investigate whether the mean-field current parameter yields any non-trivial physical predictions. The conclusion will be that currents in a homogeneous system do not significantly alter the (L)DOS. The next chapter therefore investigates currents in the presence of impurities and also includes superconductivity.

3.1 The loop-current Hamiltonian(s)

The starting point is an Emery model [22] with explicit orbital operator notation;

$$\mathcal{H} = \mathcal{H}_0 + \mathcal{H}_{int}, \tag{3.1}$$

with

$$\begin{aligned}\mathcal{H}_0 = &\sum_{\mathbf{r},\sigma} \epsilon_d n_{d,\sigma\mathbf{r}} + \epsilon_p (n_{p_x,\sigma\mathbf{r}} + n_{p_y,\sigma\mathbf{r}}) \\ &+ t_{pd} \sum_{\mathbf{r},\sigma} d^\dagger_{\sigma\mathbf{r}} (p_{x,\sigma\mathbf{r}} - p_{x,\sigma\mathbf{r}-x} - p_{y,\sigma\mathbf{r}} + p_{y,\sigma\mathbf{r}-y}) + H.c. \\ &+ t_{pp} \sum_{\mathbf{r},\sigma} p^\dagger_{x,\sigma\mathbf{r}} (p_{y,\sigma\mathbf{r}} - p_{y,\sigma\mathbf{r}-y} - p_{y,\sigma\mathbf{r}+x} + p_{y,\sigma\mathbf{r}+x-y}) + H.c.\end{aligned} \tag{3.2}$$

and

$$\mathcal{H}_{int} = V_{pd} \sum_{\mathbf{r},\sigma\sigma'} n_{d,\sigma\mathbf{r}}(n_{p_x,\sigma'\mathbf{r}} + n_{p_y,\sigma'\mathbf{r}} + n_{p_x,\sigma'\mathbf{r}-x} + n_{p_y,\sigma'\mathbf{r}-y}) + U_d \sum_{\mathbf{r},\sigma} n_{d,\sigma\mathbf{r}} n_{d,\bar{\sigma}\mathbf{r}} + U_p \sum_{\mathbf{r},\sigma} (n_{p_x,\sigma\mathbf{r}} n_{p_x,\bar{\sigma}\mathbf{r}} + n_{p_y,\sigma\mathbf{r}} n_{p_y,\bar{\sigma}\mathbf{r}}) \tag{3.3}$$

where ϵ_d and ϵ_p are the orbital energies, the t_{pd} and t_{pp} are hopping integrals, and U_d, U_p, and V_{pd} are the interaction strengths. The $\bar{\sigma}$ is understood to mean the opposite spin of σ. At this point, it is appropriate to address the issue of orbital sign conventions. As the reader will notice, we have effectively used opposite signs for the t_{pd} connected with copper-oxygen hopping in the x- and y-directions, respectively. This is merely a convention, amounting to choosing one certain unit cell instead of a different one. This is illustrated in Figure 3.1. The sign of t_{pp} then follows from the overlap of the two p-orbitals, and will in our case be positive (see also [29]).

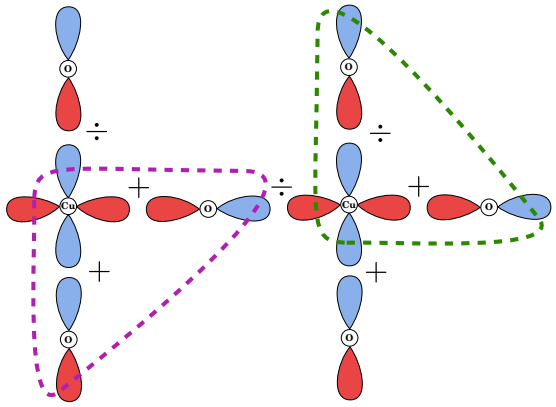

Figure 3.1: By choice of unit cell, all sign combinations for the t_{pd} can be obtained. We use the green unit cell. By counting colours, it is seen how the sign of t_{pp} follows from the signs on t_{pd} in each direction.

We must also address the presence of the U_d and U_p. By applying mean-field theory to the terms they appear in front of, the resulting approximated terms can be re-absorbed into the coefficients ϵ_d and ϵ_p and thus renormalizing them (or, equivalently, the chemical potential). We do not go into great detail regarding the U_d and U_p. From now on, they will be assumed to have been absorbed into the other constants of the theory. Our main focus lies with the oxygen-copper repulsion and the consequences in mean-field of having these terms. We therefore never address the question of what the actual values of U_d and U_p are, except in an indirect way through the choice of numerical values for the input parameters.

To get currents into the picture, one must decouple the copper-oxygen interaction term in the Fock channel (as in [28]) and then make an assumption regarding what terms to disregard.

The first thing to be noted is that a rewriting of the interaction term is

$$\tilde{V} = V_{pd} \sum_{\mathbf{r},m,\sigma,\sigma'} \mathcal{A}^\dagger_{m\mathbf{r}\sigma} \mathcal{A}_{m\mathbf{r}\sigma'}, \tag{3.4}$$

where

$$\mathcal{A}^\dagger_{(1,2),\mathbf{r},\sigma} = \frac{1}{2}[(d^\dagger p_{x,\mathbf{r}\sigma} + d^\dagger p_{x,\mathbf{r}-x\sigma}) \pm (d^\dagger p_{y,\mathbf{r}\sigma} + d^\dagger p_{y,\mathbf{r}-y\sigma})] \tag{3.5}$$

$$\mathcal{A}^\dagger_{(3,4),\mathbf{r},\sigma} = \frac{i}{2}[(d^\dagger p_{x,\mathbf{r}\sigma} - d^\dagger p_{x,\mathbf{r}-x\sigma}) \pm (d^\dagger p_{y,\mathbf{r}\sigma} - d^\dagger p_{y,\mathbf{r}-y\sigma})]. \tag{3.6}$$

If we write this out we see that

$$\tilde{V} = V_{pd} \sum_{\mathbf{r},\sigma,\sigma'} \sum_{a=x,y} d^\dagger_{\mathbf{r}\sigma}(p_{a,\mathbf{r}+a,\sigma} p^\dagger_{a,\mathbf{r}+a\sigma'} + p_{a,\mathbf{r}-a,\sigma} p^\dagger_{a,\mathbf{r}-a\sigma'}) d_{\mathbf{r}\sigma'} \tag{3.7}$$

$$= V_{pd} \sum_{\mathbf{r}.\sigma,\sigma'} \sum_{a=x,y} d^\dagger_{\mathbf{r}\sigma} d_{\mathbf{r}\sigma'}(\delta_{\sigma\sigma'} - p^\dagger_{a,\mathbf{r}+a\sigma'} p_{a,\mathbf{r}+a,\sigma} + \delta_{\sigma\sigma'} - p^\dagger_{a,\mathbf{r}-a\sigma'} p_{a,\mathbf{r}-a,\sigma}). \tag{3.8}$$

Now, this is the same as minus the copper-oxygen interaction in (3.3), provided we renormalise the ϵ_d in (3.2) (due to the $\delta_{\sigma\sigma'}$) and furthermore let all operators act completely independent of their spin index, i.e., $d_\uparrow \equiv d_\downarrow$. To emphasize the latter requirement and make the notation as clear as possible, we suppress spin indices for the remainder of this chapter; the spin will appear only as a factor of 2 in front of sums.

The next thing to do is then the actual decoupling. The way we do this has already been anticipated by the notation. We introduce the complex mean-field parameter R defined by

$$R_m = 2V_{pd} \langle \mathcal{A}_m \rangle . \tag{3.9}$$

Then

$$-4V_{pd} \sum_{\mathbf{r},m} \mathcal{A}^\dagger_{\mathbf{r}m} \mathcal{A}_{\mathbf{r}m} \approx -2 \sum_{\mathbf{r},m} (R_m \mathcal{A}^\dagger_{\mathbf{r},m} + \text{H.c.}) + \frac{1}{2V_{pd}} \sum_m |R_m|^2. \tag{3.10}$$

For our calculations we always disregard the constant term, as it only corresponds to an absolute shift of energies. Furthermore, the main assumption we make in order to have obtain a loop-current Hamiltonian, is that only one $\mathcal{A}_m$ has a non-vanishing expectation value (at a time). We thus have four different loop-current Hamiltonians.

The translation invariance of the system is begging us to Fourier transform. As mentioned in the previous chapter, we employ a Fourier transform that explicitly takes inner-unit cell distances into account:

$$d^\dagger_{\mathbf{k}} = \frac{1}{\sqrt{N}} \sum_{\mathbf{r}} d^\dagger_{\mathbf{r}} e^{i\mathbf{k}\cdot\mathbf{r}},\ p^\dagger_{x,\mathbf{k}} = \frac{1}{\sqrt{N}} \sum_{\mathbf{r}} p^\dagger_{x,\mathbf{r}} e^{i\mathbf{k}\cdot(\mathbf{r}+x/2)},\ p^\dagger_{y,\mathbf{k}} = \frac{1}{\sqrt{N}} \sum_{\mathbf{r}} p^\dagger_{y,\mathbf{r}} e^{i\mathbf{k}\cdot(\mathbf{r}+y/2)}. \tag{3.11}$$

Doing so yields a 3×3-block diagonal $\mathbf{k}$-space Hamiltonian matrix[1] in the operator basis given by

$$\psi^\dagger(\mathbf{k}) = [d^\dagger_{\mathbf{k}}, p^\dagger_{x,\mathbf{k}}, p^\dagger_{y,\mathbf{k}}]. \tag{3.12}$$

It has the form:

$$\mathcal{H}_0 = \sum_{\mathbf{k}} \psi^\dagger(\mathbf{k}) \begin{bmatrix} \epsilon_d & 2it_{pd}s_x & -2it_{pd}s_y \\ -2it_{pd}s_x & \epsilon_p & 4t_{pp}s_x s_y \\ 2it_{pd}s_y & 4t_{pp}s_x s_y & \epsilon_p \end{bmatrix} \psi(\mathbf{k}). \tag{3.13}$$

The decoupled interactions take the forms

$$\sum_{\mathbf{r}} \mathcal{A}^\dagger_{(1,2),\mathbf{r}} = \sum_{\mathbf{k}} c_x d^\dagger_{\mathbf{k}} p_{x,\mathbf{k}} \pm c_y d^\dagger_{\mathbf{k}} p_{y,\mathbf{k}}, \tag{3.14}$$

$$\sum_{\mathbf{r}} \mathcal{A}^\dagger_{(3,4),\mathbf{r}} = \sum_{\mathbf{k}} -(s_x d^\dagger_{\mathbf{k}} p_{x,\mathbf{k}} \pm s_y d^\dagger_{\mathbf{k}} p_{y,\mathbf{k}}), \tag{3.15}$$

[1] The aforementioned orbital convention is perhaps more obvious in this form.

and we end up with four different **k**-space Hamiltonians:

$$\mathcal{H}_1 = \sum_{\mathbf{k}} \psi^\dagger(\mathbf{k}) \begin{bmatrix} \epsilon_d & 2it_{pd}s_x - R_1 c_x & -2it_{pd}s_y - R_1 c_y \\ -2it_{pd}s_x - R_1^* c_x & \epsilon_p & 4t_{pp}s_x s_y \\ 2it_{pd}s_y - R_1^* c_y & 4t_{pp}s_x s_y & \epsilon_p \end{bmatrix} \psi(\mathbf{k}) \tag{3.16}$$

$$\mathcal{H}_2 = \sum_{\mathbf{k}} \psi^\dagger(\mathbf{k}) \begin{bmatrix} \epsilon_d & 2it_{pd}s_x - R_2 c_x & -2it_{pd}s_y + R_2 c_y \\ -2it_{pd}s_x - R_2^* c_x & \epsilon_p & 4t_{pp}s_x s_y \\ 2it_{pd}s_y + R_2^* c_y & 4t_{pp}s_x s_y & \epsilon_p \end{bmatrix} \psi(\mathbf{k}) \tag{3.17}$$

$$\mathcal{H}_3 = \sum_{\mathbf{k}} \psi^\dagger(\mathbf{k}) \begin{bmatrix} \epsilon_d & 2it_{pd}s_x + R_3 s_x & -2it_{pd}s_y + R_3 s_y \\ -2it_{pd}s_x + R_3^* s_x & \epsilon_p & 4t_{pp}s_x s_y \\ 2it_{pd}s_y + R_3^* s_y & 4t_{pp}s_x s_y & \epsilon_p \end{bmatrix} \psi(\mathbf{k}) \tag{3.18}$$

$$\mathcal{H}_4 = \sum_{\mathbf{k}} \psi^\dagger(\mathbf{k}) \begin{bmatrix} \epsilon_d & 2it_{pd}s_x + R_4 s_x & -2it_{pd}s_y - R_4 s_y \\ -2it_{pd}s_x + R_4^* s_x & \epsilon_p & 4t_{pp}s_x s_y \\ 2it_{pd}s_y - R_4^* s_y & 4t_{pp}s_x s_y & \epsilon_p \end{bmatrix} \psi(\mathbf{k}) \tag{3.19}$$

We shall use these for calculating current expectation values, and in the next chapter to perform impurity scattering calculations. Furthermore, we shall from now on abuse our own notation somewhat, and label these four decouplings as $\mathcal{A} = 1, 2, 3, 4$. By (e.g.) taking $\mathcal{A} = 1$ we mean that the decoupling of the interaction had a non-vanishing $\langle \mathcal{A}_{1,\mathbf{r},\sigma} \rangle$, and not that the $\mathcal{A}$-operator is equal to unity. This should not cause any confusion.

3.2 The current operators

What is a current? Physically, we can think of it as something breaking time reversal symmetry, which is - as discussed in chapter 1 - of course an important property of the proposed pseudogap ground state. But more specifically, a non-vanishing current should correspond to a non-vanishing expectation value of some operator. Which one? The $\mathcal{A}$-operators themselves are not current operators. One might naïvely take $\hat{j}_{a\to b} = a^\dagger b - b^\dagger a$, which has the nice properties that $\hat{j}^\dagger_{a\to b} = -\hat{j}_{a\to b} = \hat{j}_{b\to a}$. However, this leads to current patterns without current conservation[2], a thing we deem unphysical. We shall therefore define the current operators through demanding current conservation. The starting point is the continuity equation:

$$\dot{n}_{d,\mathbf{r}} = -\nabla \cdot \hat{\boldsymbol{\jmath}}_{d,\mathbf{r}} = -(\hat{j}^x_{d,\mathbf{r}} - \hat{j}^x_{d,\mathbf{r}-x} + \hat{j}^y_{d,\mathbf{r}} - \hat{j}^y_{d,\mathbf{r}-y}). \tag{3.20}$$

Secondly, current conservation means that $\dot{n}_{d,\mathbf{r}} = 0$. We calculate the time derivative using the Heisenberg equation. We do this in detail for the $\mathcal{A} = 1$ case. The three other cases can then easily be covered by small sign changes in the result.

$$\begin{aligned} i[\mathcal{H}_1, n_{d,\mathbf{r}}] =& \frac{i}{2}[(2t_{pd} - R_1 \mathrm{e}^{i\phi_1}) d^\dagger_{\mathbf{r}} p_{x,\mathbf{r}} - (R_1 \mathrm{e}^{i\phi_1} + 2t_{pd}) d^\dagger_{\mathbf{r}} p_{x,\mathbf{r}-x} \\ & - (R_1 \mathrm{e}^{i\phi_1} + 2t_{pd}) d^\dagger_{\mathbf{r}} p_{y,\mathbf{r}} + (2t_{pd} - R_1 \mathrm{e}^{i\phi_1}) d^\dagger_{\mathbf{r}} p_{y,\mathbf{r}-y} + H.c., n_{d,\mathbf{r}}]. \end{aligned} \tag{3.21}$$

Using the general fermionic result that

$$[A c^\dagger_\nu c_\mu + A^* c^\dagger_\mu c_\nu, n_\nu] = -A c^\dagger_\nu c_\mu + A^* c^\dagger_\mu c_\nu, \tag{3.22}$$

we then get for the time derivative of $n_{d,\mathbf{r}}$ that

$$\begin{aligned} i[\mathcal{H}_1, n_{d,\mathbf{r}}] =& \frac{i}{2}[(R_1 - 2t_{pd}) d^\dagger_{\mathbf{r}} p_{x,\mathbf{r}} + (R_1 + 2t_{pd}) d^\dagger_{\mathbf{r}} p_{x,\mathbf{r}-x} \\ & + (R_1 + 2t_{pd}) d^\dagger_{\mathbf{r}} p_{y,\mathbf{r}} + (R_1 - 2t_{pd}) d^\dagger_{\mathbf{r}} p_{y,\mathbf{r}-y} - H.c.]. \end{aligned} \tag{3.23}$$

[2]This is not apparent from the equations, but turns out as one performs a numerical calculation.

The current operator identification is straightforward. We let $\hat{j}^R_{d,\mathbf{r}}$ correspond to the current going *right* from the d-orbital in the unit cell at $\mathbf{r}$. Then

$$\hat{j}^R_{d,\mathbf{r}} = -\frac{i}{2}[(R_1 - 2t_{pd})d^\dagger_{\mathbf{r}}p_{x,\mathbf{r}} + (2t_{pd} - R_1^*)p^\dagger_{x,\mathbf{r}}d_{\mathbf{r}}], \tag{3.24}$$

$$\hat{j}^U_{d,\mathbf{r}} = -\frac{i}{2}[(R_1 + 2t_{pd})d^\dagger_{\mathbf{r}}p_{y,\mathbf{r}} - (2t_{pd} + R_1^*)p^\dagger_{y,\mathbf{r}}d_{\mathbf{r}}], \tag{3.25}$$

$$\hat{j}^L_{d,\mathbf{r}} = -\frac{i}{2}[(R_1 + 2t_{pd})d^\dagger_{\mathbf{r}}p_{x,\mathbf{r}-x} - (2t_{pd} + R_1^*)p^\dagger_{x,\mathbf{r}-x}d_{\mathbf{r}}], \tag{3.26}$$

$$\hat{j}^D_{d,\mathbf{r}} = -\frac{i}{2}[(R_1 - 2t_{pd})d^\dagger_{\mathbf{r}}p_{y,\mathbf{r}-y} + (2t_{pd} + R_1^*)p^\dagger_{y,\mathbf{r}-y}d_{\mathbf{r}}], \tag{3.27}$$

and we thus conclude that the relevant expectation values are[3]

$$\langle \hat{j}^R_{d,\mathbf{r}} \rangle = 2\mathrm{Im}\left\langle (R_1 - 2t_{pd})d^\dagger_{\mathbf{r}}p_{x,\mathbf{r}} \right\rangle, \tag{3.28}$$

$$\langle \hat{j}^U_{d,\mathbf{r}} \rangle = 2\mathrm{Im}\left\langle (R_1 + 2t_{pd})d^\dagger_{\mathbf{r}}p_{y,\mathbf{r}} \right\rangle, \tag{3.29}$$

$$\langle \hat{j}^L_{d,\mathbf{r}} \rangle = 2\mathrm{Im}\left\langle (R_1 - 2t_{pd})d^\dagger_{\mathbf{r}}p_{x,\mathbf{r}-x} \right\rangle, \tag{3.30}$$

and

$$\langle \hat{j}^D_{d,\mathbf{r}} \rangle = 2\mathrm{Im}\left\langle (R_1 + 2t_{pd})d^\dagger_{\mathbf{r}}p_{y,\mathbf{r}-y} \right\rangle, \tag{3.31}$$

respectively.

In a similar vein, we find for the p_x-p_y-currents that

$$\dot{n}_{p_x,\mathbf{r}} = \frac{i}{2}[(2t_{pd} + R_1^*)p^\dagger_{x,\mathbf{r}}d_{\mathbf{r}} + (R_1^* - 2t_{pd})p^\dagger_{x,\mathbf{r}}d_{\mathbf{r}+x} \tag{3.32}$$

$$+ 2t_{pp}p^\dagger_{x,\mathbf{r}}(p_{y,\mathbf{r}} - p_{y,\mathbf{r}-y} - p_{y,\mathbf{r}+x} + p_{x,\mathbf{r}+x-y}) + H.c., n_{p_x,\mathbf{r}}] \tag{3.33}$$

$$= -\frac{i}{2}[(2t_{pd} + R_1^*)p^\dagger_{x,\mathbf{r}}d_{\mathbf{r}} + (R_1^* - 2t_{pd})p^\dagger_{x,\mathbf{r}}d_{\mathbf{r}+x} \tag{3.34}$$

$$+ 2t_{pp}p^\dagger_{x,\mathbf{r}}(p_{y,\mathbf{r}} - p_{y,\mathbf{r}-y} - p_{y,\mathbf{r}+x} + p_{x,\mathbf{r}+x-y}) - H.c.]. \tag{3.35}$$

We note the presence of currents from (or to) the d-orbital, which of course comes as no surprise. The remaining terms are then identified as p_x-p_y-currents, leading to the expectation values

$$\langle \hat{j}^{NW}_{x,\mathbf{r}} \rangle = 4t_{pp}\mathrm{Im}\left\langle p^\dagger_{x,\mathbf{r}}p_{y,\mathbf{r}} \right\rangle, \ \langle \hat{j}^{NE}_{x,\mathbf{r}} \rangle = -4t_{pp}\mathrm{Im}\left\langle p^\dagger_{x,\mathbf{r}+x}p_{y,\mathbf{r}} \right\rangle \tag{3.36}$$

$$\langle \hat{j}^{SW}_{x,\mathbf{r}} \rangle = -4t_{pp}\mathrm{Im}\left\langle p^\dagger_{x,\mathbf{r}}p_{y,\mathbf{r}} \right\rangle, \ \langle \hat{j}^{SE}_{x,\mathbf{r}} \rangle = 4t_{pp}\mathrm{Im}\left\langle p^\dagger_{x,\mathbf{r}}p_{y,\mathbf{r}} \right\rangle. \tag{3.37}$$

By translation invariance, we now have the full current pattern for one copper atom and its four oxygen neighbours (see Figure 3.2).

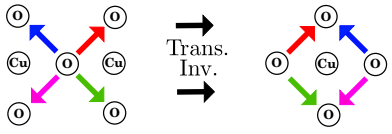

Figure 3.2: It is customary to consider the current configuration to the right.

[3] A factor of 2 for spin and a factor of -2 from $(a - a^*) = 2i\mathrm{Im}(a)$.

3.2.1 Evaluating the current operators

With the proper current operators defined, it is time to actually calculate the current expectation value numbers. We describe this calculation for a general translation invariant three band model. For simplicity, we take the temperature to be zero.

For a homogeneous system, the Hamiltonian is block diagonal in $\mathbf{k}$-space. As above, we write

$$\mathcal{H} = \sum_{\mathbf{k}} \psi^\dagger(\mathbf{k}) H(\mathbf{k}) \psi(\mathbf{k}), \tag{3.38}$$

with $\psi^\dagger(\mathbf{k}) = (d^\dagger_{\mathbf{k}}, p^\dagger_{x,\mathbf{k}}, p^\dagger_{y,\mathbf{k}})$. For a given chemical potential, μ, the ground state of this system is the product of all creation operators creating states of energy less than μ working on the vacuum state. Since we are working within the three-orbital model, H is a 3×3 matrix, and there are - for each given $\mathbf{k}$ - three bands to consider. Let us denote their corresponding annihilation operators by $\alpha_{\mathbf{k}}$, $\beta_{\mathbf{k}}$ and $\gamma_{\mathbf{k}}$, and let $E_\gamma(k)$ be the energy of a particle with momentum $\mathbf{k}$ in the γ-band. We write the band operators as

$$\begin{aligned}
\alpha^\dagger_{\mathbf{k}} &= a_\alpha(\mathbf{k}) d^\dagger_{\mathbf{k}} + b_\alpha(\mathbf{k}) p^\dagger_{x,\mathbf{k}} + c_\alpha(\mathbf{k}) p^\dagger_{y,\mathbf{k}}, \\
\beta^\dagger_{\mathbf{k}} &= a_\beta(\mathbf{k}) d^\dagger_{\mathbf{k}} + b_\beta(\mathbf{k}) p^\dagger_{x,\mathbf{k}} + c_\beta(\mathbf{k}) p^\dagger_{y,\mathbf{k}}, \\
\gamma^\dagger_{\mathbf{k}} &= a_\gamma(\mathbf{k}) d^\dagger_{\mathbf{k}} + b_\gamma(\mathbf{k}) p^\dagger_{x,\mathbf{k}} + c_\gamma(\mathbf{k}) p^\dagger_{y,\mathbf{k}}.
\end{aligned}$$

For simplicity, assume that the band structure and chemical potential are such that the ground state consists solely of particles in the γ-band. Denote the ground state as $|g\rangle$ and define a region $\mathcal{R}_\gamma$ in $\mathbf{k}$-space by

$$\mathcal{R}_\gamma = \{\mathbf{k} \in FBZ \mid E_\gamma(\mathbf{k}) \leq \mu\}. \tag{3.39}$$

Then

$$|g\rangle = \prod_{\mathbf{k} \in \mathcal{R}_\gamma} \gamma^\dagger_{\mathbf{k}} |0\rangle . \tag{3.40}$$

From equations (3.24) to (3.31), we see that any current operator expectation value has the form $\mathrm{Im}\left(A \left\langle c^\dagger_\mu c_\nu \right\rangle\right)$ for some complex number A. How do we find $\left\langle c^\dagger_\mu c_\nu \right\rangle$? Let's take $c^\dagger_\mu = p^\dagger_{x,\mathbf{r}}$ and $c_\nu = p_{y,\mathbf{r}'}$. To evaluate this number, we insert the $\mathbf{k}$-space representation of the operators[4].

$$\left\langle \hat{\jmath}_{p_{x,\mathbf{r}_0} \to p_{y,\mathbf{r}_0}} \right\rangle \propto \mathrm{Im} \langle 0| \prod_{\mathbf{k}'' \in \mathcal{R}_\gamma} \gamma(\mathbf{k}'') \sum_{\mathbf{k},\mathbf{k}'} p^\dagger_{x,\mathbf{k}} p_{y,\mathbf{k}'} \mathrm{e}^{i((\mathbf{r}'+y/2)\cdot\mathbf{k}' - (\mathbf{r}+x/2)\cdot\mathbf{k})} \prod_{\mathbf{k}'' \in \mathcal{R}_\gamma} \gamma^\dagger(\mathbf{k}'') |0\rangle \tag{3.41}$$

Now, for any fixed pair of $\mathbf{k}$, $\mathbf{k}'$, the two operators in the middle can be anti-commuted past the γ's to annihilate the vacuum (to the left respectively right), unless they meet their conjugate operator with the same momentum on the way. In that case

$$\begin{aligned}
\langle 0| \gamma_{\mathbf{k}} p^\dagger_{x,\mathbf{k}} &= \langle 0| \left(a^*_\gamma(\mathbf{k}) d_{\mathbf{k}} + b^*_\gamma(\mathbf{k}) p_{x,\mathbf{k}} + c^*_\gamma(\mathbf{k}) p_{y,\mathbf{k}}\right) p^\dagger_{x,\mathbf{k}} \\
&= \langle 0| \left(-a^*_\gamma(\mathbf{k}) p^\dagger_{x,\mathbf{k}} d_{\mathbf{k}} + b^*_\gamma(\mathbf{k})(1 - p^\dagger_{x,\mathbf{k}} p_{x,\mathbf{k}}) - c^*_\gamma(\mathbf{k}) p^\dagger_{x,\mathbf{k}} p_{y,\mathbf{k}}\right) \\
&= \langle 0| \left(-p^\dagger_{x,\mathbf{k}}\right) \gamma_{\mathbf{k}} + b^*_\gamma = \langle 0| b^*_\gamma(\mathbf{k}).
\end{aligned} \tag{3.42}$$

For clarity we label the momenta in $\mathcal{R}$ as $\mathbf{k}_1, \mathbf{k}_2, \ldots, \mathbf{k}_N$. Using (3.42), we then get that

$$\left\langle \hat{\jmath}_{p_{x,\mathbf{r}_0} \to p_{y,\mathbf{r}_0}} \right\rangle \propto \mathrm{Im} \sum_{\mathbf{k},\mathbf{k}' \in \mathcal{R}_\gamma} \langle 0| \gamma_{\mathbf{k}_1} \cdots b^*(\mathbf{k}) \cdots \gamma_{\mathbf{k}_N} \gamma^\dagger_{\mathbf{k}_N} \cdots c_\gamma(\mathbf{k}') \cdots \gamma^\dagger_{\mathbf{k}_1} |0\rangle \, \mathrm{e}^{i((\mathbf{r}'+y/2)\cdot\mathbf{k}' - (\mathbf{r}-x/2)\cdot\mathbf{k})}. \tag{3.43}$$

[4]The reader is kindly asked to imagine the γ-operators to be ordered correctly.

By construction of the Fock space, this is zero unless the two operator strings of remaining γs are each others conjugation. Therefore $\mathbf{k}$ must be equal to $\mathbf{k}'$, and we arrive at the simple formula

$$\left\langle p^\dagger_{x,\mathbf{r}} p_{y,\mathbf{r}'} \right\rangle = \mathrm{Im} \sum_{\mathbf{k}\in\mathcal{R}_\gamma} b^*_\gamma(\mathbf{k}) c_\gamma(\mathbf{k}) \phi_{\mathbf{r},\mathbf{r}'}(\mathbf{k}), \tag{3.44}$$

where $\phi_{\mathbf{r},\mathbf{r}'}(\mathbf{k}) := \mathrm{e}^{i(\mathbf{r}'+\mathbf{v}(\ell)-\mathbf{r}-\mathbf{v}(\ell'))\cdot\mathbf{k}}$, and $\mathbf{v}$ is the orbital dependent Fourier factor explained in the previous chapter. The number in equation (3.44) is easily evaluated numerically, and is readily modified for another choice of current operator.

Now, what if more than one band were to contribute, i.e., if two bands have overlapping $\mathcal{R}$-regions in momentum space? Let's assume that both $E_\gamma(\mathbf{k}_0)$ and $E_\alpha(\mathbf{k}_0)$ are less than μ. Repeating the above procedure, we need to simplify $\langle 0|\, \gamma_{\mathbf{k}_0}\alpha_{\mathbf{k}_0} p^\dagger_{x,\mathbf{k}_0}$. Using (3.42), we see that

$$\begin{aligned}
\langle 0|\, \gamma_{\mathbf{k}_0}\alpha_{\mathbf{k}_0} p^\dagger_{x,\mathbf{k}_0} &= \langle 0|\, \gamma_{\mathbf{k}_0}[(-p^\dagger_{x,\mathbf{k}_0}\alpha_{\mathbf{k}_0}) + b^*_\alpha(\mathbf{k}_0)] \\
&= \langle 0|\, (p^\dagger_{x,\mathbf{k}_0}\gamma_{\mathbf{k}_0}\alpha_{\mathbf{k}_0} - b^*_\gamma(\mathbf{k}_0)\alpha_{\mathbf{k}_0} + b^*_\alpha\gamma_{\mathbf{k}_0}) \\
&= \langle 0|\, (-b^*_\gamma(\mathbf{k}_0)\alpha_{\mathbf{k}_0} + b^*_\alpha\gamma_{\mathbf{k}_0}).
\end{aligned} \tag{3.45}$$

The same thing of course happens to the ket part of the expectation value (we have already set $\mathbf{k} = \mathbf{k}'$ by the same argument as above). Upon multiplication of the bra and the ket, all cross-terms in the product

$$\langle 0|\, (-b^*_\gamma(\mathbf{k}_0)\alpha_{\mathbf{k}_0} + b^*_\alpha\gamma_{\mathbf{k}_0})(-c_\gamma(\mathbf{k}_0)\alpha^\dagger_{\mathbf{k}_0} + c_\alpha\gamma^\dagger_{\mathbf{k}_0})\, |0\rangle \tag{3.46}$$

will vanish by construction of the Fock space. Furthermore, the a, b, c coefficient products will all be positive. The $\mathbf{k}_0$-term in the momentum sum thus takes the form

$$b^*_\gamma(\mathbf{k}_0)c_\gamma(\mathbf{k}_0) + b^*_\alpha(\mathbf{k}_0)c_\alpha(\mathbf{k}_0), \tag{3.47}$$

and we realize that the generalization of (3.44) to the general situation of arbitrarily many regions of band-overlap is straightforward:

$$\left\langle p^\dagger_{x,\mathbf{r}} p_{y,\mathbf{r}'} \right\rangle = \mathrm{Im} \left[\sum_{\mathbf{k}\in\mathcal{R}_\alpha} b^*_\alpha(\mathbf{k}) c_\alpha(\mathbf{k}) \phi_{\mathbf{r},\mathbf{r}'}(\mathbf{k}) + \sum_{\mathbf{k}\in\mathcal{R}_\beta} b^*_\beta(\mathbf{k}) c_\beta(\mathbf{k}) \phi_{\mathbf{r},\mathbf{r}'}(\mathbf{k}) + \sum_{\mathbf{k}\in\mathcal{R}_\gamma} b^*_\gamma(\mathbf{k}) c_\gamma(\mathbf{k}) \phi_{\mathbf{r},\mathbf{r}'}(\mathbf{k}) \right], \tag{3.48}$$

with obvious modifications for other currents. An interesting consequence of equation (3.48) is the vanishing of orbital currents if all three bands are filled, i.e., $R_\alpha = R_\beta = R_\gamma = FBZ$, since we then sum inner products of different rows of a unitary matrix.

The calculation explained here in great detail is of course completely analogous to the calculation of any expectation value of operator pairs, in particular the calculation of R_m (equation (3.9)). In the next section we extensively compute R_m.

3.3 Self-consistency of the currents

When doing mean-field theory, one must assume a certain value for the mean-field parameter in order to get a Hamiltonian. But with this Hamiltonian, one can calculate what the mean-field parameter actually is. Obviously, the two values should agree; the theory should be *self-consistent*. An equivalent demand is that the value of the mean-field parameter minimizes the free energy of the system (see [23, Chapter 4]).

In this section, we present three different schemes for finding the correct value of the mean-field parameter. To our luck, they turn out to agree with each other. We do not explicitly

mention the chemical potential, but it is present whenever we calculate an expectation value, and it is taken to be zero throughout this section.

We only present results for the case when $\mathcal{A} = 3$, but the 1 and 2 case has essentially the same behaviour. It was, however, not possible to stabilize an order parameter when $\mathcal{A} = 4$.

Upon performing numerical calculations, we of course have to feed the computer with actual values for all the parameters in the theory. Whereas the hopping coefficients are agreed to be $t_{pd} = -1.3$ eV and $t_{pp} = \frac{1}{2}t_{pd}$ (see e.g. [30]), there is some uncertainty regarding the hybridization energies. Varma has $\epsilon_d = \epsilon_p = 0$ (see [12]), whilst a more realistic suggestion is $\epsilon_d = -1.5$ eV and $\epsilon_p = -5$ eV. A discussion of these values can be found in ref. [5]. For the self-consistent calculations presented here, we employed Varma's parameters, but similar results were obtained for the other case. Another issue regarding numerics is the units of the parameters. The computer does not take units as input, and the author admits to sometimes having forgotten to state the units of a parameter. We work in eV, and as can be seen from e.g. equations (3.3) and (3.16), all parameters share this unit.

3.3.1 Input/output scan

In general the self-consistency problem can be quite involved. We are, however, in the privileged situation of only having to determine *one* (although complex) mean-field parameter. We can therefore scan all possible mean-field parameters and wee what output parameter they give rise to. That is to say, we repeat the calculation

$$R_0 \to H_0 \to R_1 = \langle 2V_{pd}\mathcal{A} \rangle_{H_0} \tag{3.49}$$

for many different inputs R_0. Once both real and imaginary part of R_0 and R_1 agree, a stable solution has been found. This is illustrated in Figures 3.3 and 3.4, where we plot the input/output relations in grey. Superimposed is the "input=output" plane in bright red, orange, and yellow. In Figures 3.3 and 3.4 we immediately see that only the trivial choice of R is stable when $V_{pd} = 3$, whereas a non-trivial possible "ring of stability" seem to appear when we increase V_{pd} to 5 in Figure 3.4.

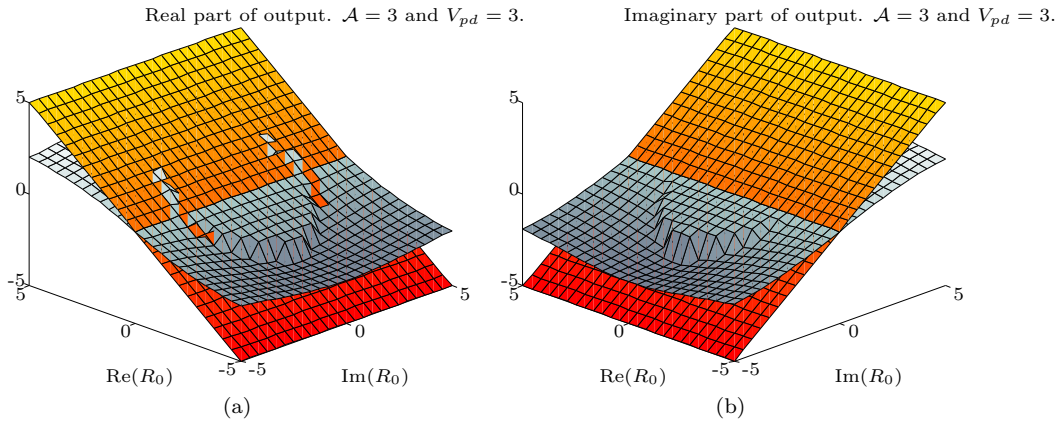

Figure 3.3: We use two three-dimensional figures to display the four-dimensional graph of a complex function of a complex variable. In both 3.3a and 3.3b, the (flat) xy-plane is the complex plane of R_0-values. The z-axis is then the real (in 3.3a) or imaginary (in 3.3a) part of the output. Having $\mathrm{Im}(R_0) = \mathrm{Im}(R_1)$ forces $\mathrm{Im}(R_0)$ to be zero. And then $\mathrm{Re}(R_0)$ must also vanish.

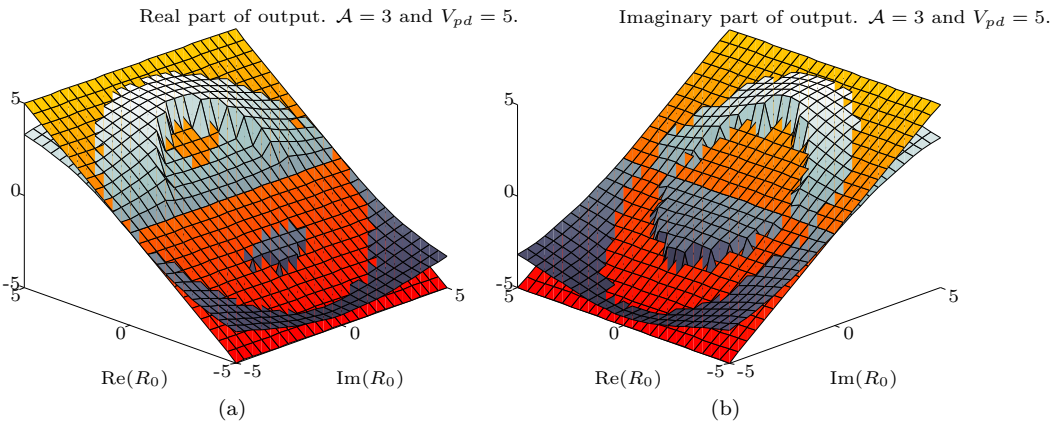

Figure 3.4: Same idea as in Figure 3.3. Now more values of R_0 seem to be stable, i.e., satisfy that $\mathrm{Re}(R_0) = \mathrm{Re}(R_1)$ and $\mathrm{Im}(R_0) = \mathrm{Im}(R_1)$.

3.3.2 Iteration for stability

The behaviour seen in the last section is also apparent when we do the self-consistency calculation in a different way, namely by iterating the above procedure. Our algorithm now does this:

$$R_0 \to H_0 \to \langle 2V_{pd}\mathcal{A}\rangle_{H_0} = R_1 \to H_1 \to \langle 2V_{pd}\mathcal{A}\rangle_{H_1} = R_2 \to \ldots \tag{3.50}$$

As seen from Figures 3.5 and 3.6, such a scheme does not seem to converge when $V_{pd} = 3$, whereas convergence is indeed attained for $V_{pd} = 5$. Of course, these figures do not tell us anything about the dependence of initial guesses nor of the possibilities of other stable solutions. This is exactly where plots like those in Figures 3.3 and 3.4 come in handy. However, it is very hard to get a precise numerical value for the parameter if one does not invoke the iterative procedure.

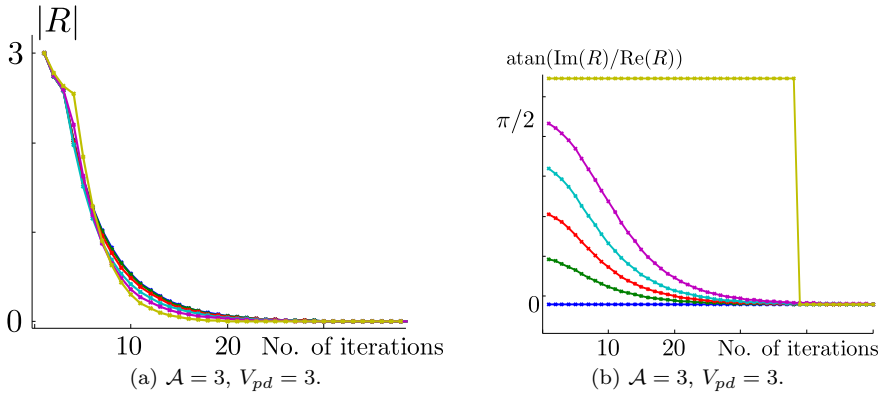

(a) $\mathcal{A} = 3$, $V_{pd} = 3$. (b) $\mathcal{A} = 3$, $V_{pd} = 3$.

Figure 3.5: Iterative evolution of length and phase of R. The colours on the left correspond to the colours on the right, and we thus fix $|R|$ for every initial guess but vary the phase. The trend is clear: everything goes to zero.

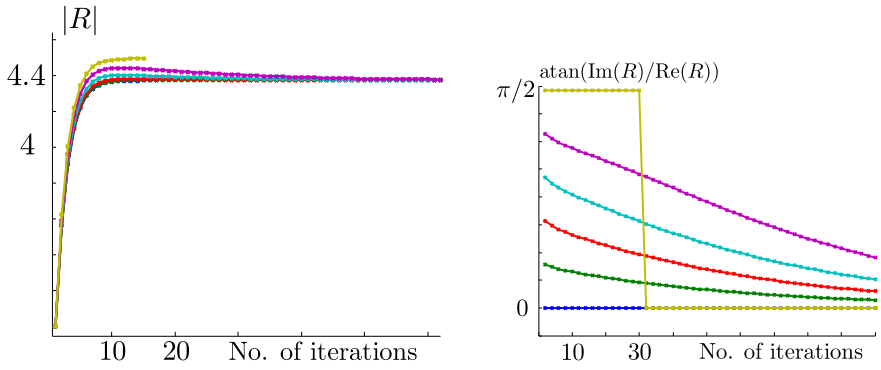

(a) $\mathcal{A} = 3$, $V_{pd} = 5$. (b) $\mathcal{A} = 3$, $V_{pd} = 5$.

Figure 3.6: Same procedure as in Figure 3.5. Now a non-zero solution is stable. But notice a danger of this procedure: it takes forever for the phase to converge to zero.

3.3.3 Energy considerations

Finally, as mentioned in the beginning of this section, one may also demand that the self-consistent parameter be a minimizer of the free energy. This is what we do now. Generally, the free energy, F, of our system is given by

$$F = \langle \mathcal{H} \rangle - TS, \tag{3.51}$$

where S is the entropy of the system and T is the temperature. At zero temperature, we thus only need to find the energy. To this end, we need to contradict what we said below equation (3.10) and actually include the constant term in the definition of $\mathcal{H}$. The reason is of course that when we change R and V_{pd}, this term no longer constant. Once we have settled on a specific V_{pd} and R the term can once more be disregarded without affecting our conscience.

The quantity in question is thus $\langle \mathcal{H} \rangle$, which we calculate as the sum (for all $\mathbf{k} \in FBZ$) of eigenvalues of the 3×3-matrix $H(\mathbf{k})$ that lie below the chemical potential plus the otherwise-to-be-disregarded-term. The explicit form of this term can, by the way, be determined from the minimization demand along with the definition of the mean-field parameter (equation (3.9)). Let us denote the term $f(R, R^*)$. Then

$$\begin{aligned} 0 = \frac{\partial F}{\partial R} &= \frac{\partial}{\partial R} \left\langle \mathcal{H}_0 - R\mathcal{A}^\dagger - R^* \mathcal{A} \right\rangle + \frac{\partial f(R, R^*)}{\partial R}, \\ \Rightarrow \left\langle \mathcal{A}^\dagger \right\rangle &= \frac{\partial f(R, R^*)}{\partial R}, \end{aligned} \tag{3.52}$$

and similarly for the complex conjugate,

$$\langle \mathcal{A} \rangle = \frac{\partial f(R, R^*)}{\partial R^*}, \tag{3.53}$$

which yields equation (3.9) if $f(R, R^*) = |R|^2/(2V_{pd})$, in accordance with equation (3.10).

In Figure 3.7 we see the clear development of the energy from supporting only the trivial solution, to actually having a non-zero mean-field parameter minimizing it.

For completeness, we plot two cuts of the energy surface, one along a real R and the other along an imaginary R. This confirms the actual value of the parameter found above by the iterative procedure, in particular that the parameter is real.

In conclusion we thus see that a circulating current phase is possible to stabilize. Although we shall later depart from the self-consistent regime and enter the world of phenomenology, it is a promising feature of the loop currents that self-consistent parameter choices actually exist.

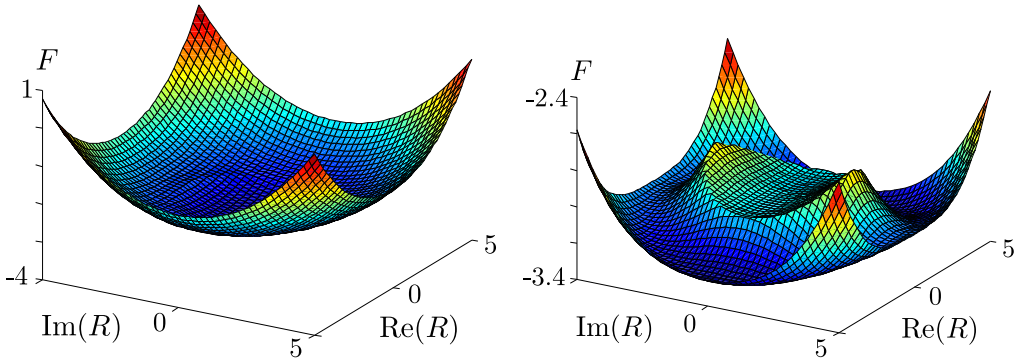

(a) $\mathcal{A} = 3$, $V_{pd} = 3$. (b) $\mathcal{A} = 3$, $V_{pd} = 5$.

Figure 3.7: For $V_{pd} = 3$ $R = 0$ is a distinct global minimum, whereas $R \neq 0$ minimizes the energy for $V_{pd} = 5$. Note the asymmetry between $\mathrm{Re}(R)$ and $\mathrm{Im}(R)$.

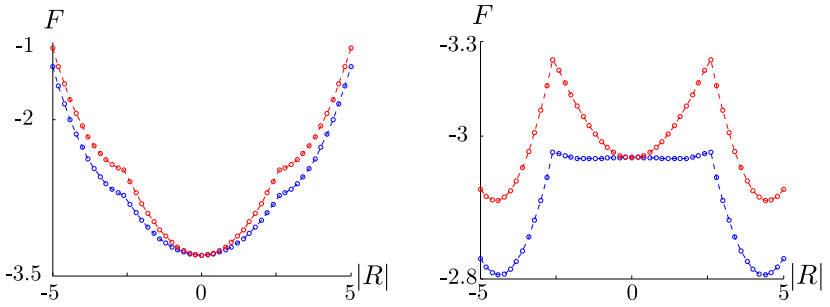

(a) $\mathcal{A} = 3$, $V_{pd} = 3$. (b) $\mathcal{A} = 3$, $V_{pd} = 5$.

Figure 3.8: Cuts through the surfaces of Figure 3.7. Red: Imaginary R. Blue: Real R.

3.4 Physical properties of the circulating current state

Self-consistency is one thing, good as a sanity check, but another thing as actual physical properties. Be it stable or not, the presence of a circulating current order parameter have better change some measurable features of our system, or we might as well never mention it. Luckily, there are at least two predictions to be obtained from assuming one of the Hamiltonians in (3.16) to (3.19).

3.4.1 Actual current patterns

Even though the inter-orbital currents themselves are not directly assessable to the STM, the patterns they form reveal something the about the (broken) symmetries of the system. As is apparent from Figure 3.1, a change of the orbital convention can correspond to a $\pi/2$ rotation of the coordinate system. We stick to our "$+-+$" convention[5] and then obtain the current patterns shown below in Figures 3.9, 3.10, and 3.11. In all three, the length of R is kept fixed at 4, and we scan the phase of R. This is in order to investigate how the current parameter phase affects the current pattern. It was found that scaling the R parameter only had a trivial effect on the magnitude of the resulting current patters. This is a good validation of our model, we actually achieve the current patterns when doing mean-field theory. We also note with pleasure that the total current through each orbital is zero.

[5]We maintain this convention throughout the thesis.

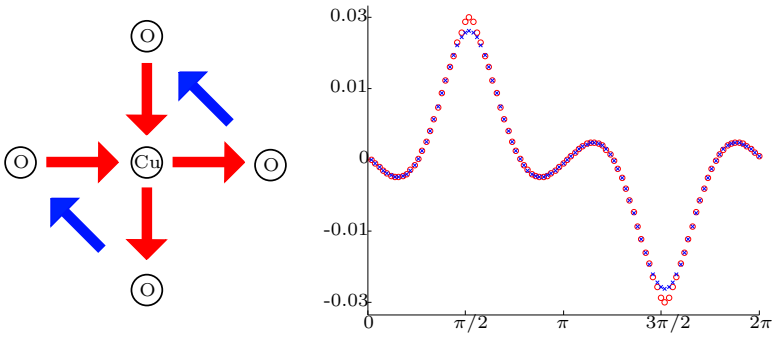

Figure 3.9: The current pattern for $\mathcal{A} = 1$. The colours on the left correspond to the colours on the right. The graph to the right shows the bare number for the current as given in e.g. equation 3.31 versus the phase of R.

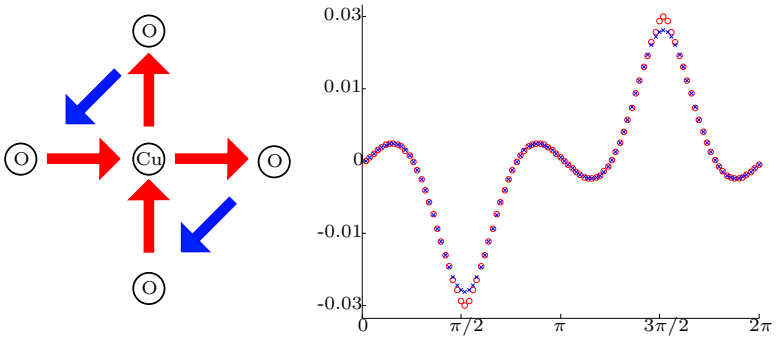

Figure 3.10: The current pattern for $\mathcal{A} = 2$. The colours on the left correspond to the colours on the right. Very similar to the $\mathcal{A} = 1$ case. We might note that the current values at the R-phase $\pm\pi/2$ are not completely identical. For these calculations it has been meticulously checked that the blue and red current strengths converge to the same number as the **k**-space resolution is increased. These plots are for a 200×200 **k**-space, and have converged almost everywhere.

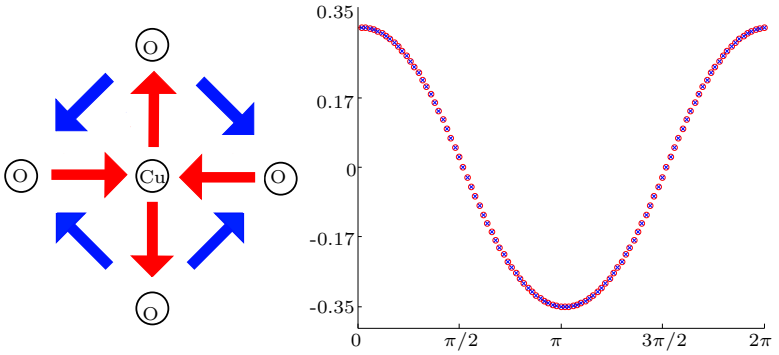

Figure 3.11: The current pattern for $\mathcal{A} = 3$. Now a somewhat different current pattern. Plotted to the right is the strength of a red current and *twice* the strength of a blue one, corresponding to zero net current through each orbital.

For $\mathcal{A} = 4$, no non-vanishing current values could be obtained. This concludes our patience with this particular decoupling, and we shall for the remainder of this thesis only consider the three other cases. They will in return reveal sufficient information to us, that no real loss will be felt.

For the $\mathcal{A} = 3$ case, one may easily compare e.g. Figures 3.8 and 3.11 and see how the self-consistent parameter also corresponds to the largest current expectation value. For the $\mathcal{A} = 1, 2$ cases, this was unfortunately not the case. This will mark our departure from self-consistency, as we in the next two chapters shall use the parameter choices yielding the maximal current strengths.

We can read off certain spatial symmetries from the pictures of the current patterns. For instance, the $\mathcal{A} = 1$ pattern is invariant under a reflection in the $x = -y$ line, whereas the corresponding symmetry line for $\mathcal{A} = 2$ is $x = y$, and no such line exists for $\mathcal{A} = 3$. If we disregard the direction of the currents, the $\mathcal{A} = 3$ pattern is seen to be symmetric under a C4-rotation, and reflections in the axes as well as the $x = \pm y$ lines, whereas the $\mathcal{A} = 1, 2$ patterns still break axial reflection symmetries and C4. These symmetries will show up again in the next chapter, and be thoroughly discussed in chapter 5.

3.4.2 Density of states; a gap anywhere?

It is interesting to see how the bulk density of states changes as the loop-current order parameter increases. It is an obvious question to ask, whether the mean-field version of Varma's theory actually predicts a (pseudo) gap in the density of states. We shall in the following consider two different cases, namely having $\epsilon_d = \epsilon_p = 0$ and having $\epsilon_d = -1.5$ eV and $\epsilon_p = -5$ eV.

We now gradually increase the current parameter for the $\mathcal{A} = 1$ and $\mathcal{A} = 3$ cases[6] to see how the bulk density of states is affected by this.

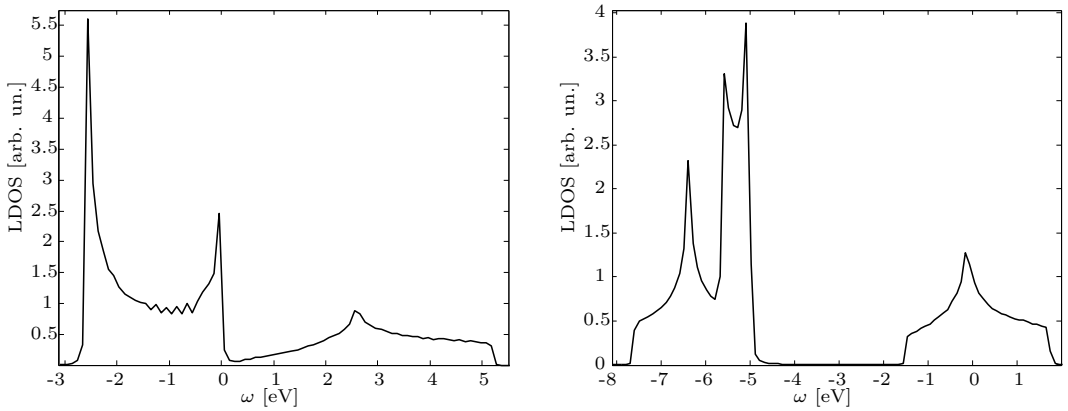

(a) The bulk DOS for $\epsilon_d = \epsilon_p = 0$.

(b) The bulk DOS for $\epsilon_d = -1.5$ eV and $\epsilon_p = -5$ eV.

Figure 3.12: The DOS for two parameter choices.

Shown in Figure 3.12 is the bulk density of states for zero currents for the two parameter choices mentioned above. The actual forms of the curves are not that important, as only a small energy range is experimentally accessible without any interference from other layers in the cuprate, i.e., we do not expect our theory to predict the STM-measured form of these curves with any precision. What we *are* looking for is a qualitative signature of what happens upon increasing the current parameters.

[6]The $\mathcal{A} = 2$ case is just a rotation of the $\mathcal{A} = 1$ case. The DOS should not be able to see this, and the calculated DOS plots for $\mathcal{A} = 2$ are indeed identical to those for $\mathcal{A} = 1$.

Shown in Figure 3.13 is the DOS evolution as R is increased from 0 to $3i$ (in equal steps increasing upwards in the Figure). We see a smearing of the DOS, but no distinct gap features.

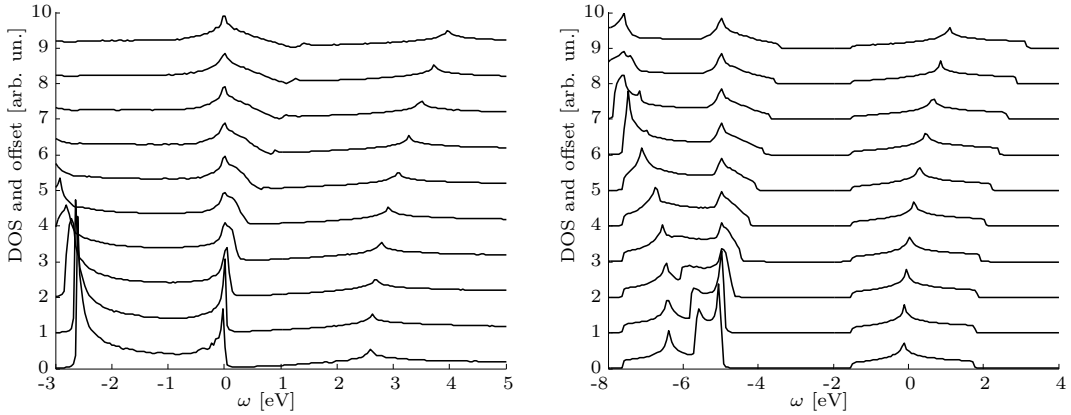

(a) $\mathcal{A} = 1$ (b) $\mathcal{A} = 1$

Figure 3.13: The evolution of the bulk DOS as R is increased in equal steps from 0 to $3i$. Each curve is for an R-value $\frac{3i}{10}$ higher than the curve beneath it and is set off with 1 in our arbitrary DOS-units with respect to the curve beneath it.

In Figure 3.14 we see how the bulk density of states changes as R is being cranked up from 0 to 3. This time the DOS seems to get squeezed together as well as smeared out. No gap seems to manifest itself.

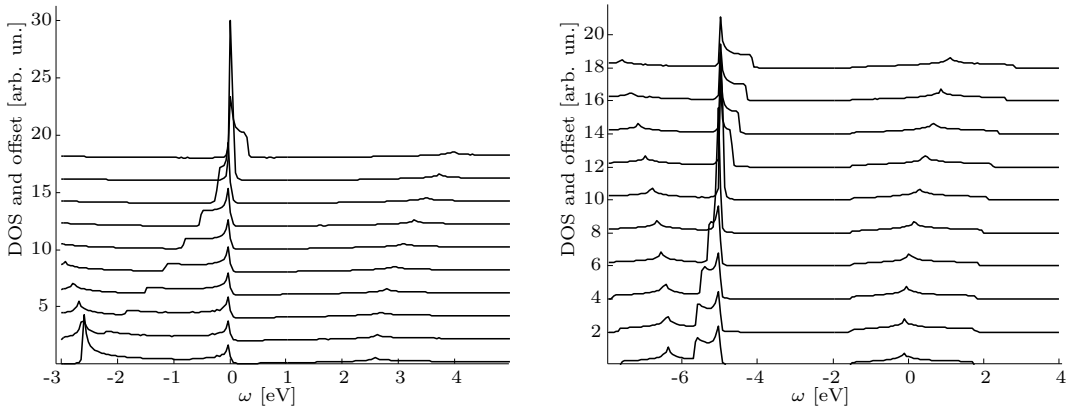

(a) $\mathcal{A} = 3$ (b) $\mathcal{A} = 3$

Figure 3.14: The evolution of the bulk DOS as R is increased in equal steps from 0 to 3. Each curve is for an R-value $\frac{3}{10}$ higher than the curve beneath it and is set off with 2 in our arbitrary units with respect to the curve beneath it.

On the basis of the Figures 3.13 and 3.14 no convincing conclusions can be drawn, or, to quote chapter 1, no smoking gun is to be seen. We thus end this chapter by concluding that a loop current fingerprint should rather be found from the spatial symmetries of the loop patterns. The appearance of non-vanishing currents but lack of a gap feature in mean-field is in accordance with Varma's own predictions in [12]. Here it is found that the emergence of a gap requires the inclusion of fluctuations of the current parameter to be taken into account. We do not venture that far with the loop current theory, but stay within the mean-field picture and look for the spatial symmetries of the current patterns to show up in the local density of

states. But if we are to see spatial symmetry breaking, a homogeneous system is not a good system to consider, and we therefore break the translation invariance of our model in the next chapter, by introducing an impurity.

3.5 Summary

In summary, we have now investigated the mean-field loop current theory to an extent where we feel confident enough to use it in actual predictions. We found the emergence of intra-orbital currents along with explicit current conservation. Furthermore, we found no homogeneous fingerprints of the loop-currents, apart from the breaking of certain symmetries by the current patterns. These broken spatial symmetries will form the basis of our results, as presented in the next chapter and analysed in the chapter after that.

Chapter 4

Impurity scattering, the local density of states

We now arrive at the heart of this thesis. With a thorough understanding of the behaviour of Varma's mean-field theory at hand (chapter 3), we turn to the LDOS around an impurity to search for a loop-current fingerprint.

4.1 Introducing the impurity

In the cuprates, impurities are not a nuisance or something unfortunate a very careful experimentalist could have avoided. On the contrary, they are put into the material on purpose (by a very careful experimentalist) and are the cause of the doping as they "suck out" electrons or holes of the CuO_2 layers. It is therefore highly realistic and relevant to include impurities into our model.

For our purposes, a single impurity will suffice. Introducing more of them will only complicate things, and we want to study the LDOS modulations in the immediate vicinity of an impurity, where any other deviations from the CuO_2 lattice can safely be ignored. This of course implies that our results should be considered valid in the dilute limit of low impurity concentration. This is in fine agreement with being in the lower-doping part of the phase diagram (see Figure 1.2a). We model this single impurity as depicted graphically in Figure 4.1 and mathematically in equation (4.1); by adding an extra energy to the creation/annihilation operator pair on one specific copper orbital. The spin dependence in equation (4.1) stems from the possibility of having a magnetic impurity, which still resides only one particular place in space, buts treats spin up and spin down differently.

$$\mathcal{H} \to \mathcal{H} + \sum_{\sigma} V_{\sigma}^{\text{imp}} d_{\sigma \mathbf{r}_0}^{\dagger} d_{\sigma \mathbf{r}_0} = \mathcal{H} + \sum_{\mathbf{r},\sigma} V_{\sigma}^{\text{imp}} d_{\sigma \mathbf{r}}^{\dagger} d_{\sigma \mathbf{r}} \delta(\mathbf{r} - \mathbf{r}_0) \tag{4.1}$$

The only difference between a magnetic and non-magnetic impurity will be that $V_{\uparrow}^{\text{imp}} = V_{\downarrow}^{\text{imp}}$ for a non-magnetic impurity and $V_{\uparrow}^{\text{imp}} = -V_{\downarrow}^{\text{imp}}$ for a magnetic one. In our actual calculations we only consider a non-magnetic impurity.

It is important to note that this sort of impurity model still leaves our full Hamiltonian quadratic in creation/annihilation operators. We use this fact in the very beginning of the next section, more precisely in equation (4.3).

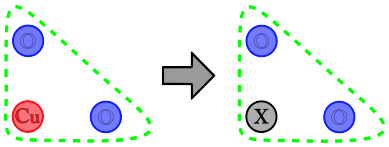

Figure 4.1: One copper atom gets modified by an enlargened on-site potential.

4.2 General case derivation

As the LDOS is our ultimate goal, we need a spectral function and to that end a Green's function. We largely follow [4, Chapter 4], whence the following very nice derivation for the case of a single impurity stems.

Let us first denote the full Hamiltonian as $\mathcal{H}$ where $\mathcal{H} = \mathcal{H}^0 + \mathcal{H}^{\text{imp}}$, and furthermore $\mathcal{H} = \psi^\dagger H \psi = \psi^\dagger (H^0 + H^{\text{imp}})\psi$. For the Green's function of respectively thee free and full Hamiltonian we have that

$$[1(\omega + i\eta) - H^0]G^0(\omega) = 1 \tag{4.2}$$

and

$$[1(\omega + i\eta) - H]G(\omega) = 1, \tag{4.3}$$

where 1 is the identity operator and a matrix structure of the Green's functions is understood. Equating the left hand sides of equations (4.2) and (4.3) then yields that

$$\begin{aligned}[1(\omega + i\eta) - H]G(\omega) &= [1(\omega + i\eta) - H + H^{\text{imp}}]G^0(\omega) &(4.4)\\ &= [1(\omega + i\eta) - H]G^0(\omega) + H^{\text{imp}}G^0(\omega). &(4.5)\end{aligned}$$

Since, by equation (4.3), $G(\omega) = [1(\omega + i\eta) - H]^{-1}$, we can multiply by $G(\omega)$ from the left and obtain the Dyson integral equation;

$$G(\omega) = G^0(\omega) + G(\omega)H^{\text{imp}}G^0(\omega). \tag{4.6}$$

In a basis where H^{imp} is (block) diagonal, this equation takes the following appealingly simple component-wise form:

$$G_{\mu\nu}(\omega) = G^0_{\mu\nu}(\omega) + \sum_{\nu'} G_{\mu\nu'}(\omega)H^{\text{imp}}_{\nu'}G^0_{\nu'\nu}(\omega). \tag{4.7}$$

For our impurity, the position basis is just such a basis, since H^{imp} is proportional to a δ-function (see equation (4.1)). If we understand orbital and spin matrix structure of the factors, we then have that

$$G(\mathbf{r}, \mathbf{r}', \omega) = G^0(\mathbf{r} - \mathbf{r}', \omega) + G(\mathbf{r}, \mathbf{r}_0, \omega)H^{\text{imp}}(\mathbf{r}_0)G^0(\mathbf{r}_0 - \mathbf{r}', \omega), \tag{4.8}$$

from where it immediately follows that

$$G(\mathbf{r}, \mathbf{r}_0, \omega) = G^0(\mathbf{r} - \mathbf{r}_0, \omega) + G(\mathbf{r}, \mathbf{r}_0, \omega)H^{\text{imp}}(\mathbf{r}_0)G^0(\mathbf{r}_0 - \mathbf{r}_0, \omega), \tag{4.9}$$

and hence that

$$G(\mathbf{r}, \mathbf{r}_0, \omega) = G^0(\mathbf{r} - \mathbf{r}_0, \omega)[1 - H^{\text{imp}}(\mathbf{r}_0)G^0(\mathbf{r}_0 - \mathbf{r}_0, \omega)]^{-1}. \tag{4.10}$$

The *exact* solution to the real-space Dyson equation (equation 4.8) is thus

$$\begin{aligned}G(\mathbf{r}, \mathbf{r}', \omega) &= G^0(\mathbf{r} - \mathbf{r}', \omega)\\ &\quad + G^0(\mathbf{r} - \mathbf{r}_0, \omega)[1 - H^{\text{imp}}(\mathbf{r}_0)G^0(\mathbf{r}_0 - \mathbf{r}_0, \omega)]^{-1}H^{\text{imp}}(\mathbf{r}_0)G^0(\mathbf{r}_0 - \mathbf{r}', \omega), &(4.11)\end{aligned}$$

which has the very nice feature of only involving *free* Green's functions. We can rewrite this expression for the full Green's function in a slightly more illustrative way.

From [23, Chapter 5] we have the following expression for the T-matrix:

$$T = H^{\text{imp}} + H^{\text{imp}} \underbrace{\frac{1}{\omega + i\eta - H_0}}_{G^0} T, \tag{4.12}$$

which can be rearranged as

$$T = [1 - H^{\text{imp}} G^0]^{-1} H^{\text{imp}}. \tag{4.13}$$

The compact form of equation (4.11) is thus

$$G(\mathbf{r}, \mathbf{r}', \omega) = G^0(\mathbf{r} - \mathbf{r}', \omega) + G^0(\mathbf{r} - \mathbf{r}_0, \omega) T(\mathbf{r}_0, \omega) G^0(\mathbf{r}_0 - \mathbf{r}', \omega), \tag{4.14}$$

which is intuitively reasonable, as illustrated in Figure 4.2.

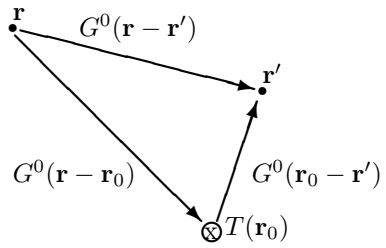

Figure 4.2: How does the particle get from $\mathbf{r}$ to $\mathbf{r}'$? -By either propagating freely or by scattering off the impurity. The arrows represent unperturbed propagators, i.e., free Green's functions.

Note that the T or scattering matrix - since it contains a Green's function - can be advanced or retarded. As is the case with Green's functions, we take it to be retarded if nothing else is mentioned. It is also worth noting that the T matrix for a single impurity is a function of energy only. This is not really apparent from the notation of equation (4.14), but follows from the translation invariance of the unperturbed system;

$$T(\mathbf{r}_0, \omega) = [1 - H^{\text{imp}} G^0(\mathbf{r}_0 - \mathbf{r}_0, \omega)]^{-1} H^{\text{imp}} = [1 - H^{\text{imp}} G^0(0, \omega)]^{-1} H^{\text{imp}} \equiv T(\omega). \tag{4.15}$$

Regardless of where we (spatially) want to calculate the LDOS, we thus only need to calculate the T matrix once.

4.3 Three band case

We now mimic section 2.2 and demonstrate how we get from a general expression to a numerical value; an actual result for the LDOS around an impurity.

The first thing to consider is the form of the impurity matrix for a non-magnetic impurity. In the usual (spin degenerate) three-band basis, where $\psi^\dagger(\mathbf{r}) = (d^\dagger_{\mathbf{r}}, p^\dagger_{x,\mathbf{r}}, p^\dagger_{y,\mathbf{r}})$, the impurity matrix only has one non-zero entry;

$$H^{\text{imp}} = \begin{bmatrix} V & 0 & 0 \\ 0 & 0 & 0 \\ 0 & 0 & 0 \end{bmatrix} \delta(\mathbf{r}_0). \tag{4.16}$$

For a given ω, the next step is then to find the free Green's function matrix at the origin. As explained in chapter 2, this is given by

$$G^0(\omega, 0) = \sum_{\mathbf{k}} [1(\omega + i\eta) - H_{3\times 3}(\mathbf{k})]^{-1} . * F_{iuc}(\mathbf{k}), \tag{4.17}$$

where $.*$ denotes elementwise matrix multiplication and

$$F_{3\times 3}(\mathbf{k}) = \begin{bmatrix} 1 & \mathrm{e}^{-ik_x/2} & \mathrm{e}^{-ik_y/2} \\ \mathrm{e}^{ik_x/2} & 1 & \mathrm{e}^{i(k_x-k_y)/2} \\ \mathrm{e}^{ik_y/2} & \mathrm{e}^{i(k_y-k_x)/2} & 1 \end{bmatrix}. \tag{4.18}$$

This gives us the T matrix of ω. Finally, as we shall only ever ask for the full Green's function at the same site, we find the free Green's functions at the sites $\pm\mathbf{r}$;

$$G^0(\pm\mathbf{r}, \omega) = \sum_{\mathbf{k}} [1(\omega + i\eta) - H_{3\times 3}(\mathbf{k})]^{-1} . * F_{iuc}(\mathbf{k}) \mathrm{e}^{\pm i\mathbf{k}\cdot\mathbf{r}}, \tag{4.19}$$

and then perform the matrix multiplication, take the imaginary part, multiply by the appropriate factor, and repeat for another $\mathbf{r}$ or ω. Just as in the bulk case described in chapter 2, our calculation scales linearly with the size of the system as it amounts to repeating the same computation for every point in $\mathbf{k}$-space and then summing up these results.

4.3.1 Nambu-fied three band case

In the superconducting three-band model, the first thing to consider is the spin-dependence of the impurity. We use the same operator basis as described in chapter 2, the three-band Nambu basis given (in $\mathbf{k}$-space) by

$$\psi^\dagger(\mathbf{k}) = (d^\dagger_{\uparrow\mathbf{k}}, p^\dagger_{x,\uparrow\mathbf{k}}, p^\dagger_{y,\uparrow\mathbf{k}}, d_{\downarrow-\mathbf{k}}, p_{x,\downarrow-\mathbf{k}}, p_{y,\downarrow-\mathbf{k}}), \tag{4.20}$$

and take the impurity to be non-magnetic, i.e., it treats spin up and spin down on equal footing. At the impurity site, the impurity matrix can then be written as

$$H^{\mathrm{imp}} = \begin{bmatrix} V & 0 & 0 \\ 0 & 0 & 0 \\ 0 & 0 & 0 \end{bmatrix} \oplus \begin{bmatrix} -V & 0 & 0 \\ 0 & 0 & 0 \\ 0 & 0 & 0 \end{bmatrix}, \tag{4.21}$$

where the minus arises from the reversed order of spin down operators in our basis. The second thing to consider is how we should Fourier transform the entries of the now 6 by 6 Green's function matrix. If we simply perceive each entry in the matrix as an expectation value of two operators (which indeed is what a Green's function is, see [23, chapters 8, 9, and 11]), we see that the operator pairs in question are

$$\left(\begin{array}{ccc|ccc} d_{\uparrow\mathbf{k}}d^\dagger_{\uparrow\mathbf{k}} & d_{\uparrow\mathbf{k}}p^\dagger_{x,\uparrow\mathbf{k}} & d_{\uparrow\mathbf{k}}p^\dagger_{y,\uparrow\mathbf{k}} & d_{\uparrow\mathbf{k}}d_{\downarrow-\mathbf{k}} & d_{\uparrow\mathbf{k}}p_{x,\downarrow-\mathbf{k}} & d_{\uparrow\mathbf{k}}p_{y,\downarrow-\mathbf{k}} \\ p_{x,\uparrow\mathbf{k}}d^\dagger_{\uparrow\mathbf{k}} & p_{x,\uparrow\mathbf{k}}p^\dagger_{x,\uparrow\mathbf{k}} & p_{x,\uparrow\mathbf{k}}p^\dagger_{y,\uparrow\mathbf{k}} & p_{x,\uparrow\mathbf{k}}d_{\downarrow-\mathbf{k}} & p_{x,\uparrow\mathbf{k}}p_{x,\downarrow-\mathbf{k}} & p_{x,\uparrow\mathbf{k}}p_{y,\downarrow-\mathbf{k}} \\ p_{y,\uparrow\mathbf{k}}d^\dagger_{\uparrow\mathbf{k}} & p_{y,\uparrow\mathbf{k}}p^\dagger_{x,\uparrow\mathbf{k}} & p_{y,\uparrow\mathbf{k}}p^\dagger_{y,\uparrow\mathbf{k}} & p_{y,\uparrow\mathbf{k}}d_{\downarrow-\mathbf{k}} & p_{y,\uparrow\mathbf{k}}p_{x,\downarrow-\mathbf{k}} & p_{y,\uparrow\mathbf{k}}p_{y,\downarrow-\mathbf{k}} \\ \hline d^\dagger_{\downarrow-\mathbf{k}}d^\dagger_{\uparrow\mathbf{k}} & d^\dagger_{\downarrow-\mathbf{k}}p^\dagger_{x,\uparrow\mathbf{k}} & d^\dagger_{\downarrow-\mathbf{k}}p^\dagger_{y,\uparrow\mathbf{k}} & d^\dagger_{\downarrow-\mathbf{k}}d_{\downarrow-\mathbf{k}} & d^\dagger_{\downarrow-\mathbf{k}}p_{x,\downarrow-\mathbf{k}} & d^\dagger_{\downarrow-\mathbf{k}}p_{y,\downarrow-\mathbf{k}} \\ p^\dagger_{x,\downarrow-\mathbf{k}}d^\dagger_{\uparrow\mathbf{k}} & p^\dagger_{x,\downarrow-\mathbf{k}}p^\dagger_{x,\uparrow\mathbf{k}} & p^\dagger_{x,\downarrow-\mathbf{k}}p^\dagger_{y,\uparrow\mathbf{k}} & p^\dagger_{x,\downarrow-\mathbf{k}}d_{\downarrow-\mathbf{k}} & p^\dagger_{x,\downarrow-\mathbf{k}}p_{x,\downarrow-\mathbf{k}} & p^\dagger_{x,\downarrow-\mathbf{k}}p_{y,\downarrow-\mathbf{k}} \\ p^\dagger_{y,\downarrow-\mathbf{k}}d^\dagger_{\uparrow\mathbf{k}} & p^\dagger_{y,\downarrow-\mathbf{k}}p^\dagger_{x,\uparrow\mathbf{k}} & p^\dagger_{y,\downarrow-\mathbf{k}}p^\dagger_{y,\uparrow\mathbf{k}} & p^\dagger_{y,\downarrow-\mathbf{k}}d_{\downarrow-\mathbf{k}} & p^\dagger_{y,\downarrow-\mathbf{k}}p_{x,\downarrow-\mathbf{k}} & p^\dagger_{y,\downarrow-\mathbf{k}}p_{y,\downarrow-\mathbf{k}} \end{array}\right).$$

By invoking our usual Fourier transform of each operator (equation (3.11)), we thus find that each 3 by 3 block will have the same intra unit cell Fourier phase matrix, namely the one given in equation (4.18).

It is indeed this Nambu-fied model we shall use in the remainder of the chapter, possibly with some parameters set to zero. The Hamiltonian is thus the one of equations (2.45) and (2.46), with the 3-band Hamiltonian given by one of the equations (3.16) to (3.18).

4.4 Results of the calculation

We now present the first series of our main results, which are local density of states plots for different relevant cases. In particular, we repeat our calculations for the two sets of hybridization energies mentioned in the previous chapter, namely $\epsilon_d = \epsilon_p = 0$ and $\epsilon_d = -1.5$ eV and $\epsilon_p = -5$ eV, to find the dependence of our results on the specific parameter choices. It is of course always a trade-off when one performs numerical calculations, that one on one hand would like to verify that the behaviour seen is not an artefact of the particular parameter choice invoked, but on the other hand does not want to perform an exhaustive search in the parameter space[1]. We choose this procedure as a sound compromise between generality and clarity.

So which parameters do we use? First of all, we restrict ourselves in this chapter to consider only the $\mathcal{A} = 1$ current pattern. This pattern will provide us with the results we shall perceive as the main findings of our study. In the next chapter, where we present a more in-depth analysis of our results, we shall also discuss the differences to the other current patterns. The main conclusion hereof will be that the LDOS is sensitive to where the currents run - to be understood as between which orbitals there is a non-vanishing current expectation value (c.f. Figures 3.9 to 3.11) - but insensitive to the direction of the currents. It should in this respect be mentioned that the phase-dependence of the current values was found to be very similar for both sets of hybridization energies, in particular that the current-maximising phases are the same for both cases. See Appendix A for details.

Secondly, as we do not have self-consistent values for the co-existing superconducting gap and current parameter at hand, we choose these large enough to see distinct effects of their presence, but small enough to (hopefully) avoid any pathological results. In section 4.5, we use as a good compromise the values $\Delta_0 = 0.25$, $R = 1i$. Our choice for the complex phase of R draws upon our analysis of Varma's mean-field theory by itself; it is the phase that was found to maximize the current expectation value (see Figure 3.9).

As a final thing before presenting the results, let us clarify how we perceive the lattice. When we calculate the local density of states, we of course have to specify a lattice point in which we calculate it. We count lattice points as unit cells, and then choose the appropriate orbital (Green's function entry) for the inner structure. This is illustrated in Figure 4.3.

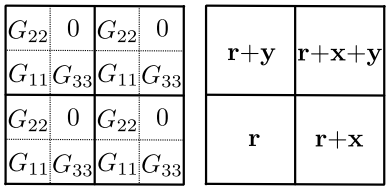

Figure 4.3: We perceive the lattice as a cubic square lattice (right), where each point has an inner spatial structure (left).

This spatial structure is also very important to keep in mind, when we discuss spatial symmetries. The origin of our coordinate system (with respect to the impurity) is placed inside - but *not* in the middle of - the unit cell at $\mathbf{r} = (0, 0)$. This can potentially cause some confusion, which we shall do our best to illustrate our way out of, whenever the need arises.

4.5 The realistic parameters

We start out by setting $\epsilon_d = -1.5$ eV and $\epsilon_p = -5$ eV. We shall focus on a small energy range close to the fermi energy, as this is the experimentally relevant region.

[1] For our full theory, we provide the numerical inputs: ϵ_d, ϵ_p, t_{pd}, t_{pp}, Δ_0, R, V_{imp}, and $\mathcal{A}$. We only really want to vary R and switch between two or three values for $\mathcal{A}$ and Δ_0.

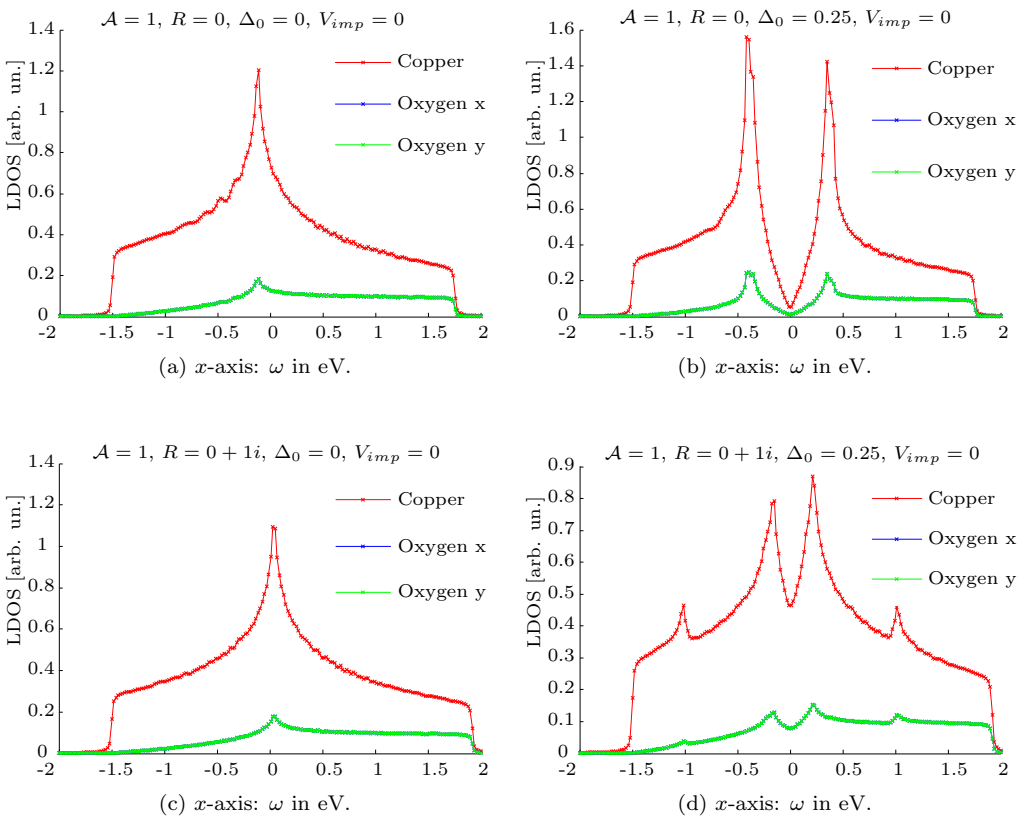

(a) x-axis: ω in eV. (b) x-axis: ω in eV.

(c) x-axis: ω in eV. (d) x-axis: ω in eV.

Figure 4.4: Reference plots in the relevant energy range (extended a bit). The parameters used in the computation are shown above each plot. The legend shows three curves, but only two are to be seen in the plots. This is due to the two oxygen density of states being equal in the homogeneous case. Note the two extra peaks at $\omega \approx \pm 1$ eV.

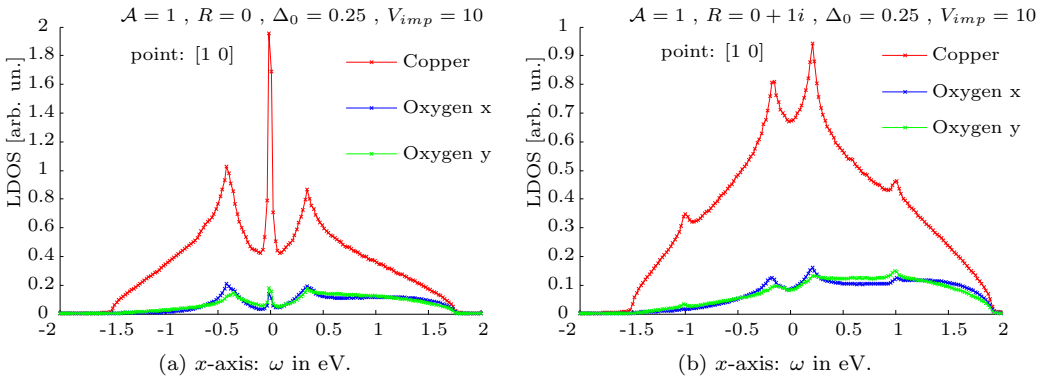

(a) x-axis: ω in eV. (b) x-axis: ω in eV.

Figure 4.5: The characteristic nearest-neighbour sub-gap peak disappears in the presence of a current. The extra peaks noted also in Figure 4.4d remain.

As a first thing, as a reference, let us see how the orbitally resolved homogeneous density of states with and without superconductivity and orbital currents looks. This is shown in Figures 4.4a to 4.4d. These four plots reveal some qualitative information about our model to us. First of all, we see that the introduction of a current does not alter the non-superconducting DOS in any significant way (compare Figures 4.4a and 4.4c), which is of course in accordance with what we saw in Figure 3.13b. As a second thing, we observe that although we only placed superconductivity on the copper atoms, the oxygen atoms resonate along, and form coherence peaks at the same energies as the copper does. This feature is present in all of our numerical data, whenever superconductivity can be identified. Recalling the discussion of chapter 2 on how to put superconductivity into the model, it is noted that majority of the spectral weight at and near the Fermi level of the system actually resides on copper in the normal state, so our choice of letting all the Cooper pairs condense on copper might all in all not have been too crude.

Furthermore, we notice the possible co-existence of superconductivity and currents in the model. Although the superconducting gap gets reduced from Figure 4.4b to Figure 4.4d, in the sense that the DOS at $\omega = 0$ no longer vanishes, it is still present and the characteristic "V-neck" gap is evident also in Figure 4.4d. Also, some new peaks are present. We return to these later in this section. This surviving gap behaviour is lost when R becomes too large, which is our main reason for keeping R and Δ_0 of the same magnitude. The co-existence of d-wave superconducting fingerprints and loop-currents is not a surprising result in itself, since we explicitly assumed the coexistence in the way we built our model, but it is nonetheless an indication of the model behaving in a way we understand.

On the other hand, though, some of the usual and well-understood features of a d-wave superconductor seem to be completely lost in the presence of currents. In a one-band superconductor with a single impurity, one finds huge sub-gap peaks in the LDOS on the nearest neighbours away from the impurity (see [4, chapter 3] for a discussion of this). This feature clearly survives into the current-less three-band model, in the sense that the peak is on the nearest-neighbouring copper atom, as shown in Figure 4.5a, but is nowhere to be seen in Figure 4.5b.

Now, as mentioned in chapter 2, is it not our aim to study the co-existence of superconductivity and currents in great detail. We do phenomenology; put in the superconductivity by hand and look for a current signature. It would thus be somewhat hollow to find this signature in the specific way the currents alter the usual superconductivity features. Instead, we look somewhere else for our smoking gun, and find it in the spatial modulations around the impurity.

In Figure 4.6, the smoke is evident. We fix the energy at the peak value of Figure 4.5a and vary the position at which the LDOS is calculated. We can easily cover a very large plaquette this way by virtue of equation (4.14), but as the LDOS modulations fall off quite rapidly as ones moves away from the impurity, we zoom in near the impurity to get a good look of what is going on. The real system size is of course determined by our $\mathbf{k}$-space resolution, which for the plots in Figure 4.6 is 200×200.

A real-space plot is a very nice visualization of things, and provides us with an overview of what is going on. But as the mind has no standard way of ordering colours (see [31] for a discussion of this), a lot of quantitative information is absent. We clearly see that the C4 symmetry is broken in Figure 4.6b, but by what measure? And more importantly: what is the R dependence of the breaking? We quantify the breaking in the following way. We look at the two unit cells at respectively $x = -1$, $y = 1$ and $x = -1$, $y = -1$. Let us denote the former site as $\mathbf{r}$ and the latter as $\mathbf{r}'$. As the reader may easily verify (or deduct from Figure 5.1b), a C4 invariance implies that

$$\rho_d(\mathbf{r}, \omega) = \rho_d(\mathbf{r}', \omega) \quad \text{and} \quad \rho_{p_x}(\mathbf{r}, \omega) = \rho_{p_y}(\mathbf{r}', \omega). \tag{4.22}$$

In a suitable range of ω, we now calculate the three orbital densities of states at these two sites, while we gradually increase R. We then quantify the C4 breaking, denote it $B_d(R)$

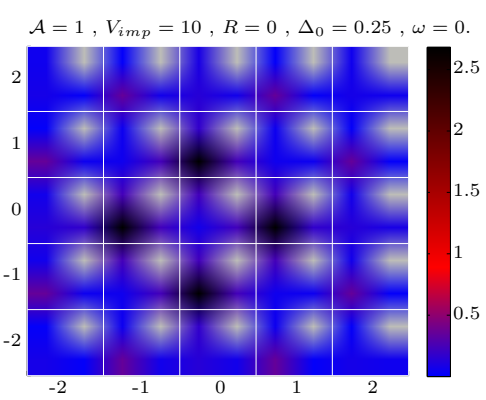

(a) Superconducting state with no currents.

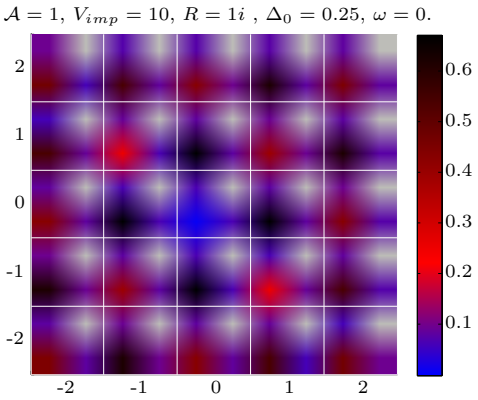

(b) Superconducting state with currents. C4 is broken.

Figure 4.6: Real-space grid with the density of states at the energy shown above the plot. The x- and y-axes are labelled in accordance with Figure 4.3. The colour scale shown to the right of each plot is in the same arbitrary units as the previous plots of this section. The grey colour represents nothing; no atom resides in this location, and we thus do not calculate a value for the grey squares; their value is taken to be zero. The impurity resides in the copper (South-West) corner of the [0 0] cell in each plot.

and $B_p(R)$, respectively, for each ω and R-value as the absolute value of the LDOS difference divided by the average LDOS value. In formulas,

$$B_d(R,\omega) = \frac{2|\rho_d(\mathbf{r},\omega) - \rho_d(\mathbf{r}',\omega)|}{|\rho_d(\mathbf{r},\omega) + \rho_d(\mathbf{r}',\omega)|}, \tag{4.23}$$

and

$$B_p(R,\omega) = \frac{2|\rho_{p_x}(\mathbf{r},\omega) - \rho_{p_y}(\mathbf{r}',\omega)|}{|\rho_{p_x}(\mathbf{r},\omega) + \rho_{p_y}(\mathbf{r}',\omega)|}. \tag{4.24}$$

We measure the $B_i(R,\omega)$ in percent. The result of this calculation is shown in Figure 4.7. Interestingly, the difference between the calculated densities of states is identically zero[2] when $R = 0$, but have relatively large finite values for all the non-zero R-values. The conclusion from the numerical point of view is thus that this effect is solely ascribable to the R-parameter. In the next chapter, we verify analytically that no C4 breaking is possible in the normal state without the currents. The energy dependence of the symmetry breaking also deserves mentioning. First of all, we note the connection between the peaks in the $B_d(R,\omega)$ and $B_p(R,\omega)$ curves at $\omega \approx R$ and the extra current-induced van Hove peaks in Figures 4.4d and 4.5b. We get a clear symmetry breaking a these energies, but not necessarily the largest one. Apart from these peaks, the vanishing B_i values are due to the local density of states graphs for each site *crossing* each other, and are therefore not an indication of an absence of current effects, but rather that currents alter the LDOS in a way we do not have a detailed description of, but is clearly *different* for different C4-related sites. The particular shape of the curve is not our main focus. The main thing to be noted is that the symmetry breaking is not present at all energies, and vanishes for different energies for copper and oxygen. If these curves are to serve as guides for an experiment, it will thus be necessary to search for the symmetry breaking over a range of energies to find the proper signal. The result is encouraging, though, in the sense that large peaks are present at very low energies.

[2]The (very) sceptical reader might see some (very) small wiggles on the $B_d(0,\omega)$- and/or $B_p(0,\omega)$-curve. This is due to some rounding error either in Matlab's way of displaying data or our pdf-conversion of the figure.

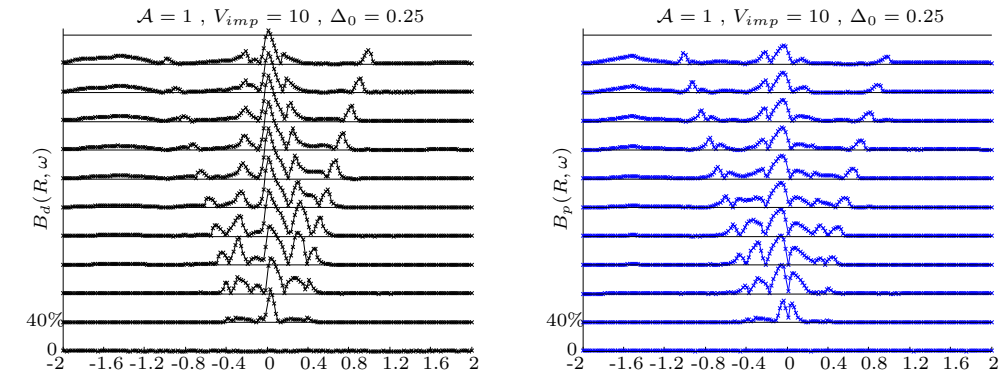

(a) The x-axis is ω in eV.

(b) The x-axis is ω in eV.

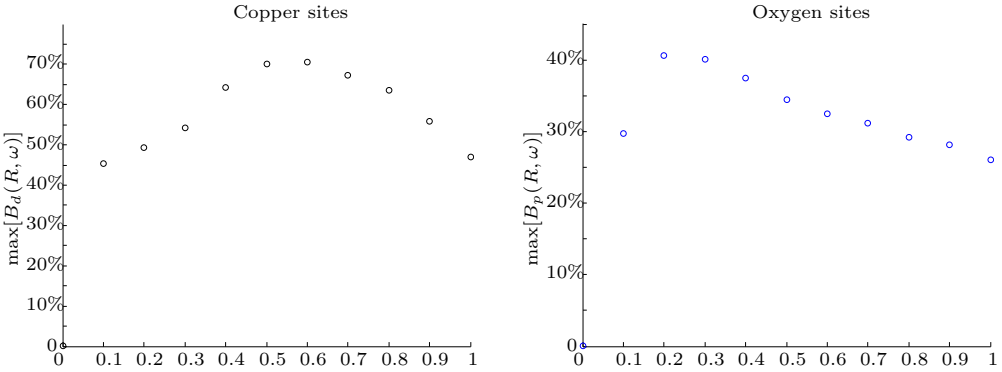

(c) The x-axis is $\mathrm{Im}(R) = |R|$.

(d) The x-axis is $\mathrm{Im}(R) = |R|$.

Figure 4.7: The quantification of the π-rotational invariance breaking. Top panels ((a) and (b)): We increase R in steps of length 0.1 from 0 to i. R is increased upwards, so that the bottom curve corresponds to $R = 0$. Shown are the resulting B_i curves, offset by 40% with respect to each other. Bottom panels ((c) and (d)): The maximum of $B_i(R,\omega)$ over all ω is shown for each R-value. The eleven curves of each top panel thus become eleven points in a corresponding bottom panel.

Having established all this for the superconducting case, we must of course also investigate how the local density of states changes around the impurity when no superconductivity is present in the system. We investigate this by repeating the calculation leading to Figure 4.7 but with $\Delta_0 = 0$. In this calculation we let $|R|$ go all the way to 2, as we have no obligations towards the other order parameter in the system. The result is displayed in Figure 4.8. Once again, the symmetry is completely intact if $R = 0$, whereas any non-zero R yields a difference between the LDOS for the sites in question. Interestingly, the magnitude of the symmetry breaking is substantially lower than when superconductivity was also included. Retrospectively, this might indicate why the curves in Figures 4.7c and 4.7d seem to fall off after an initial increase as $|R|$ is increased; the current order suppresses the superconductivity, and the symmetry breaking approaches its "normal state value". This value - the maximal symmetry breaking as quantified by $B_i(R,\omega)$ in the normal state - has the expected monotonic dependence of R. We stress that we of course do not expect $\max_\omega[B_i(R,\omega)]$ to be completely unbounded; there is a natural

The largest points in the plotted arrays for $R = 0$ have the values $1.2588 \cdot 10^{-14}$, and $1.0540 \cdot 10^{-13}$, respectively. The curves thus ought to be completely straight.

limit set by the vanishing of the LDOS value of any one particular orbital at one of the sites in question (what we try to convey is that the difference in equations (4.23) and (4.24) is of course maximal when one of the ρ's vanishes), in which case $\max_\omega[B_i(R,\omega)]$ is 200 %. But for non-pathological values, a monotonic connection is the immediate expectation for the curves in Figure 4.7.

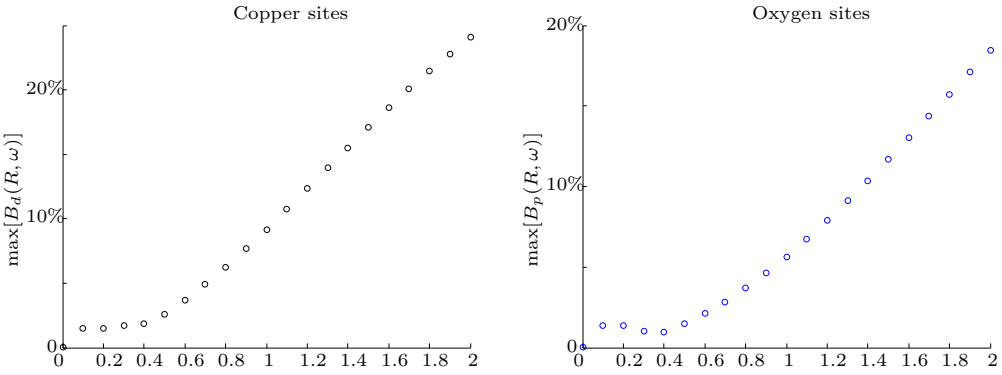

(a) The x-axis is $\mathrm{Im}(R) = |R|$.

(b) The x-axis is $\mathrm{Im}(R) = |R|$.

Figure 4.8: A very simple relationship: the larger $|R|$, the larger the maximal difference between the local state density on the C4-related sites.

4.6 The Varma parameters

We now present similar results for the case when the hybridization energies vanish, i.e., when $\epsilon_d = \epsilon_p = 0$. Although these parameters are favoured by Varma and used in his own mean-field theory (in [12]), they have one major drawback with respect to what we are doing: they do not support superconductivity. This can be seen from Figure 4.9, where it is obvious that the copper does not have enough spectral weight at the Fermi level to support Cooper pair condensation. This is also what our calculations show us, the (L)DOS is virtually unaltered by a non-vanishing Δ_0. We therefore leave superconductivity out of the picture for the remainder of this section.

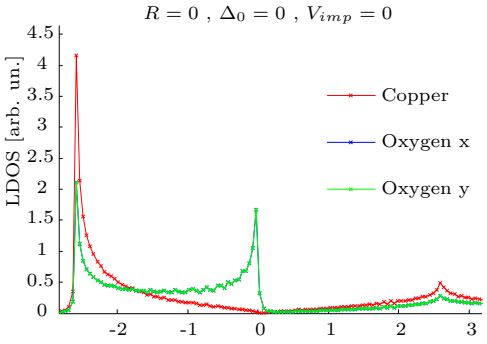

(a) The x-axis is ω in eV.

Figure 4.9: The bulk density of states with Varma's parameters in the current-less normal state.

Apart from the lacking support of superconductivity, the results are very similar to those of the previous section. In Figure 4.10 we display the real space LDOS modulations around

the impurity with and without a current value. We have set the energy to be $\omega = -0.5$ eV, in order to pick up some signal from all three orbitals. The plot is very illustrative in showing how the rotational invariance of the LDOS pattern is lost when a current value is present.

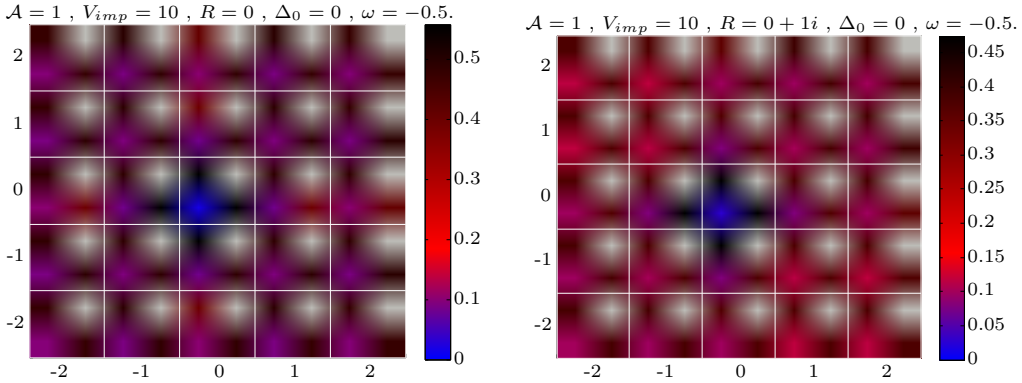

(a) The current-less normal state.

(b) The current possesing normal state.

Figure 4.10: Real space grid with the calculated LDOS-values. The axes are labelled in accordance with Figure 4.3. The colour bar to the right of each plot shows the DOS in the same arbitrary units as Figure 4.9. The impurity is placed on the copper orbital in the [0 0] unit cell, and appears as a brigt blue square in both plots. The grey squares are empty positions, and thus have the LDOS value zero. One difference between the two plots is immediate: currents alter the spatial LDOS pattern significantly.

As was the case in the previous section, we would like to press the envelope a little, and go beyond merely depicting the effect. We therefore perform the calculation described by equations (4.22) to (4.24), once again for the unit cells at respectively $x = -1$, $y = -1$ and $x = -1$, $y = 1$. What we find - as depicted in Figure 4.11 - are some exceedingly large values for $\max_\omega[B_d(R,\omega)]$ and $\max_\omega[B_p(R,\omega)]$. First and foremost, these graphs solidify what we are at this point confident about: no R means an intact C4 symmetry. Furthermore, they might loosely hint that current effects are even more predominant with the hybridization energies that are more or less "tailored" to this end.

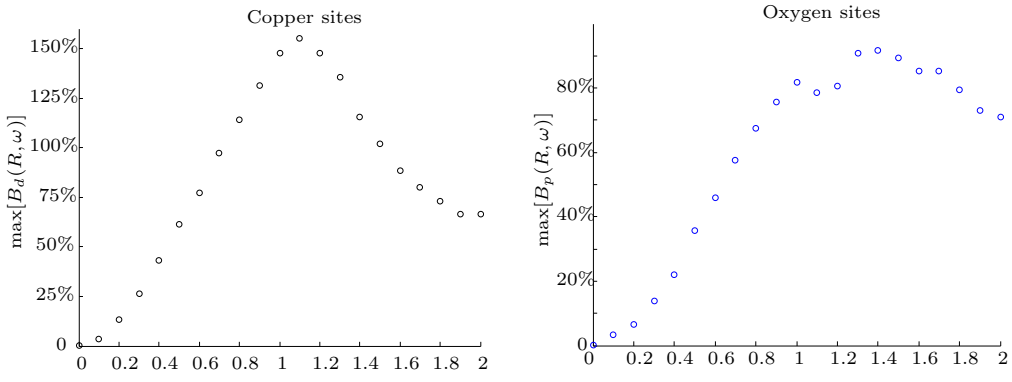

(a) The x-axis is $\mathrm{Im}(R) = |R|$.

(b) The x-axis is $\mathrm{Im}(R) = |R|$.

Figure 4.11: Results for the same calculation as in Figure 4.7, but for $\epsilon_d = \epsilon_p = 0$ and without superconductivity.

This concludes our presentation of specific LDOS results. In the next section we introduce the Fourier transform of the LDOS, a quantity that will play an important role in the next

chapter, which is dedicated to a comprehensive symmetry analysis and a physical interpretation of the broken symmetries.

4.7 Homogeneous FT-LDOS

Apart from spatial symmetry breakings around an impurity, it was our hope that a second loop-current fingerprint might appear in the Fourier transform of the homogeneous local density of states. Obviously, a real-space LDOS grid that breaks, say, C4-symmetry will also yield a Fourier transformed map that breaks C4-symmetry. But in the homogeneous case, it might be relevant to see if circulating currents would alter the weight of the different peaks that constitute the Fourier transformed LDOS. This is a relevant question to ask, as it is experimentally a commonly employed technique to Fourier transform the real-space STM image, and do the real analysis in the momentum representation[3] (see e.g. [15]).

Our goal is now to calculate the so-called power spectrum of the homogeneous system, which is really nothing but the absolute value of the Fourier transform of the real-space LDOS grid. Since the grid consists of non-negative numbers, the Fourier transform of it will in general be complex, and it is customary to look at the absolute value of it.

For a one-band system, the LDOS grid will have the same value at every, call it A, and the FT-LDOS will simply give rise to a peak at $\mathbf{q} = 0$. This is easily shown. Let $\rho(\mathbf{r}, \omega)$ be the local density of states and $\rho(\mathbf{q}, \omega)$ the Fourier transform hereof. Then the LDOS can be written as

$$\rho(\mathbf{r}, \omega) = \sum_{\mathbf{R}} A\delta(\mathbf{r} - \mathbf{R}), \tag{4.25}$$

with $\mathbf{R}$ denoting the position of each atom. For the FT-LDOS, we then find that

$$\begin{aligned}\rho(\mathbf{q}, \omega) &= \frac{1}{N}\sum_{\mathbf{r}} \rho(\mathbf{r}, \omega)\mathrm{e}^{-i\mathbf{r}\cdot\mathbf{q}} \\ &= \frac{1}{N}A\sum_{\mathbf{R}} \mathrm{e}^{-i\mathbf{q}\cdot\mathbf{R}} \\ &= A\delta(\mathbf{q}),\end{aligned} \tag{4.26}$$

in other words, a peak at $\mathbf{q} = 0$ with the value A and nothing else. For the three-band case, the picture is a little more complicated, but not much. Let us assume that we have a grid with four different values, A, B, C, and D, and that they are positioned in the following way:

$$\begin{array}{cccc} C & D & C & D \\ A & B & A & B \\ C & D & C & D \\ A & B & A & B \end{array}$$

with this pattern repeating itself, and with the distance between two A-positions being one. Then we can write the LDOS as

$$\begin{aligned}\rho(\mathbf{r}, \omega) = \sum_{n\in\mathbb{Z}} \Big[& A\delta(x-n)\delta(y-n) + B\delta(x-(n+\tfrac{1}{2}))\delta(y-n) \\ & + C\delta(x-n)\delta(y-(n+\tfrac{1}{2})) + D\delta(x-(n+\tfrac{1}{2}))\delta(y-(n+\tfrac{1}{2}))\Big].\end{aligned} \tag{4.27}$$

[3] Quoth an anonymous source from the theoretical department: "He's an experimentalist... -Those guys *live* in **k**-space!".

The Fourier transform is then seen to be

$$\rho(\mathbf{q},\omega) = \sum_{n\in\mathbb{Z}} \Big[A\mathrm{e}^{-iq_x(x-n)}\mathrm{e}^{-iq_y(y-n)} + B\mathrm{e}^{-iq_x(x-(n+\frac{1}{2}))}\mathrm{e}^{-iq_y(y-n)} + C\mathrm{e}^{-iq_x(x-n)}\mathrm{e}^{-iq_y(y-(n+\frac{1}{2}))} + D\mathrm{e}^{-iq_x(x-(n+\frac{1}{2}))}\mathrm{e}^{-iq_y(y-(n+\frac{1}{2}))}\Big]. \tag{4.28}$$

One may directly read off at which points in $\mathbf{q}$-space constructive interference is obtained. At $\mathbf{q} = 0$, we get a coherent contribution from all four values. At $\mathbf{q} = (0, 2\pi)$ (i.e., $q_x = 0$ and $q_y = 2\pi$) A and B will have the same sign, whereas C and D will have opposite signs. Similarly one can deduct what the contributions at the two other relevant peaks will be. Now, for our purposes, D is of course always zero. If we denote the four relevant places in $\mathbf{q}$-space as $\mathbf{q}_1 = (0, 0)$, $\mathbf{q}_2 = (2\pi, 0)$, $\mathbf{q}_3 = (0, 2\pi)$, and $\mathbf{q}_4 = (2\pi, 2\pi)$, and write what A, B, and C really corresponds to in terms of Green's functions, we then have that

$$|\rho(\mathbf{q}_1,\omega)| = \frac{1}{\pi}\left|\mathrm{Im}[G^0_{11}(0,\omega)] + \mathrm{Im}[G^0_{22}(0,\omega)] + \mathrm{Im}[G^0_{33}(0,\omega)]\right| \tag{4.29}$$

$$|\rho(\mathbf{q}_2,\omega)| = \frac{1}{\pi}\left|\mathrm{Im}[G^0_{11}(0,\omega)] - \mathrm{Im}[G^0_{22}(0,\omega)] + \mathrm{Im}[G^0_{33}(0,\omega)]\right| \tag{4.30}$$

$$|\rho(\mathbf{q}_3,\omega)| = \frac{1}{\pi}\left|\mathrm{Im}[G^0_{11}(0,\omega)] + \mathrm{Im}[G^0_{22}(0,\omega)] - \mathrm{Im}[G^0_{33}(0,\omega)]\right| \tag{4.31}$$

$$|\rho(\mathbf{q}_4,\omega)| = \frac{1}{\pi}\left|\mathrm{Im}[G^0_{11}(0,\omega)] - \mathrm{Im}[G^0_{22}(0,\omega)] - \mathrm{Im}[G^0_{33}(0,\omega)]\right|, \tag{4.32}$$

where we have understood the free Green's function to be a function of position and energy, and, due to the translation invariance of the free Green's function, just simply evaluated it at the origin. Due to the symmetry between p_x and p_y in the free case, only three different values are actually obtained. By means of this, the plots of Figure 4.12 were obtained.

These FT-LDOS plots look a lot similar the orbitally resolved LDOS plots of Figure 4.4, and as such do not reveal anything profoundly new to us. The somewhat fragile co-existence between current pattern 1 and superconductivity discussed in section 4.5 is seen again in 4.12a. For all three parameter choices, current pattern 3 hardly seems to change anything. The view of current pattern 3 as experimentally undetectable will find further support in our analysis in the next chapter. The conclusion is along the lines of the concluding remarks of chapter 3; an impurity is needed to reveal a loop-current fingerprint to an STM apparatus.

4.8 Summary and outlook

We have now presented the calculational scheme we employ and presented some results of this calculation. As there are many parameters to vary, there are many places to look for fingerprints of the loop currents. We believe to have found a good candidate for a smoking gun in the breaking of π rotational symmetry. Regardless of parameter choices and co-existence with superconductivity, this effect is clearly present as long as the mean-field parameter for the currents is non-vanishing. The reader may have wondered why only the $\mathcal{A} = 1$ case was covered, and if any other spatial symmetries could have been broken. In the next chapter, we present a more detailed analysis of how the different current patterns alter the spatial symmetries of the system.

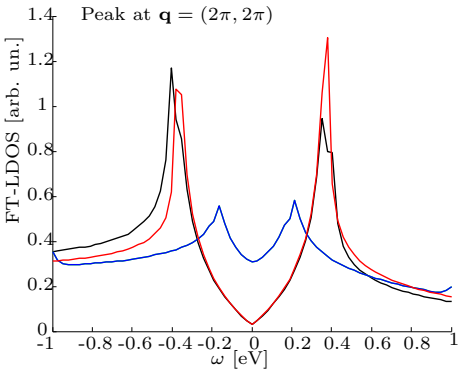

(a) Parameters: $\Delta_0 = 0.25$, $\epsilon_d = -1.5$, $\epsilon_p = -5$.

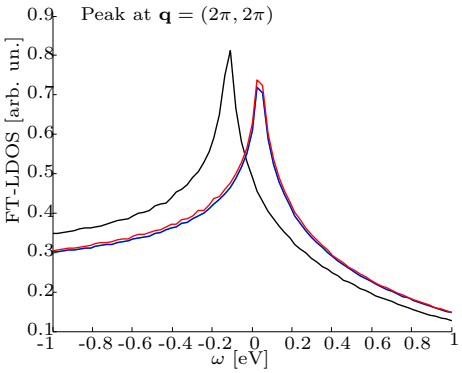

(b) Parameters: $\Delta_0 = 0$, $\epsilon_d = -1.5$, $\epsilon_p = -5$.

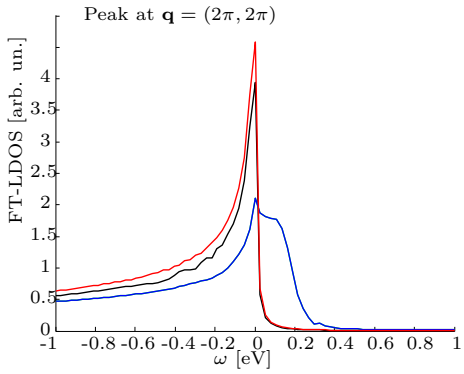

(c) Parameters: $\Delta_0 = 0$, $\epsilon_d = 0$, $\epsilon_p = 0$.

Figure 4.12: Three versions of the FT-LDOS peak at $\mathbf{q} = (2\pi, 2\pi)$ as a function of energy. In all three plots the black curve is for the current-less case, the blue curve is for the $\mathcal{A} = 1, 2$ cases (they are identical) with $R = i$, and the red curve is for the $\mathcal{A} = 3$ case with R=1.

Chapter 5

Analysing the results

In the previous chapter we found our main numerical result: that a mean-field loop current theory breaks a spatial symmetry of the LDOS pattern around a single impurity. In this chapter we try to achieve a better and more systematic understanding of this phenomenon. We first try to classify which symmetries the different current patterns (see chapter 3) may break, and then we give a physical reason for the occurrence of the breaking.

5.1 Symmetry considerations

We now systematically investigate how the presence of currents might affect the symmetries of the LDOS. We do this for the normal state of the system, in order to clearly distinguish which features are solely due to the circulating currents.

5.1.1 The impurity contribution

The key to finding spatial symmetries of the system will be the full Green's function at a certain lattice point. As we saw in the previous chapter, this is given by

$$G(\mathbf{r},\mathbf{r},\omega) = G^0(0,\omega) + G^0(\mathbf{r},\omega)TG^0(-\mathbf{r},\omega). \tag{5.1}$$

Obviously, the first term will be invariant under any symmetry operation we can cook up; it is simply constant in space. We thus focus on the second term, which we shall denote as $\delta G(\mathbf{r},\mathbf{r},\omega)$, i.e.,

$$\delta G(\mathbf{r},\mathbf{r},\omega) = G^0(\mathbf{r},\omega)TG^0(-\mathbf{r},\omega). \tag{5.2}$$

In the case of a point-like impurity residing only on a copper orbital, the T-matrix takes the following simple form:

$$T = [1 - H_{\text{imp}}G^0(0,\omega)]^{-1}H_{\text{imp}} \tag{5.3}$$

$$= \left[1 - \begin{bmatrix} V & 0 & 0 \\ 0 & 0 & 0 \\ 0 & 0 & 0 \end{bmatrix} G^0(0,\omega)\right]^{-1} \begin{bmatrix} V & 0 & 0 \\ 0 & 0 & 0 \\ 0 & 0 & 0 \end{bmatrix} \tag{5.4}$$

$$= \begin{bmatrix} \frac{V}{1-VG^0_{11}(0,\omega)} & 0 & 0 \\ 0 & 0 & 0 \\ 0 & 0 & 0 \end{bmatrix}. \tag{5.5}$$

Futhermore, as our goal is to analyze the spatial symmetries of the system, we can consider ω to be fixed. The T-matrix is then just a constant. We denote the non-zero entry by α;

$$\alpha := \frac{V}{1 - VG^0_{11}(0,\omega)}. \tag{5.6}$$

For each orbital, the impurity contribution to the full Green's function can then be written as

$$\delta G_{11}(\mathbf{r},\mathbf{r},\omega) = \alpha G^0_{11}(\mathbf{r},\omega)G^0_{11}(-\mathbf{r},\omega) \tag{5.7}$$
$$\delta G_{22}(\mathbf{r},\mathbf{r},\omega) = \alpha G^0_{21}(\mathbf{r},\omega)G^0_{12}(-\mathbf{r},\omega) \tag{5.8}$$
$$\delta G_{33}(\mathbf{r},\mathbf{r},\omega) = \alpha G^0_{31}(\mathbf{r},\omega)G^0_{13}(-\mathbf{r},\omega) \tag{5.9}$$

These three contributions all share the same common structure of being the product of two *free* Green's function entries. In terms of momenta, we exploit the $\mathbf{k}$-diagonal structure of the free Green's function to rewrite the product as

$$\delta G_{ii}(\mathbf{r},\mathbf{r},\omega) = \alpha G^0_{i1}(\mathbf{r},\omega)G^0_{1i}(-\mathbf{r},\omega) \tag{5.10}$$
$$= \alpha \sum_{\mathbf{k},\mathbf{k}'} G^0_{i1}(\mathbf{k},\omega)G^0_{1i}(\mathbf{k}',\omega)\mathrm{e}^{-i\mathbf{r}\cdot(\mathbf{k}-\mathbf{k}')}\mathrm{e}^{\phi_i(\mathbf{k},\mathbf{k}')}, \tag{5.11}$$

where $\phi_i(\mathbf{k},\mathbf{k}')$ accounts for the intra-unit cell structure. This formula will be the starting point for our symmetry considerations. First, we find symmetries that are present when $R = 0$, and subsequently we show how many of these are (in general) broken as R is increased.

5.1.2 Symmetries for $R = 0$

Let us now focus on the copper Greens function. The oxygen cases are slightly more complicated due to the way we spatially label p_x and p_y-orbitals, but largely follow the same arguments. Let S be some symmetry operation[1] we suspect the system to be invariant under and let $\mathbf{r}' = S\mathbf{r}$. We then have invariance if $\delta G_{11}(\mathbf{r},\mathbf{r},\omega) = \delta G_{11}(\mathbf{r}',\mathbf{r}',\omega)$. In terms of equation (5.11), this can be recast as having (recall that $\phi_1(\mathbf{k},\mathbf{k}') = 0$)

$$\sum_{\mathbf{k},\mathbf{k}'} f(\mathbf{k})f(\mathbf{k}')\mathrm{e}^{i\mathbf{r}\cdot(\mathbf{k}'-\mathbf{k})} = \sum_{\mathbf{k},\mathbf{k}'} f(\mathbf{k})f(\mathbf{k}')\mathrm{e}^{iS\mathbf{r}\cdot(\mathbf{k}'-\mathbf{k})}, \tag{5.12}$$

with $f(\mathbf{k}) = G^0_{11}(\mathbf{k},\omega)$. The right hand side can then be further rewritten as

$$\sum_{\mathbf{k},\mathbf{k}'} f(\mathbf{k})f(\mathbf{k}')\mathrm{e}^{iS\mathbf{r}\cdot(\mathbf{k}'-\mathbf{k})} = \sum_{\mathbf{k},\mathbf{k}'} f(\mathbf{k})f(\mathbf{k}')\mathrm{e}^{i\mathbf{r}\cdot(S^T\mathbf{k}'-S^T\mathbf{k})} \tag{5.13}$$
$$= \sum_{S\mathbf{k},S\mathbf{k}'} f(S\mathbf{k})f(S\mathbf{k}')\mathrm{e}^{i\mathbf{r}\cdot(\mathbf{k}'-\mathbf{k})}. \tag{5.14}$$

As S by assumption leaves the sum over the Brillouin zone invariant[2], the restriction for invariance is then that

$$\sum_{\mathbf{k},\mathbf{k}'} f(\mathbf{k})f(\mathbf{k}')\mathrm{e}^{i\mathbf{r}\cdot(\mathbf{k}'-\mathbf{k})} = \sum_{\mathbf{k},\mathbf{k}'} f(S\mathbf{k})f(S\mathbf{k}')\mathrm{e}^{i\mathbf{r}\cdot(\mathbf{k}'-\mathbf{k})}, \tag{5.15}$$

and if this is to hold for arbitrary $\mathbf{r}$, the terms multiplying the same phase must be equal, and we finally see that we must have

$$\sum_{\mathbf{k},\mathbf{k}'} f(\mathbf{k})f(\mathbf{k}') = \sum_{\mathbf{k},\mathbf{k}'} f(S\mathbf{k})f(S\mathbf{k}'), \tag{5.16}$$

[1] More precisely: S is an orthogonal transformation.
[2] We still cover the exact same $\mathbf{k}$-points.

along all lines where $\mathbf{k} - \mathbf{k}'$ is equal to the same constant (vector). This latter requirement can be explicitly verified in the absence of currents for a number of symmetries, where we have $f(\mathbf{k}) = f(S\mathbf{k})$.

Let us write out what $f(k_x, k_y)$ is for copper. In order to do so, we need an explicit form of the Hamiltonian. We use our usual three-orbital one, for now with no orbital currents.

$$G^0_{11}(k_x, k_y, \omega) = (1(\omega + i\eta) - H(k_x, k_y))^{-1}_{11} \tag{5.17}$$

$$= \frac{(\omega + i\eta - \epsilon_p)^2 - (4t_{pp}s_x s_y)^2}{\det[1(\omega + i\eta) - H(k_x, k_y)]} \tag{5.18}$$

Upon expansion, the determinant takes the form

$$\begin{aligned}\det[1(\omega + i\eta) - H(k_x, k_y)] &= (\omega + i\eta - \epsilon_d)(\epsilon_p^2 - (4t_{pp}s_x s_y)^2) \\ &+ 2it_{pd}s_x([\omega + i\eta - \epsilon_p]2it_{pd}s_x - 4t_{pp}s_x s_y 2it_{pd}s_y) \\ &+ 2it_{pd}s_y([\omega + i\eta - \epsilon_p]2it_{pd}s_y - 4t_{pp}s_x s_y 2it_{pd}s_x).\end{aligned} \tag{5.19}$$

We can now immediately read off a number of symmetries for the LDOS. Two apparent ones are reflection symmetries around the x- and y-axes, corresponding to $k_x \to -k_x$ and $k_y \to -k_y$. And if we can perform these two operations independently of each other, we can of course also perform them at once, and thus inversion invariance[3] follows. C4 invariance is also noted, as a C4 operation for copper amounts to taking $k_x \to -k_y$ and $k_y \to k_x$. From the above expressions, it is clear that

$$G^0_{11}(-k_y, k_x, \omega) = \frac{(\omega + i\eta - \epsilon_p)^2 - (4t_{pp}s_x s_y)^2}{\det[1(\omega + i\eta) - H(-k_y, k_x))]} = G^0_{11}(k_x, k_y, \omega). \tag{5.20}$$

The final symmetries we care for are reflections in the $x = \pm y$ lines. These correspond respectively to $k_x \to k_y$, $k_y \to k_x$ and $k_x \to -k_y$, $k_y \to -k_x$. Once again, the numerator of equation (5.19) is easily seen to be invariant under these transformations, and the same thing holds true for the determinant.

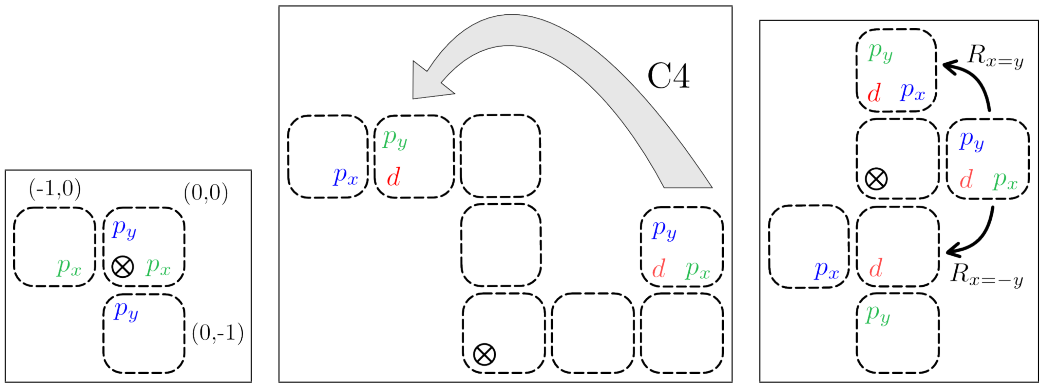

(a) The effect of reflections in the axes and our unit cell labelling.

(b) The effect of a C4 operation. The colours get mapped into themselves, i.e., $d \to d$, $p_x \to p_y$ and $p_y \to p_x$.

(c) The effect of the two "diagonal" reflections. The colours get mapped into themselves, i.e., $d \to d$, $p_x \to p_y$ and $p_y \to p_x$.

Figure 5.1: The ultimate guide to our real-space grid in terms of orbitals and unit cells.

[3]This was already apparent from equation (5.7); sending $\mathbf{r} \to -\mathbf{r}$ just corresponds to commuting two complex numbers. Inversion symmetry is thus manifestly present for copper, irrespective of the form of the Hamiltonian.

We now treat the slightly more complicated oxygen cases. The extra complications all arise from the intra-unit cell structure and the fact that the origin of the system (the position of the impurity) is taken to be at a copper site. Upon a symmetry operation, a d-orbital is always mapped into a d-orbital, but this is not the case for the $p_{x,y}$-orbitals, as illustrated in Figures 5.1a, 5.1b, and 5.1c.

As a first thing, we need the analogue of equation (5.16) for p_x and p_y. The invariance demand expressed in terms of equation (5.11) is

$$\sum_{\mathbf{k},\mathbf{k}'} f_{p_j}(\mathbf{k}) g_{p_j}(\mathbf{k}') \mathrm{e}^{i(k_j/2 - k'_j/2)} = \sum_{\mathbf{k},\mathbf{k}'} f_{p_j}(S\mathbf{k}) g_{p_j}(S\mathbf{k}') \mathrm{e}^{iS(k_j/2 - k'_j/2)}, \quad j = x, y, \tag{5.21}$$

with p_x having

$$f_{p_x}(\mathbf{k}) = \frac{-(\omega + i\eta - \epsilon_p) 2it_{pd} s_x + 2it_{pd} s_y 4t_{pp} s_x s_y}{\det[1(\omega + i\eta) - H(\mathbf{k})]} \tag{5.22}$$

and

$$g_{p_x}(\mathbf{k}) = \frac{(\omega + i\eta - \epsilon_p) 2it_{pd} s_x - 2it_{pd} s_y 4t_{pp} s_x s_y}{\det[1(\omega + i\eta) - H(\mathbf{k})]}, \tag{5.23}$$

whereas it for p_y holds that

$$f_{p_y}(\mathbf{k}) = \frac{(\omega + i\eta - \epsilon_p) 2it_{pd} s_y - 2it_{pd} s_x 4t_{pp} s_x s_y}{\det[1(\omega + i\eta) - H(\mathbf{k})]} \tag{5.24}$$

and

$$g_{p_x}(\mathbf{k}) = \frac{-(\omega + i\eta - \epsilon_p) 2it_{pd} s_y + 2it_{pd} s_x 4t_{pp} s_x s_y}{\det[1(\omega + i\eta) - H(\mathbf{k})]}. \tag{5.25}$$

We have already established the invariance of the determinant under all four reflections, inversion and C4, so it is up to the numerators to decide which symmetries the system possesses. We treat C4 first.

The condition for C4 invariance to hold is that we have (for S being a $\pi/2$ rotation)

$$\delta G_{22}(\mathbf{r}, \mathbf{r}, \omega) = \delta G_{33}(S\mathbf{r}, S\mathbf{r}, \omega). \tag{5.26}$$

From equations (5.22) to (5.25) we see that

$$f_{p_y}(-k_y, k_x) g_{p_y}(-k'_y, k'_x) \mathrm{e}^{i(k_x - k'_x)} = g_{p_x}(k_x, k_y) f_{p_x}(k'_x, k'_y) \mathrm{e}^{i(k_x - k'_x)}, \tag{5.27}$$

and C4 invariance is thus also established for the oxygen orbitals.

For reflections in the $x = y$ line, the proper invariance demand is that (for S now being the relevant reflection)

$$\delta G_{22}(\mathbf{r}, \mathbf{r}, \omega) = \delta G_{33}(S\mathbf{r}, S\mathbf{r}, \omega) \tag{5.28}$$

From equations (5.22) to (5.25) we see that

$$f_{p_y}(k_y, k_x) g_{p_y}(k'_y, k'_x) \mathrm{e}^{i(k_x - k'_x)} = g_{p_x}(k_x, k_y) f_{p_x}(k'_x, k'_y) \mathrm{e}^{i(k_x - k'_x)}, \tag{5.29}$$

and the first reflection invariance is thus also established for the oxygen orbitals.

The remaining reflections are a bit more tricky, as we - as seen from Figures 5.1a, 5.1b, and 5.1c - should modify the S in equation (5.21) to be the symmetry we consider plus a shift to a nearest neighbouring unit cell. Let us clarify this enigmatic statement with a concrete example.

For a reflection in the x-axis, the utter invariance of $\delta G_{33}(\mathbf{r}, \mathbf{r}, \omega)$ is immediate. For p_x, one might naïvely assume the $x \to -x$ invariance demand to be that (for S being a reflection in the x-axis)

$$\delta G_{22}(\mathbf{r}, \mathbf{r}, \omega) = \delta G_{22}(S\mathbf{r}, S\mathbf{r}, \omega). \tag{5.30}$$

However, a careful study of Figure 5.1a reveals that the proper demand is rather

$$\delta G_{22}(\mathbf{r},\mathbf{r},\omega) = \delta G_{22}(S\mathbf{r}-\hat{x},S\mathbf{r}-\hat{x},\omega), \tag{5.31}$$

where $\hat{x}$ is a unit vector in the x direction. A rewriting of the right hand side reveals that

$$\begin{aligned}\delta G_{22}(S\mathbf{r}-\hat{x},S\mathbf{r}-\hat{x},\omega) &= \alpha\sum_{\mathbf{k},\mathbf{k}'} f_{p_x}(k_x,k_y)g_{p_x}(k'_x,k'_y)\mathrm{e}^{i(-x-1,y)\cdot(\mathbf{k}-\mathbf{k}')}\mathrm{e}^{i(k_x/2-k'_x/2)} &(5.32)\\ &= \alpha\sum_{\mathbf{k},\mathbf{k}'} f_{p_x}(k_x,k_y)g_{p_x}(k'_x,k'_y)\mathrm{e}^{i(-x,y)\cdot(\mathbf{k}-\mathbf{k}')}\mathrm{e}^{i(k'_x/2-k_x/2)} &(5.33)\\ &= \alpha\sum_{\mathbf{k},\mathbf{k}'} f_{p_x}(-k_x,k_y)g_{p_x}(-k'_x,k'_y)\mathrm{e}^{i(x,y)\cdot(\mathbf{k}-\mathbf{k}')}\mathrm{e}^{i(k_x/2-k'_x/2)}. &(5.34)\end{aligned}$$

What remains to check is therefore whether $f_{p_x}(k_x,k_y)g_{p_x}(k'_x,k'_y) = f_{p_x}(-k_x,k_y)g_{p_x}(-k'_x,k'_y)$, and as this holds, we have invariance under reflection in the y-axis. In a completely similar way, one can convince oneself that reflection in the x-axis is also a symmetry of the oxygen LDOS.

Finally, we treat reflections in the $x=-y$ line. Let S be this transformation (i.e., $Sx=-y$, $Sy=-x$.). Invariance then implies that

$$\delta G_{22}(\mathbf{r},\mathbf{r},\omega) = \delta G_{33}(S\mathbf{r}-\hat{y},S\mathbf{r}-\hat{y},\omega), \tag{5.35}$$

which is easily verified in the same manner as above.

To summarize, we have now seen that the non-current carrying system in the normal state possesses the following symmetries for the LDOS around an impurity on a copper site:

- Rotations by π (C4).
- Reflections in the axes.
- Reflections in the diagonals.
- Inversion.

A breaking of *any* of these will thus be a potential loop-current fingerprint.

5.1.3 Unbroken symmetries when $R \neq 0$

Along the lines of the previous section, we are able to show that some of the aforementioned symmetries remain unbroken in the loop-current state. This is really a thing to rejoice in; had the orbital-currents broken all of the symmetries, it would experimentally be indistinguishable from a wild and uncontrolled impurity (a defect of the sample). Some of the symmetries we are able to show will hinge on R being either real or imaginary. We comment on this as we go along, and then collect all these findings at the end of the section.

We follow arguments completely identical to those of the previous section. Let us therefore cut right to the chase.

For the $\mathcal{A}=1$ case, the determinant in question takes the form

$$\begin{aligned}\det[1(\omega+i\eta)-H_1(\mathbf{k})] &= (\omega+i\eta-\epsilon_d)([\omega+i\eta-\epsilon_d]^2-(4t_{pp}s_xs_y)^2)\\ &\quad-(-2it_{pd}s_x+Rc_x)(2it_{pd}s_x+R^*c_x)(\omega+i\eta-\epsilon_p)\\ &\quad+(-2it_{pd}s_x+Rc_x)4t_{pp}s_xs_y(2it_{pd}s_y-R^*c_y)\\ &\quad+(2it_{pd}s_y+Rc_y)4t_{pp}s_xs_y(-2it_{pd}s_x-R^*c_x)\\ &\quad-(2it_{pd}s_y+Rc_y)(-2it_{pd}s_y+R^*c_y)(\omega+i\eta-\epsilon_p).\end{aligned} \tag{5.36}$$

How about the numerators in the expressions for the Green's function entries?

Well,

$$G^0_{11}(\mathbf{k},\omega) = \frac{(\omega + i\eta - \epsilon_p)^2 - (4t_{pp}s_x s_y)^2}{\det[1(\omega + i\eta) - H_1(\mathbf{k})]}, \tag{5.37}$$

and the currents thus do not alter the inversion invariance of the copper LDOS. For the oxygen atoms,

$$G^0_{21}(\mathbf{k},\omega) = \frac{(\omega + i\eta - \epsilon_p)(-2it_{pd}s_x - R^*c_x) + 4t_{pp}s_x s_y(2it_{pd}s_y - R^*c_y)}{\det[1(\omega + i\eta) - H_1(\mathbf{k})]}, \tag{5.38}$$

$$G^0_{12}(\mathbf{k},\omega) = \frac{(\omega + i\eta - \epsilon_p)(2it_{pd}s_x - Rc_x) + 4t_{pp}s_x s_y(-2it_{pd}s_y - Rc_y)}{\det[1(\omega + i\eta) - H_1(\mathbf{k})]} \tag{5.39}$$

and

$$G^0_{31}(\mathbf{k},\omega) = \frac{(\omega + i\eta - \epsilon_p)(2it_{pd}s_y - R^*c_y) + 4t_{pp}s_x s_y(-2it_{pd}s_x - R^*c_x)}{\det[1(\omega + i\eta) - H_1(\mathbf{k})]}, \tag{5.40}$$

$$G^0_{13}(\mathbf{k},\omega) = \frac{(\omega + i\eta - \epsilon_p)(-2it_{pd}s_y - Rc_y) + 4t_{pp}s_x s_y(2it_{pd}s_x - Rc_x)}{\det[1(\omega + i\eta) - H_1(\mathbf{k})]}. \tag{5.41}$$

Under axis reflections, all the s_i factors change sign, whilst the c_i factors go to themselves, and we see no apparent reason why this should leave the determinant invariant. Nor does it correspond to an overall sign, and must therefore conclude that these two symmetries are possibly not present.

For reflections in the $x = y$ line, the determinant is only invariant if R is real (in which case all three LDOS values are invariant), whereas this demand *is not* present when we consider the $x = -y$ line; we see that the entire LDOS grid is invariant under reflections in the $x = -y$ lines regardless of what R is. C4 is not seen to hold under any assumptions regarding R.

For $\mathcal{A} = 2$ the story is very similar, and the reader may simply let $c_y \to -c_y$ to obtain all the results for this case. One interesting difference is noted, namely that we now have reflection invariance in the $x = y$ line instead of the $x = -y$ line.

For $\mathcal{A} = 3$ the current pattern is a quite different from the $\mathcal{A} = 1, 2$ cases, and we once again write out everything.

$$\begin{aligned}
\det[1(\omega + i\eta) - H_3(\mathbf{k})] = {} & (\omega + i\eta - \epsilon_d)([\omega + i\eta - \epsilon_p]^2 - (4t_{pp}s_x s_y)^2) \\
& + (2it_{pd}s_x + Rs_x)(-2it_{pd}s_x + R^*s_x)(\omega + i\eta - \epsilon_p) \\
& - (2it_{pd}s_x + Rs_x)(2it_{pd}s_y + R^*s_y)4t_{pp}s_x s_y \\
& - (-2it_{pd}s_y + Rs_y)(-2t_{pd}s_x + R^*s_x)4t_{pp}s_x s_y \\
& + (-2it_{pd}s_y + Rs_y)(2it_{pd}s_y + R^*s_y)(\omega + i\eta - \epsilon_p)
\end{aligned} \tag{5.42}$$

Each term in the determinant contains an even number of sines in each direction (meaning x or y), and the determinant is therefore invariant under reflections in the axes independently of each other, and hence also under inversion. The numerators in the Green's function entries are either invariant or change sign, and their products are thus invariant. This is actually as far as we can go; no further symmetries are apparent in the system. We stress that this of course does not mean that they are not present, but simply that it is not immediate whether this is the case. We do not consider $\mathcal{A} = 4$, since, as discussed in chapter 3, this parameter choice did not lead to stable current patters.

In summary, we can draw the current symmetry table Table 5.1, where we only display the symmetries we have explicitly verified.

These are the symmetries we could have read off of the drawings of the current patters depicted in chapter 3 in Figures 3.9 to 3.11, with the inversion symmetry of copper as the possible exception.

Current pattern	$\mathcal{A}=1$		$\mathcal{A}=2$		$\mathcal{A}=3$	
Symmetry ↓	Copper	Oxygen	Copper	Oxygen	Copper	Oxygen
x-axis refl.	-	-	-	-	Yes	Yes
y-axis refl.	-	-	-	-	Yes	Yes
inversion	Yes	-	Yes	-	Yes	Yes
$x=y$ refl.	If R real	If R real	Yes	Yes	-	-
$x=-y$ refl.	Yes	Yes	If R real	If R real	-	-
C4	-	-	-	-	-	-

Table 5.1: Symmetries analytically shown to be unbroken by R.

5.1.4 Comparison with the numerical data

These symmetry considerations for the local density of states around an impurity relate very well to our numerical results. In Table 5.2 are displayed the results of a numerical symmetry analysis of the LDOS around and impurity for different current patterns. The LDOS-grids were computed as described in the previous chapter. The procedure used to retrieve this numerical data was the following. The real-space LDOS grid was computed for three unit cells to each side of the impurity, yielding a total of 49 unit cells, and for the five energies $\omega = 0, \pm 0.2, \pm 0.5$ (in eV). Along the lines of the discussion so far, and the relation of our LDOS results to the orbital current patterns of chapter 3, we employ for each choice of $\mathcal{A}$ the phase of R yielding the maximal current expectation value. For $\mathcal{A} = 1, 2$ we thus chose $R = i$, whereas for $\mathcal{A} = 3$, we took $R = 1$.

The resulting 14×14 matrix was trimmed, so that only orbitals with symmetry partners were left. The meaning of this is illustrated for a slightly smaller field of view in Figure 5.2.

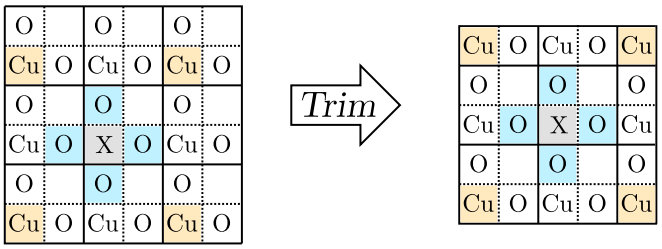

Figure 5.2: The idea of trimming our matrix. As described in chapter 4, what we calculate is not symmetric around the impurity (and thus the origin when talking symmetries). Removing one row and one column fixes this. The colours and dashed lines are guides to the eyes, whereas the solid lines define different unit cells. See also Figures 4.6 and 4.10.

This reduced matrix can then readily be checked for various symmetries by means of elementary matrix operations. Our criterion for symmetry preservation was rather strict; if the absolute value of any entry of the difference between the original matrix and its image under the symmetry operation was non-zero[4] the symmetry was deemed broken. We also did this for the copper sites only, and the results were identical. This was all done thrice, once for the Varma hybridizations and twice for the "realistic" hybridizations, respectively with and without superconductivity. All these six sets of symmetry results turned out to be in agreement, which we take as an encouraging hint on the robustness of our conclusions with respect to different parameter choices. The results are displayed in Table 5.2.

[4]With some reasonable round-off given by numerical specifications such as the **k**-space resolution, size of η etc.

Current pattern	$\mathcal{A}=1$		$\mathcal{A}=2$		$\mathcal{A}=3$	
Symmetry ↓	Copper	Oxygen	Copper	Oxygen	Copper	Oxygen
x-axis refl.	No	No	No	No	Yes	Yes
y-axis refl.	No	No	No	No	Yes	Yes
inversion	Yes	Yes	Yes	Yes	Yes	Yes
$x=y$ refl.	Yes	Yes	Yes	Yes	Yes	Yes
$x=-y$ refl.	Yes	Yes	Yes	Yes	Yes	Yes
C4	No	No	No	No	Yes	Yes

Table 5.2: Symmetries numerically found to be broken for the maximally current-yielding R value. "No" means that the symmetry was explicitly broken in the numerical data, and "Yes" means that it was left unbroken.

A comparison of Tables 5.1 and 5.2 of course reveals no contradictions. But it also seems that a nice feature is lost. In Table 5.1 we see a possible difference in the reflectional symmetries in the $x=\pm y$ lines, displayed by the $\mathcal{A}=1,2$ cases. This can intuitively be related to the actual form of the current patterns. In Table 5.2 there seems to be no difference between the LDOS grids when $\mathcal{A}=1$ and when $\mathcal{A}=2$. To our contentment, one thing does not entirely rule out the other. As seen in Figure 5.3, the intuitive connection between the actual current pattern, seen on the right, and its manifestation as LDOS modulations is not lost. And the modulations respect the same symmetries in both cases. Note that it is the directions of the currents that seem to play no role.

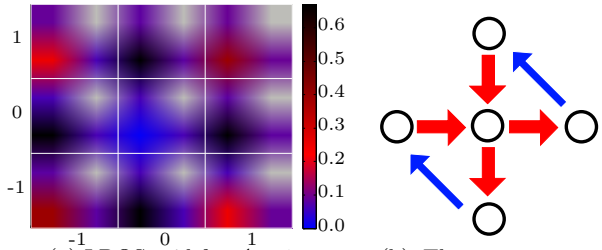

(a) LDOS-grid for $\mathcal{A}=1$.

(b) The current pattern for $\mathcal{A}=1$.

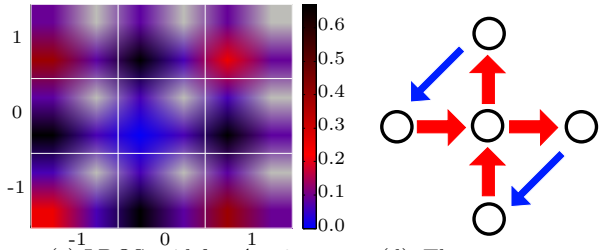

(c) LDOS-grid for $\mathcal{A}=2$.

(d) The current pattern for $\mathcal{A}=2$.

Figure 5.3: Left: real-space LDOS grids. The axes denotes spatial unit cell labelling, the colourbar is LDOS in arb. un., grey represents an empty space. The parameters shared by both plots were $R=i$, $\Delta_0=0.25$, and $\epsilon_d=-1.5$, $\epsilon_p=-5$ (all in eV). Right: the current patterns as calculated in chapter 3.

5.2 Physical explanation in terms of energy contours

Although we in the two previous chapters concluded that no traces of the symmetry breaking was seen in the homogeneous system, the fact that only free Green's functions make up the full Green's function (see equation (4.14)), indicates to us that the real physics of the symmetry loss should somehow be contained in the unperturbed system. But at the same time, an impurity was needed to bring forth this facet of the current-carrying system. The relevant question is then what feature of the unperturbed system otherwise hidden to the density of states a scattering process reveals. The answer is the curves of constant energy, CCEs, on which the scattering takes place. In this section, we consider the Fourier transformed density of states around an impurity, and deduce from the CCEs via a qualitative scattering model that the symmetry of the FT-LDOS is broken, which in turn implies a non-symmetric LDOS.

The curves of constant energy are found by diagonalizing the Hamiltonian in the absence of an impurity.

5.2.1 The octet model

The shape and especially rate of change of constant energy curves reveal a good deal of information to us. Let us briefly explain how the rate of change affects the DOS. We implicitly use two facts about the Dirac-δ function, see e.g. ref. [27] for an explanation.

Let us consider the 3×3 Green's function written, for once, not in the orbital basis, but in the diagonal (band) basis introduced in section 3.2.1. We use the notation of that section in the following. In this diagonal basis, the Green's function can be explicitly written as

$$G(\mathbf{k},\omega) = \begin{bmatrix} \frac{1}{\omega+i\eta-E_\alpha(\mathbf{k})} & 0 & 0 \\ 0 & \frac{1}{\omega+i\eta-E_\beta(\mathbf{k})} & 0 \\ 0 & 0 & \frac{1}{\omega+i\eta-E_\gamma(\mathbf{k})} \end{bmatrix}. \tag{5.43}$$

In the limit where $\eta \to 0$, the spectral function is then given by

$$A(\mathbf{k},\omega) = \begin{bmatrix} 2\pi\delta(\omega-E_\alpha(\mathbf{k})) & 0 & 0 \\ 0 & 2\pi\delta(\omega-E_\beta(\mathbf{k})) & 0 \\ 0 & 0 & 2\pi\delta(\omega-E_\gamma(\mathbf{k})) \end{bmatrix}, \tag{5.44}$$

and the density of states is readily found as

$$\begin{aligned} \rho(\omega) &= \frac{1}{2\pi N}\,\mathrm{Tr}[A(\mathbf{k},\omega)] \\ &= \frac{1}{2\pi N}\sum_{i=\alpha,\beta,\gamma}\sum_{\mathbf{k}} 2\pi\delta(\omega-E_i(\mathbf{k})) \\ &= \frac{1}{N}\sum_{i=\alpha,\beta,\gamma}\sum_{\mathbf{k}}\sum_{j}\frac{\delta(\mathbf{k}-\mathbf{k}_j)}{|\nabla E_i(\mathbf{k})|}, \end{aligned} \tag{5.45}$$

where the $\mathbf{k}_j$-momenta satisfy that $\omega = E_i(\mathbf{k}_j)$ for $i = \alpha, \beta, \gamma$. We thus see that the largest spectral weight is obtained at those places in $\mathbf{k}$-space where the bands have the lowest rate of change. When one makes a cut through the bands in $\mathbf{k}$-space at a range of fixed energies, ω, these regions where $|\nabla E(\mathbf{k})|$ is small will be the regions where the curves of constant energy vary *the most* as ω is changed. This is illustrated in one dimension in Figure 5.4a. Equation (5.45) was obtained for a three-band system in the normal state, but for a system including superconductivity, the corresponding 6×6 derivation is completely analogous, and the main point remains the same: by looking at the curves of constant energy for a small range of ω-values close to each other, we can deduce where in $\mathbf{k}$-space the system has the most spectral weight.

This rather simple observation has led to the proposal of the so-called *octet model* (see e.g. refs. [32] and [33]) to explain the scattering modulations in the Fourier transformed local density of states for a d-wave superconductor. The idea of the octet model is illustrated in Figure 5.4b. In words, the idea is that scattering from one state to another can only occur on a CCE, due to energy conservation. Whereas all energy-conserving scattering events are possible, we expect the scattering processes from a densely populated area to a densely populated area (in **k**-space) to be dominant. If we therefore consider the Fourier transformed local density of states around an impurity, we expect to see large contributions at those **q**-vectors corresponding to such a scattering event. For a d-wave superconductor, there are eight such regions in **k**-space, and an initial state from one region therefore has eight **q**-vectors (including the null vector) of "highly probable" scattering. These eight vectors are depicted in Figure 5.4b. Even if we disregard the null vector, each of the eight hot spots have seven vectors connecting them to other hot spots, yielding 56 potential peaks. Although only 32 of these are actually different, this is still a vast amount of peaks, and not all of them are realized. We shall return to this subject later in this section.

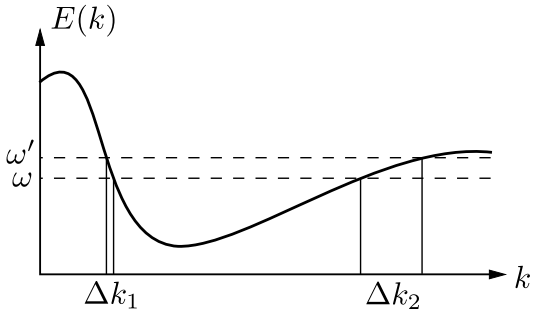

(a) Illustration of the relation between an energy band and its ω-projection. When the band changes slowly as a function of k, the rate of change with respect to ω is large; $\Delta k_2 > \Delta k_1$. This particular band curve is completely fictitious.

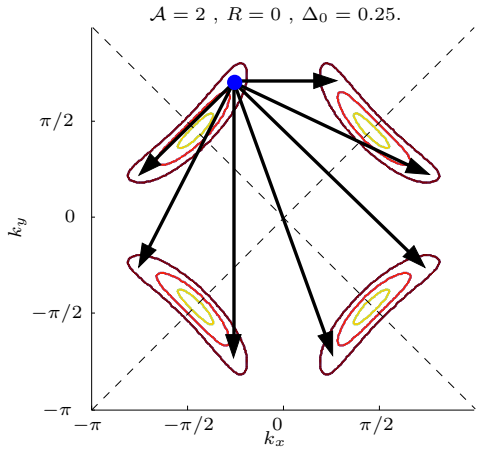

(b) Illustration of the octet model. Shown are the banana shaped CCEs for our three-band (current-less) superconductor in a range around the Fermi energy. The biggest change is obviously at the banana tips.

One can get a feel for the validity of this picture by looking at the actual form of the FT-LDOS. Let us now describe how to find the FT-LDOS around an impurity. In section 4.7 we studied the homogeneous Fourier transformed LDOS and found four peaks in **q**-space. As described in that section, these peaks arise from the particular unit cell structure of our model. Upon computing the FT-LDOS in the non-homogeneous case, those structural peaks will be very dominant and mask almost every other feature. We therefore disregard the free term in the full Greens function, and only find the Fourier transform of the δG-term as defined in equation (5.2).

Let $\delta\rho(\mathbf{q},\omega)$ and $\delta\rho(\mathbf{r},\omega)$ denote the impurity contributions to the FT-LDOS and LDOS, respectively. Then it holds that

$$\delta\rho(\mathbf{q},\omega) = \sum_{\mathbf{r}} \delta\rho(\mathbf{r},\omega)\mathrm{e}^{-i\mathbf{q}\cdot\mathbf{r}}. \tag{5.46}$$

Now, as described in sections 4.3.1 and 2.4, the full density of states contains the sum of the imaginary parts of six Green's function entries. For simplicity, we now focus on the first one,

i.e., the contribution from spin up on copper.

$$\begin{aligned}\frac{-1}{\pi}\sum_{\mathbf{r}}\mathrm{Im}[\delta G_{11}(\mathbf{r},\omega)]\mathrm{e}^{-i\mathbf{q}\cdot\mathbf{r}} &= \frac{1}{2\pi i}\sum_{\mathbf{r}}\delta G_{11}^{*}(\mathbf{r},\omega)\mathrm{e}^{-i\mathbf{q}\cdot\mathbf{r}} - \delta G_{11}(\mathbf{r},\omega)\mathrm{e}^{-i\mathbf{q}\cdot\mathbf{r}} \\ &= \frac{1}{2\pi i}\sum_{\mathbf{r}}\delta G_{11}^{*}(-\mathbf{q},\omega) - \delta G_{11}(\mathbf{q},\omega), \end{aligned} \tag{5.47}$$

where

$$\begin{aligned}\delta G_{11}(\mathbf{q},\omega) &= \sum_{\mathbf{r}}\sum_{\mathbf{k},\mathbf{k}'}[G^{0}(\mathbf{k},\omega)T(\omega)G^{0}(\mathbf{k}',\omega)]_{11}\mathrm{e}^{-i\mathbf{q}\cdot\mathbf{r}}\mathrm{e}^{i\mathbf{k}\cdot\mathbf{r}}\mathrm{e}^{-i\mathbf{k}'\cdot\mathbf{r}} \\ &= \sum_{\mathbf{k}}[G^{0}(\mathbf{k}+\mathbf{q},\omega)T(\omega)G^{0}(\mathbf{k},\omega)]_{11}. \end{aligned} \tag{5.48}$$

The other ten terms are found in a similar manner. From equations (5.47) and (5.48), the main idea of the octet model seems plausible; the quantity in question is large if there is "a lot" of Green's function at $\mathbf{k}$ and $\mathbf{k}+\mathbf{q}$. It is, however, not very evident how well it describes the shape and height of the Fourier amplitudes in question.

We stress that the octet model is not an exact result. For one thing, it does not predict the relative weights at each peak, some of which are indeed often zero. We thus do not see all 32 peaks predicted by the model. Furthermore, in the actual results, the peaks that do survive are often smeared a little to rather give small arcs of high intensity than distinct point-like peaks. But having said this, the octet model still provides us with a good qualitative explanation of our results, especially in terms of symmetries. The validity and limitations of the octet model is discussed further in e.g. refs. [32], [33], and [34].

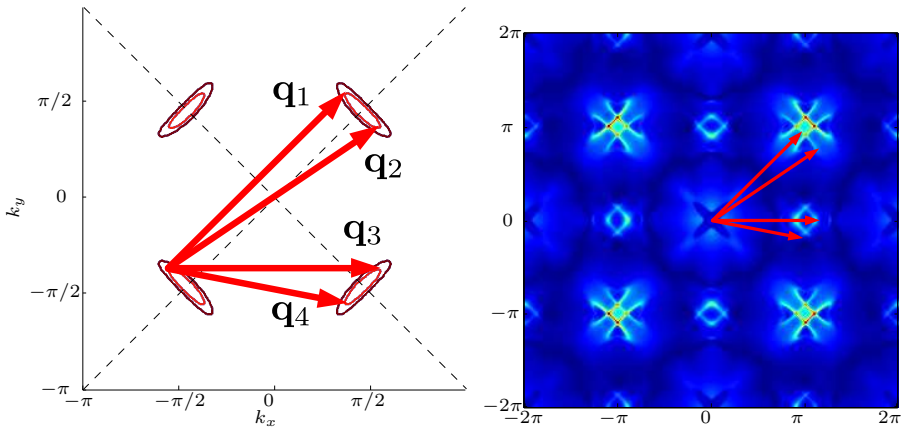

(a) CCEs in the FBZ. The red CCEs are at value.

(b) Power spectrum in $\mathbf{q}$-space calculated at $\omega = 0.1$ eV, the black ones slightly above this $\omega = 0.1$ eV.

Figure 5.4: We identify four vectors connecting banana tips as peaks in the power spectrum. These vectors, found in $\mathbf{k}$-space, are then inserted into $\mathbf{q}$-space, in good agreement with the FT-LDOS in this space. For both plots the parameters were: $\epsilon_d = -1.5$ eV, $\epsilon_p = -5$ eV, $R = 0$, $\Delta_0 = 0.25$.

In Figure 5.4 we explore how some of the aforementioned 32 vectors appear in the FT-LDOS (or more precisely: the power spectrum). The absolute value FT-LDOS plots were calculated as an imitation of the experimental way, by first calculating a large LDOS grid, and then Fourier transforming that. For the plots presented here, the $\mathbf{k}$-space resolution was 325×325

and the LDOS-grid matrix was 302×302 (corresponding to 75 unit cells in each direction away from the impurity). We do not want to make a detailed account of how many peaks are absent or present, but instead focus on some places where we definitely see a signal, a signal that will be substantially altered by the loop currents.

In the current-less case, the CCEs and the FT-LDOS posses a number of symmetries. These symmetries where counted and classified in section 5.1.2. It is relatively straightforward to see how the bunch of four vectors in Figure 5.4a could equally well have been placed at one of three other (left) banana tips by applying *the same* rotation and translation to all of them, and how this four-fold symmetry shows up in the FT-LDOS image of Figure 5.4b. Similarly, we can rediscover all the other symmetries of section 5.1.2 by relating equivalent vectors between banana tips with high power spectrum regions. It is especially worth noting how the diamond-shaped region near $q = (\pi, 0)$ can be generated by $\mathbf{q}_3$ and $\mathbf{q}_4$ and their partners (not shown in the figure for reasons of graphical clarity) emanating from the lowest tip of the South-West banana and ending in the same places as $\mathbf{q}_3$ and $\mathbf{q}_4$.

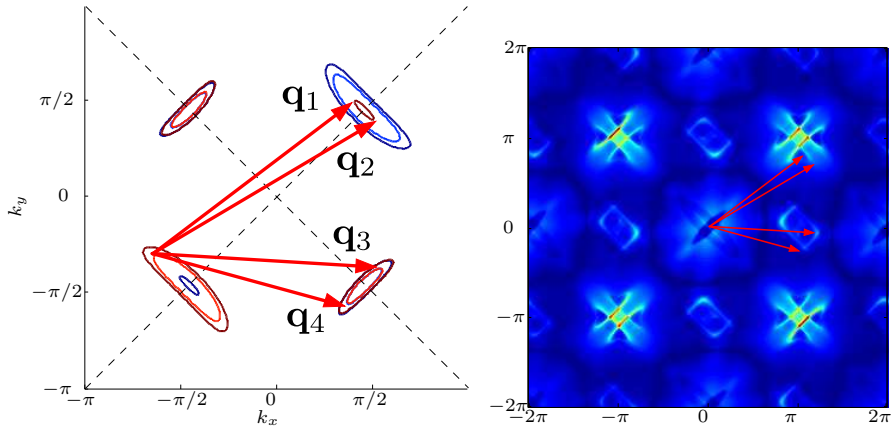

(a) CCEs in the FBZ.

(b) Power spectrum in $\mathbf{q}$-space calculated at $\omega = 0.1$ eV.

Figure 5.5: We identify four vectors connecting banana tips as peaks in the power spectrum. For both plots the parameters were: $\epsilon_d = -1.5$ eV, ϵ_p=-5 eV, $R = 0.1i$, $\Delta_0 = 0.25$.

If we now turn our attention to Figure 5.5, we note that the picture is somewhat different. The four bananas are no longer of the same shape, and scattering vectors in different directions are no longer related by simple symmetry operations. In particular, the q-vectors $\mathbf{q}_3$ and $\mathbf{q}_4$ have been significantly distorted, with an evident effect on the FT-LDOS region in the vicinity of $q = (\pi, 0)$. The diamond-shaped region gets distorted into a general rhombic shape, a shape that is again in very good agreement with the four scattering vectors from the South-West banana to the South-East one.

5.2.2 Beyond the octet model

Although the octet model yields a nice explanation of the observed breaking of symmetry in the FT-LDOS and hence also the LDOS around an impurity, it can not be all there is to the story, as it hinges on the particular banana-shaped CCEs observed in d-wave superconductors, whereas our symmetry breaking was present also in the two non-superconducting cases (see chapter 4). Indeed, it is only a good qualitative explanation, not a rigorous result. What remains true, however, is that scattering does take place on curves of constant energy, and it is therefore a very reasonable assumption that the symmetries of the CCEs are inherited by the

density of states upon scattering off a single point-like impurity (as such an impurity is itself maximally symmetric). This is indeed also what we find. Below we present some calculated CCEs in energy ranges close to the Fermi energy, and we observe a perfect agreement between loop-current pattern, mean-field parameter strength for the currents, broken symmetries and the numerical results presented in section 5.1.4. A more elaborate collection of CCEs is found in Appendix B.

In Figure 5.6 the CCEs for the same parameters as employed in the previous subsection are shown. Figure 5.6a is thus the same picture as Figure 5.4a. In these curves, we once again find the usual symmetry relations between the different current patterns. $\mathcal{A} = 1$ and $\mathcal{A} = 2$ both break the C4 symmetry, and their respective deviations from the currentless case are clearly pronounced in the $k_x = \pm k_y$ lines (cf. Figure 5.3). The energy contours when $\mathcal{A} = 3$ are very hard to distinguish from the currentless case, and in particular respect all the symmetries of that case.

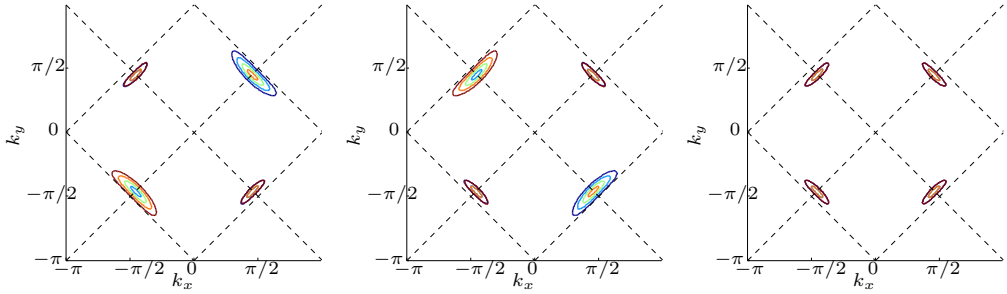

(a) $\mathcal{A} = 1$, $R = 0.1i$ (b) $\mathcal{A} = 2$, $R = 0.1i$ (c) $\mathcal{A} = 3$, $R = 0.1$

Figure 5.6: The curves of constant energy for a range of energy near the Fermi level. Parameters shared by all plots: ϵ_d=-1.5 eV, ϵ_p=-5 eV, $\Delta_0 = 0.25$ eV.

These features are not dependent on superconductivity. When we in Figure 5.7 consider the energy contours for the same hybridization energies as above but without superconductivity, we see essentially the same picture, just somewhat less pronounced. Recalling the "maximum spatial C4 breaking"-plots of Figures 4.7 and 4.8, this is indeed also what we would expect. The main thing to note is once again that the pictures for $\mathcal{A} = 1$ and for $\mathcal{A} = 2$ are very similar, but differ in that the "thickening" of the CCE-lines (i.e., the distance between each line) happen along either the $k_x = k_y$ or the $k_x = -k_y$ line, and of course that $\mathcal{A} = 3$ respects every single symmetry of the current-less system. It is not easily seen where any scattering vectors analogous to the scattering vectors of the octet model might be drawn, and we do not expect the same picturesque correspondence between CCEs and FT-LDOS as in the superconducting case. But it is convincing that the same overall symmetries are present in the CCEs presented here and the spatial LDOS modulations of the previous chapter.

This concludes our analysis of the symmetry breaking in terms of curves of constant energy. The main line of reasoning was the following: elastic scattering takes place from one energy contour to another one of the same energy. If these energy contours lack a certain symmetry, so will the resulting scattering processes and hence also the density of states, both in real- and momentum space. Of course one could imagine special cases where such effects would cancel out (cf. Figure 4.7), but in general this will not be the case.

5.3 Relating our results to real life

From the discussion in this chapter, the main conclusion is clear: if the loop-current theory is realized in the cuprates in the form of current pattern 1 or 2, we expect to see a significant

breaking of C4 symmetry in the density of states around an impurity in the dilute concentration limit. If the currents are realized through current pattern 3, we predict no substantial deviation from not having orbital currents at all.

The latter prediction is somewhat dull. Luckily, the experimental evidence in favour of the loop current theory seems to support the view that current patterns 1 and 2 are being realized in the cuprates. In ref. [9] the magnetic signal signal observed is corresponding to a current pattern similar to our $\mathcal{A} = 1, 2$. The authors also mention an earlier experiment that rules out the current pattern $\mathcal{A} = 3$ as a realistic current pattern. In the (controversial) experiment of ref. [13], the results are also consistent with $\mathcal{A}$ being 1 or 2. Finally, although not directly related to the cuprates, the actual current patterns observed in "bare" CuO and reported in ref. [14] showed a shape similar to the other two experiments mentioned here (cf. Figure 1.5).

If we are to believe in the loop-current theory at all, we are therefore lead to assume the realization of the orbital currents through the current patterns that gave rise to our non-trivial results. What experimental test of Varma's theory do we then propose?

Well, obviously, we propose an STM measurement in the vicinity of a single impurity. In real available samples it is highly unlikely that a single order parameter for the currents would suffice to describe the entire material; instead we must expect different domains of loop order with different current strengths and directions to be present in the sample. Having a large field of view in the STM experiment might then result in an averaging over these different domains, and the symmetry breaking could then be obscured or even lost. This might explain the lack of experimental reports on this matter. As a large field of view is essential for a decent $\mathbf{q}$-space resolution of the FT-LDOS image, our proposal is to remain in real space, and search for a broken spatial symmetry close to the impurity. This should, in the light of the findings of chapter 4, be done for a range of energies at fixed positions. Integration over these energies should be avoided, as this may also result in a masking or loss of the symmetry breaking.

To our knowledge, no such systematic investigation has been performed on a cuprate in the pseudogap part of the superconducting dome.

If such an experiment finds no trace of C4 symmetry breaking, we must consider that to be a serious problem for the loop current theory, but it might of course also indicate some shortcoming of our model. If the experiment however does succeed in capturing this feature of the LDOS modulations, we must conclude it to be a most encouraging result in favour of the loop-current theory. In either case, we believe that such an experiment in the light of our results would add to a tipping of the balance with regard to the success of intra-unit cell orbital currents as the theory to properly explain the pseudogap phase of the cuprates.

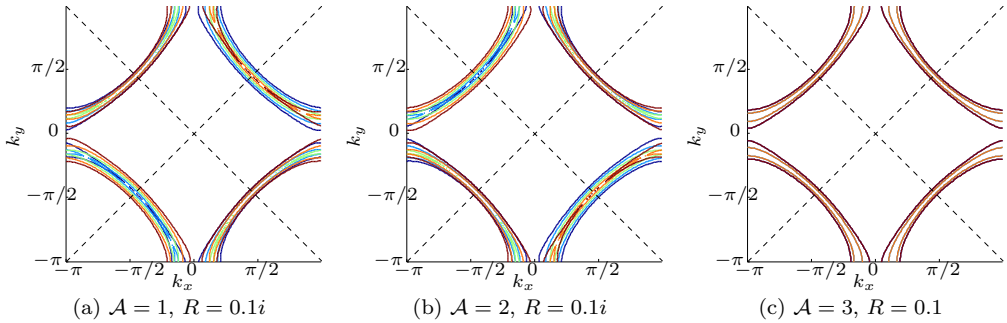

(a) $\mathcal{A} = 1$, $R = 0.1i$ (b) $\mathcal{A} = 2$, $R = 0.1i$ (c) $\mathcal{A} = 3$, $R = 0.1$

Figure 5.7: The curves of constant energy for a range of energy near the Fermi level. Parameters shared by all plots: ϵ_d=-1.5 eV, ϵ_p=-5 eV, $\Delta_0 = 0$.

Chapter 6

Conclusion

We have studied the loop-current theory for the pseudogap phase of the cuprates proposed by C. M. Varma (see e.g. [12] and the references herein) in a three-band mean-field approximation. We have studied the three different orbital current patterns seen in Figure 6.1 for two different hybridization energies, and in each case found a non-vanishing mean-field parameter to yield actual intra-orbital current patterns with the total current going through each orbital being a conserved quantity.

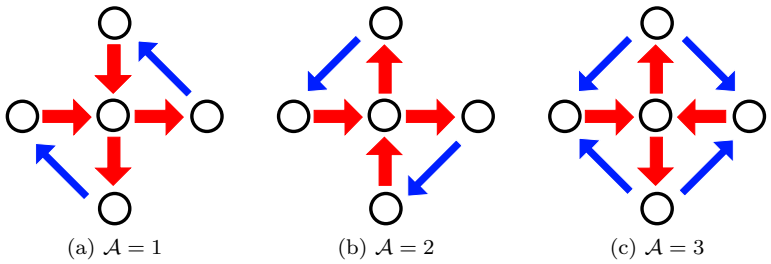

(a) $\mathcal{A} = 1$ (b) $\mathcal{A} = 2$ (c) $\mathcal{A} = 3$

Figure 6.1: The three intra unit-cell current patterns studied.

Imposing into this theory - for one of the two sets of hybridization energies - a possibility of a co-existing superconducting order parameter, we have studied the spatial modulations of the local density of states around a single point-like impurity using a Green's function formalism. It was found that in either of the nine resulting cases[1], the symmetries of the current pattern was reflected in the spatial symmetries of the local density of states, as exemplified in Figure 6.2.

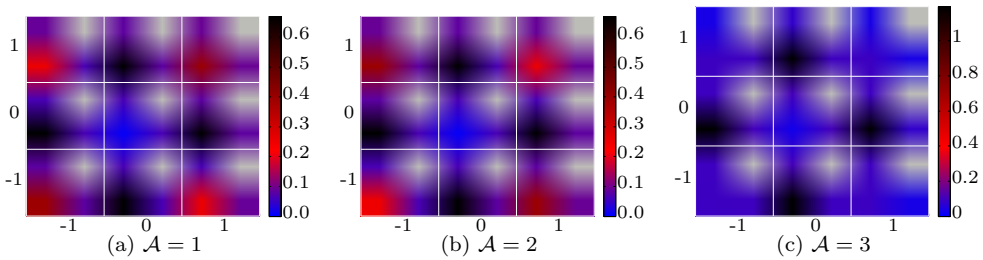

(a) $\mathcal{A} = 1$ (b) $\mathcal{A} = 2$ (c) $\mathcal{A} = 3$

Figure 6.2: The resulting LDOS maps around an impurity. Colour bar in arb. un.

[1] Three current patterns, two sets of hybridization energies, one of which may or may not include superconductivity.

The LDOS patterns were found to be completely oblivious to the directions of the currents, and the $\mathcal{A} = 3$ case thus respected every conceivable spatial symmetry, whereas the $\mathcal{A} = 1, 2$ cases broke axial reflection symmetry and C4. By comparison to the experimental literature (refs. [13] and [9]), it is found that the current patterns 1 and 2 are the most realistic candidates as realizations of the circulating current theory.

The persistent symmetry breaking for those two current patterns whenever the mean-field parameter for the orbital currents was varied away from zero was then related to the dispersion relation of the unperturbed system. It was found that the presence of orbital currents breaks the symmetry of the curves of constant energy on which elastic scattering takes place. For the superconducting case, the octet model gave a good qualitative explanation of this behaviour, but even with no superconductivity, the essence of this explanation remains valid.

As the energy dependence of the symmetry breaking is a bit unclear, an experimental search for the features we found should probe many different energies and avoid integrating over the energy, as this may cause cancellation or at least damping of the effect. Furthermore, as different domains of loop order may be present in a sample, it should be avoided to average over different domains, as this may again cause cancellations.

As a consequence of our results and discussion it is suggested to search for spatial non-C4 symmetric modulations of the local density of states by an STM measurement in a small field of view in the vicinity of a single impurity in the underdoped superconducting regime.

Appendix A

The current patterns for finite hybridizations energies

In the analysis of our data as well as in the parameter choices leading to our data, we have relied heavily on the phase of the mean-field current parameter having a certain value, in order for the current expectation values to be maximal. In chapter 3, only current expectation values calculated for the case of vanishing hybridization energies, i.e., $\epsilon_d = \epsilon_p = 0$ were presented. In this appendix the corresponding plots (corresponding to Figures 3.9 to 3.11) for the hybridization energies of $\epsilon_d = -1.5$ eV and $\epsilon_p = -5$ eV are shown. The conclusion is the same in this case as for the vanishing hybridization energies; for $\mathcal{A} = 1, 2$, R should be imaginary to yield the maximal currents, whereas R should be real for $\mathcal{A} = 3$ in order to achieve that. Furthermore, it remains true that two of the patterns break the C4 symmetry, whereas the last one preserves it, under the assumption that current directions are not visible to the STM (do not show up in the LDOS).

For all three plots in Figures A.1 to A.3 the length of R is fixed at 3, and the phase of R is varied. There are both red and blue points present, corresponding colour-wise to the arrows on the left. Note the nice current conservation.

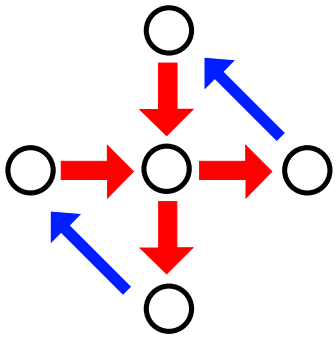

(a) The resulting current pattern.

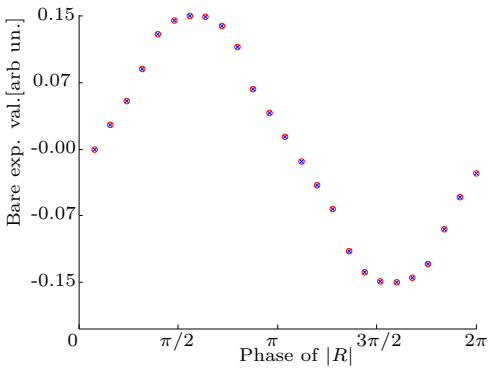

(b) The calculated current pattern.

Figure A.1: $\mathcal{A} = 1$.

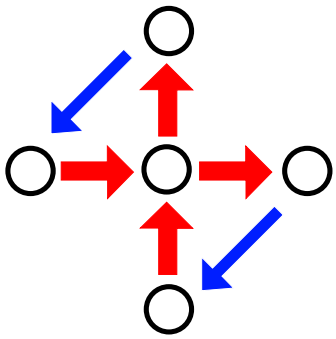

(a) The resulting current pattern.

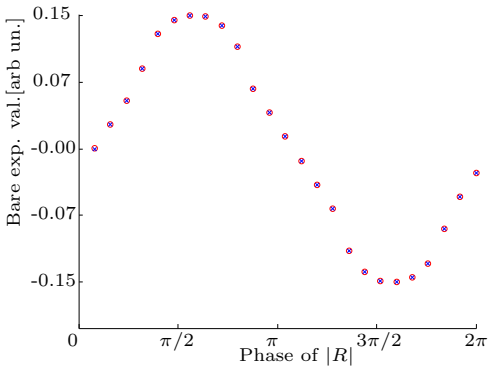

(b) The calculated current pattern.

Figure A.2: $\mathcal{A} = 2$.

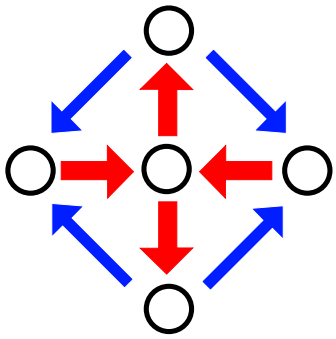

(a) The resulting current pattern.

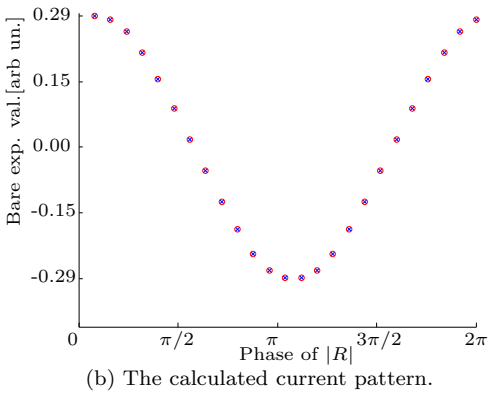

(b) The calculated current pattern.

Figure A.3: $\mathcal{A} = 3$.

Appendix B

Curves of constant energy

On the next two pages we display the curves of constant energy for the three different current patterns and three different parameter cases studied in chapter 5. Below each plot the hybridization energies used are displayed, and the parameters regarding superconductivity and orbital current strength are displayed above the plots.

For all three sets of parameter values, the same distinct pattern is clear. For $\mathcal{A} = 3$ no symmetries are broken, and a rather large R-parameter is necessary in order to see any change in the constant energy curves. For $\mathcal{A} = 1, 2$ the symmetry breaking is obvious even for a small value of $|R|$, and it is further noted that the two cases are related by a π-rotation, in accordance with their resulting current patterns (shown in chapter 3 and in appendix A).

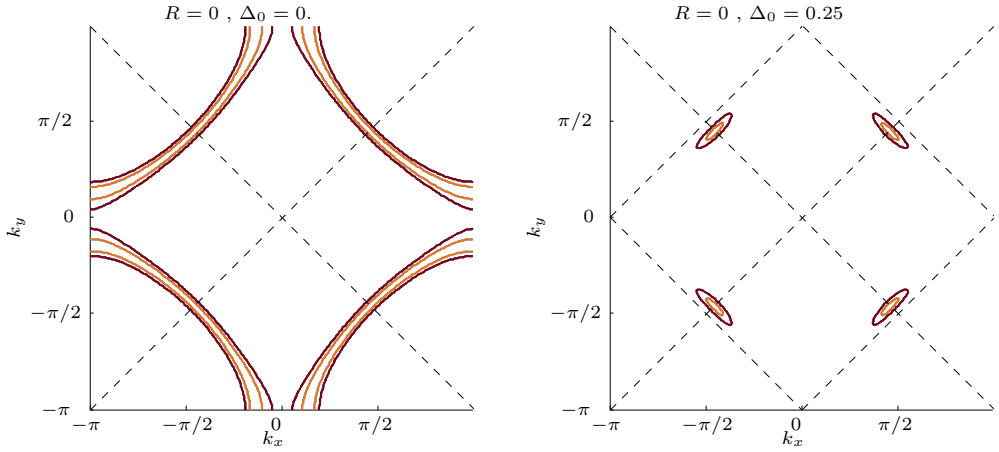

Figure B.1: Hybridization energies: $\epsilon_d = -1.5$ eV, $\epsilon_p = -5$ eV.

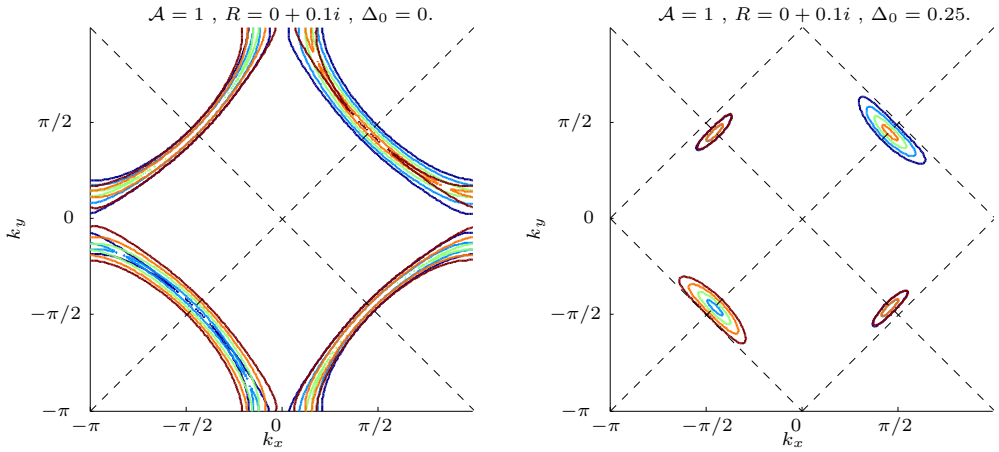

Figure B.2: Hybridization energies: $\epsilon_d = -1.5$ eV, $\epsilon_p = -5$ eV.

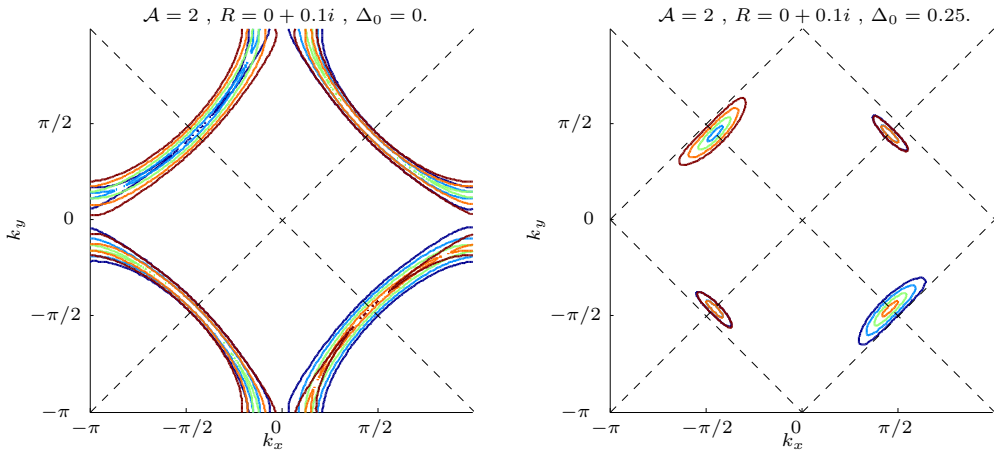

Figure B.3: Hybridization energies: $\epsilon_d = -1.5$ eV, $\epsilon_p = -5$ eV.

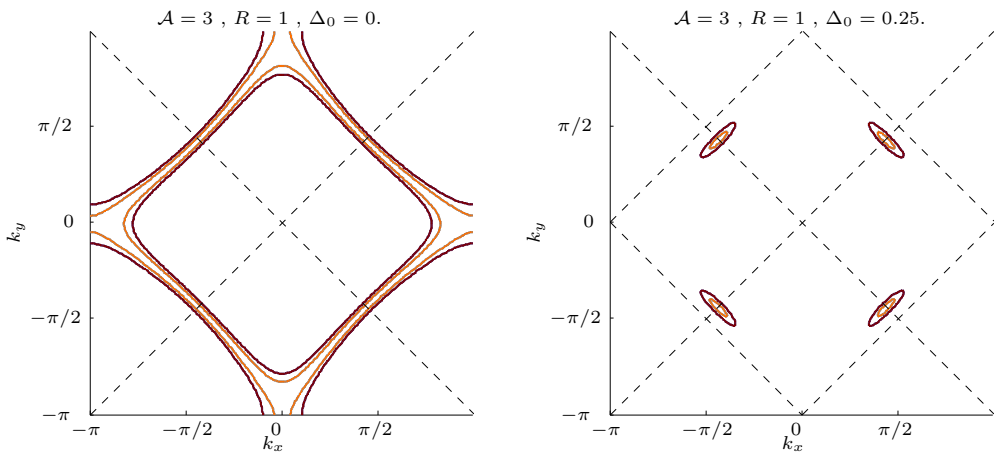

Figure B.4: Hybridization energies: $\epsilon_d = -1.5$ eV, $\epsilon_p = -5$ eV.

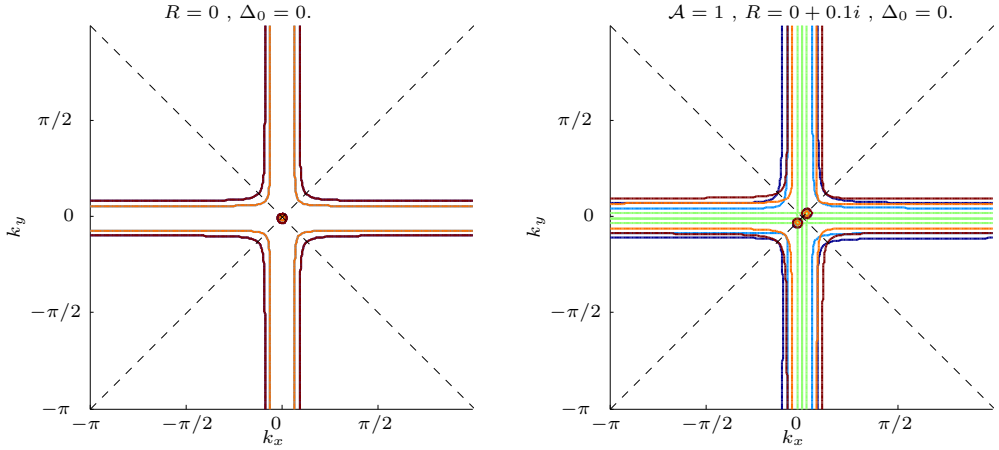

Figure B.5: Hybridization energies: $\epsilon_d = \epsilon_p = 0$.

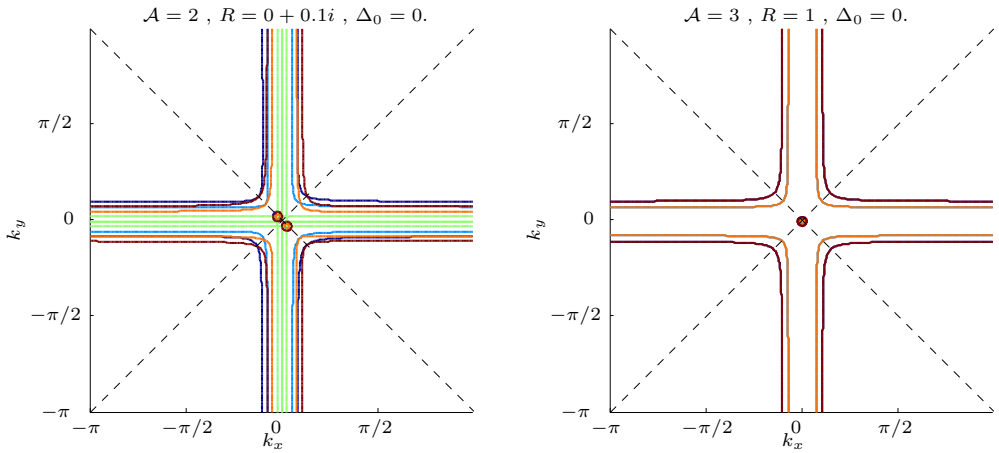

Figure B.6: Hybridization energies: $\epsilon_d = \epsilon_p = 0$.

Bibliography

[1] D. van Delft and P. Kes, Physics Today **63**, 38 (2010).

[2] J. Bardeen, L. N. Cooper, and J. R. Schrieffer, Physical Review **106**, 162 (1957).

[3] J. Bednorz and K. Müller, Zeitschrift für Physik B **64**, 189 (1986).

[4] B. M. Andersen, *Coexistence of Magnetic and Superconducting Order in the High-T_c Materials*, PhD thesis, University of Copenhagen, 2004.

[5] M. Greiter and R. Thomale, Physical Review Letters **99**, 027005 (2007).

[6] D. A. Bonn, Nature Physics **2**, 159 (2006).

[7] M. R. Norman, D. Pines, and C. Kallin, Advances in physics **54**, 715 (2005).

[8] C. Renner, B. Revaz, J.-Y. Genoud, K. Kadowaki, and Ø. Fischer, Physical Review Letters **80**, 149 (1998).

[9] B. Fauqué *et al.*, Physical Review Letters **96**, 197001 (2006).

[10] C. M. Varma, Physical Review B **55**, 14554 (1997).

[11] C. M. Varma, Physical Review Letters **83**, 3538 (1999).

[12] C. M. Varma, Physical Review B **73**, 155113 (2006).

[13] A. Kaminski *et al.*, Nature **416**, 610 (2002).

[14] V. Scagnoli *et al.*, Science **332**, 696 (2011).

[15] M. J. Lawler *et al.*, Nature **466**, 347 (2010).

[16] S. Strässle, B. Graneli, M. Mali, J. Roos, and H. Keller, Physical Review Letters **106**, 097003 (2011).

[17] S. V. Borisenko *et al.*, Physical Review Letters **92**, 207001 (2004).

[18] J. Tersoff and D. R. Hamann, Physical Review B **31**, 805 (1985).

[19] E. W. Hudson, S. H. Pan, A. K. Gupta, K.-W. Ng, and J. C. Davis, Science **285**, 88 (1999).

[20] J. E. Hoffman *et al.*, Science **297**, 1148 (2002).

[21] S. H. Pan, E. W. Hudson, K. M. Lang, H. Eisaki, and S. Uchida, Nature **403**, 746 (2003).

[22] V. J. Emery, Physical Review Letters **58**, 2794 (1987).

[23] H. Bruus and K. Flensberg, *Many-Body Quantum Theory in Condensed Matter Physics* (Oxford University Press, 2004).

[24] A. Altland and B. Simons, *Condensed Matter Field Theory*, second ed. (Cambridge University Press, 2010).

[25] M. Tinkham, *Introduction to superconductivity*, second ed. (McGraw-Hill, 1996).

[26] Y. Nambu, Physical Review **117**, 648 (1960).

[27] K. Riley, M. Hobson, and S. Bence, *Mathematical methods for Physics and Engineering*, third ed. (Cambridge University Press, 2006).

[28] M. H. Fischer and E.-A. Kim, Physical Review B **84**, 144502 (2011).

[29] Z. B. Huang, H. Q. Lin, and J. E. Gubernatis, Physical Review B **63**, 115112 (2011).

[30] H. Eskes and G. A. Sawatzky, Physical Review B **44**, 9656 (1991).

[31] E. R. Tufte, *The Visual Display of Quantitative Information*, second ed. (Graphics Press, 2001).

[32] K. McElroy *et al.*, Nature **422**, 592 (2003).

[33] Q.-H. Wang and D.-H. Lee, Physical Review B **67** (2003).

[34] T. S. Nunner, W. Chen, B. M. Andersen, A. Melikyan, and P. J. Hirschfeld, Physical Review B **73** (2006).